Physical and Numerical Modeling of Large Marine Microplastics Transport and Deposition

by

Mostafa Bigdeli

Thesis submitted to the University of Ottawa
in partial fulfillment of the requirements for the
Doctorate in Philosophy degree in Civil Engineering

Department of Civil Engineering
Faculty of Engineering
University of Ottawa

Abstract

The prevalence of micro-sized plastic pollution has raised significant concerns for aquatic ecosystems and their inhabitants, including humans, due to its distinct physical and toxicological characteristics. Large microplastics (MPs), primarily synthetic polymers measuring less than 5 mm, pose a considerable threat. According to the literature, rivers alone transport millions of tons of plastic into the ocean annually, regardless of other water bodies. During this transport, MPs undergo physical processes such as advection and diffusion, influenced by atmospheric and hydrological conditions. These processes are driven by larger-scale factors, including wind-induced drag, wave drift, and buoyancy, all stemming from currents, geostrophic circulation, and turbulence in extensive water bodies.

The inherent properties of MPs—such as size, shape, and density—along with fluid flow characteristics like velocity, depth, and pressure, play crucial roles in determining their transport and deposition patterns. Consequently, this thesis aimed to use physical and numerical modeling approaches to investigate MPs' transport and deposition under varying hydraulic parameters and bathymetric changes applied to the channel bed.

The experimental component of this research involved reviewing existing studies and conducting physical modeling of MPs transport and deposition. Various experimental test scenarios were carried out in a tilting flume at the National Research Council Canada Ocean, Coastal, and River Engineering Research Centre (NRC-OCRE) physical testing facility in Ottawa. Data on MPs transport and deposition were gathered using different physical setups in a straight open-channel flume to assess the effects of flow velocity, water levels, channel geometries, and particle shapes. This study contributed to validating numerical models for MPs transport and deposition.

The second part of the research, focusing on numerical modeling, followed three steps: (1) reviewing the literature, (2) using a machine learning (ML) approach to predict MPs transport and deposition dynamics for large spherical and cylindrical MPs, and (3) simulating MPs transport and deposition using a coupled computational fluid dynamics-discrete element method (CFD-DEM).

For the first step, a comprehensive review was conducted on the structure of four well-known Lagrangian particle tracking models (D-WAQ PART, Ichthyop, TrackMPD, and CaMPSim-3D) in simulating MPs' fate and transport. Each model was examined in terms of its ability to account

for key physical transport processes—such as advection, diffusion, windage, beaching, and washing off—as well as transformation processes like biofouling and degradation, which influence MPs' behavior in the marine environment. Additionally, the review evaluated the effects of MPs' physical properties (mainly size, diameter, and shape) on their fate and trajectories. This analysis identified gaps in particle tracking models, including insufficient consideration of homo- and hetero-aggregation, agglomeration, photodegradation, chemical and biological degradation, and additional advection caused by wave-induced drift.

In the second step of the numerical research, an ML-based study was conducted to predict the deposition patterns of spherical and cylindrical MPs using Extreme Learning Machines (ELM) for the first time, based on laboratory datasets. Various test scenarios were performed to collect data on multiple input parameters, including flow velocity, channel bed deepening, channel bed slope, water level, particle shape (spherical or cylindrical), near-bed flow velocity, and particle velocity at deposition. Eleven models, utilizing different dimensionless input combinations derived from Buckingham’s theorem, were evaluated. The best-performing model incorporated all four dimensionless variables, achieving high accuracy for spherical (R=0.94) and cylindrical (R=0.90) MPs. Sensitivity analysis revealed that the ratio of water depth to particle diameter had the greatest impact on deposition patterns. This study highlighted the potential of ML in predicting MPs behavior, aiding environmental monitoring and management.

In the final step, numerical results were validated against laboratory experiments. A numerical modeling approach was employed to simulate the transport and deposition of spherical MPs under different flow and channel geometry scenarios. The unresolved CFD-DEM method was used for simulations, with results successfully validated through experimental measurements. Additionally, the model effectively captured the influence of hydraulic parameters on MPs deposition.

I would like to dedicate this thesis to my family.

To my dear mother and father, whose unwavering love and encouragement have supported me through every decision, even while I studied abroad. To my sisters, Mahsa and Maryam, for always being there for me. To my beloved wife, Mercedeh, whose belief in me and unwavering strength have been my greatest support. And to my son, Liam, who means the world to me.

Acknowledgments

I would like to express my deepest gratitude to my supervisor, Prof. Abdolmajid Mohammadian, whose invaluable guidance and unwavering support were fundamental to the completion of this doctoral thesis. His expertise and encouragement fueled my passion and determination to explore the complexities of my research.

I am also profoundly thankful to Dr. Abolghasem Pilechi, as my co-supervisor, for his support, particularly during the implementation of my experiments in the lab and CFD-based simulations. It has been a great pleasure working with Prof. Hossein Bonakdari, whose support was instrumental in numerical modeling using artificial intelligence.

I extend my sincere appreciation to my Ph.D. defense committee members—Prof. Ioan Nistor, Prof. Infante Sedano, Dr. Hamidreza Shirkhani, and Prof. Mona Rahmani—for their time, effort, and valuable feedback.

A special thanks to Yvan Brunet and the Laboratory Technicians at the National Research Council Canada Ocean, Coastal, and River Engineering Research Centre (NRC-OCRE) for their assistance in setting up the physical model and continuously modifying its design to accommodate various test scenarios.

I would also like to acknowledge the National Research Council Canada for the financial support that made this academic endeavor possible.

To my parents, I am eternally grateful for their boundless love, encouragement, and sacrifices. Their unwavering belief in me has been a constant source of motivation, and I am forever thankful for the values and resilience they instilled in me.

Finally, to my wife, Mercedeh, I owe an immeasurable debt of gratitude. Her patience, understanding, and steadfast support throughout my Ph.D. journey have been my greatest source of strength. Her unwavering belief in my dreams and the countless sacrifices she made have been instrumental to my success. You have endured every high and low of this journey with me, and for that, I am forever grateful.

Publications from this research

The following publications have resulted from this research:

- **Bigdeli, M.**, Mohammadian, A., Pilechi, A., Taheri, M. (2022). "Lagrangian modeling of marine microplastics fate and transport: the state of the science", published by Journal of Marine Science and Engineering, MDPI. https://doi.org/10.3390/jmse10040481
- **Bigdeli, M.**, Mohammadian, A., Pilechi, A. (2022). "Numerical Modeling of Marine Microplastics Deposition using coupled CFD-DEM" accepted in 3rd IAHR Young Professionals Congress.
- **Bigdeli, M.**, Mohammadian, A., Pilechi, A. (2024). "A Laboratory Dataset on Transport and Deposition of Spherical and Cylindrical Large Microplastics for Validation of Numerical Models", published by Journal of Marine Science and Engineering, MDPI. https://doi.org/10.3390/jmse12060953
- **Bigdeli, M.**, Mohammadian, A., Pilechi, A., Bonakdari, H. (2025). "Dynamic Prediction of Large Spherical and Cylindrical Microplastic Deposition: A Machine Learning Approach for Transport and Deposition", (submitted).
- **Bigdeli, M.**, Mohammadian, A., Pilechi, A. (2025). "Numerical Modeling of Large Spherical Microplastics Transport and Deposition using CFD-DEM", (submitted).

Table of Contents

List of Figures

List of Tables

List of Abbreviations

ADV	Acoustic Doppler Velocimeter
AI	Artificial Intelligence
ANFIS	Adaptive Neuro-Fuzzy Inference Systems
ANN	Artificial Neural Networks
CaMPSim-3D	Canadian Microplastic Simulation
CFD	Computational Fluid Dynamics
Cyln.	Cylindrical
DEM	Discrete Element Method
D-WAQ PART	Delft3D - Water Quality Particle tracking module
ELM	Extreme Learning Machines
FFNN	Feedforward Neural Networks
FOV	Field Of View
GDP	Gross Domestic Product
Ichthyop	Ichthyoplankton
ML	Machine Learning
MPs	Microplastics
NRC-OCRE	National Research Council Canada Ocean, Coastal, and River Engineering Research Centre
PaTATO	Particle Tracking and Analysis Toolbox
PDSA	Partial Derivative Sensitivity Analysis
PEI	Prediction Interval Error
PET	Polyethylene Terephthalate
PTM	Particle Tracking Models
PVC	Polyvinyl Chloride
RA	Relative Accuracy
SLFFNN	Single-Layer Feedforward Neural Network
Sphr.	Spherical
SVM	Support Vector Machines

TE	Trap Efficiency
TrackMPD	Track Marine Plastic Debris
WUB	Width of Uncertainty Band

List of Symbols

d_p	Particle diameter
v	Flow dynamic viscosity
w	Water depth in the channel
u_f	Flow velocity
h	Water depth in the channel at the deepening
s	Slope applied to the channel's bed
π_1	$\frac{w}{d_p}$
π_2	$\frac{h}{d_p}$
π_3	$\frac{u_f d_p}{v}$
π_4	s
R	Correlation Coefficient
MAE	Mean Absolute Error
$RMSE$	Root Mean Square Error
$BIAS$	Bias
e_i	Individual prediction error
$\bar{e}$	Mean prediction error
S_e	Standard deviation of prediction error
T_R	Rayleigh time
G	Shear modulus
Y	Young's modulus
R	Particle radius
ρ	Particle density
$t_{constact,H}$	Hertz contact time
ε_f	Void fraction
k	Turbulent kinetic energy
f_s	Sliding friction
f_r	Rolling friction

1 Introduction and Study Objectives

1.1 General Background

While most plastics are expected to float on the water's surface due to their lower density than water, research findings from (Kaiser et al., 2017) and (Zhang et al., 2019) have revealed a significant presence of plastic waste in the sediment beds of various water bodies, including coastal waters and rivers. Surprisingly, estimates suggest that around 99% of all plastics that have entered the world's oceans are unaccounted for, possibly having been deposited in sediments or deep ocean waters. A global analysis of plastic production and often unregulated disposal by (Geyer et al., 2017) projects that plastic debris accumulation in natural environments and landfills could reach a staggering 12,000 million metric tons (Mt) by 2050.

Rivers are recognized as one of the primary conduits for transporting plastic waste from land to oceans, with an estimated annual rate ranging from 0.41 to 4.0 Mt (Corcoran et al., 2019). Previous studies have emphasized that the mobility of micro-sized particles in aquatic environments is influenced by various factors, including particle-specific characteristics (such as size, density, shape, chemical composition), water chemistry, surface charge, surface coating, hydrodynamic conditions, and sediment properties like grain size distribution and organic matter content (Klaine et al., 2008; Masliyah, 1998; Wiesner & Bottero, 2017). It is challenging to accurately estimate the plastic load within sediments due to the absence of standardized data analysis procedures that account for the inherent variability in natural conditions and limited density of available samples. To make valid comparisons across different spatial and temporal scales, it is essential to consider hydrodynamic conditions at a local level. This consideration is crucial because the variations in microplastic abundance observed at small spatial scales can be more pronounced than those seen at larger spatial scales, as indicated by studies like (Enders et al., 2019; Martin et al., 2017). Further details have been provided in section 1.9.

Physical and numerical modeling serve as valuable tools for predicting the fate and transport of plastic debris, offering a potential solution to mitigate the plastic pollution problem. Therefore, it is crucial to thoroughly characterize and quantify the deposition of plastic debris in bed materials, especially when developing numerical models to simulate the fate and transport of plastic debris

in water bodies. This information is vital for tasks like mass balance calculations and estimating the transport of plastic debris versus its deposition.

A comprehensive understanding of MPs' behavior in water resources is essential due to the following challenges:

1. Widespread Distribution & Environmental Impact:

The high production rate and rapid industrial growth of plastics pose a substantial threat to marine ecosystems and biodiversity, leading to severe pollution. The transport and deposition of MPs can adversely affect water quality, making it unsuitable for drinking or other uses.

2. Bioaccumulation & Health Risks:

MPs can be absorbed by marine fauna, entering the food chain and persisting without degradation (Alvarez-Zeferino et al., 2020). The distribution and accumulation of MPs—given their diverse types, origins, and compositions—raise serious concerns. MPs can infiltrate the body tissues of marine species and human lymph, liver, kidney, and circulatory systems (Vethaak & Legler, 2021). Additionally, MPs can serve as platforms for the growth of harmful biofilms (Vethaak & Legler, 2021). It is, therefore, crucial to identify high-accumulation zones, assess associated risks, and implement mitigation strategies.

3. Lack of Comprehensive Studies:

Limited reliable and comprehensive studies on MPs in water bodies hinder our ability to understand their behavior and plan effective mitigation and remediation strategies. Existing studies have primarily focused on collecting, pretreating, and analyzing MPs (Ballent et al., 2016; Bujaczek et al., 2021; Castañeda et al., 2014; Corcoran et al., 2019; Vermaire et al., 2017).

4. Unclear Deposition & Accumulation Patterns:

Despite significant findings on the abundance, shape, color, and size of MPs (Ballent et al., 2016; Bujaczek et al., 2021; Castañeda et al., 2014; Corcoran et al., 2019), their deposition and accumulation patterns remain largely unknown, limiting our understanding of their environmental impact on marine ecosystems.

5. Unresolved Deposition Characteristics:

The deposition behavior of MPs is not yet fully understood. Assessing water bodies using laboratory experiments, modeling approaches, and numerical simulations can provide critical insights into MPs' deposition mechanisms, making it a worthwhile research endeavor.

1.2 Research Questions

Several key questions arise when considering the transport and deposition of MPs in water bodies:

1. Which hydraulic factors have the greatest influence on the transport and deposition of MPs in water bodies?

2. In the context of changes in water body bathymetry, how do changes in bathymetry impact particle transport and deposition?

3. Is ML capable of sufficiently predicting the behavior of MPs under the influence of different hydraulic flow conditions and different physical characteristics of the MPs?

4. How effective are numerical models in capturing the precise distribution and deposition of MPs in water bodies?

1.3 Research Objectives and Significance

To address these questions comprehensively, it is imperative to establish research objectives in a manner that facilitates solutions to the aforementioned concerns and contributes to the existing body of knowledge. Accordingly, the research study's objectives are delineated as follows:

1. Develop and construct a physical model and conduct experimental trials to:

- Investigate the role of both transport and deposition in shaping the fate of marine MPs.
- Identify the pivotal hydraulic parameters, considering water bodies' flow characteristics that govern the transport and deposition of MPs particles.
- Determine how bathymetric changes in water bodies contribute to the formation of dead zones where MPs accumulate.

2. Verify and implement numerical simulations by integrating CFD-DEM model to:

- Explore the transport and deposition of MPs.

- Track particle behavior in turbulent marine conditions.

3. Evaluate the capability of the ELM model in predicting MPs deposition patterns based on a comprehensive and reliable experimental dataset derived from controlled test scenarios.

1.4 Research Outcomes

The main results of this research can be summarized as follows:

1. Enhance our comprehension of the dynamics of marine MPs transport and deposition in water bodies, considering different bathymetric conditions.
2. Present a robust and comprehensive physical model for a better understanding of the MPs' behavior in real world conditions.
3. Provide the capacity of CFD-based and AI-based numerical models to simulate and predict the transport and deposition of marine MPs.
4. Disseminate the research findings through the publication of scientific papers in peer-reviewed journals.

1.5 Novelty and Contribution of the Research

In order to meet the research study objectives, there are some novel contributions that were verified by lab tests. The main novelties are described below:

1. Elucidating the dynamic of marine MPs transport and deposition within the channel of water bodies
2. Comprehending the influence of varied hydraulic conditions in water bodies on MPs transport and deposition with different physical characteristics.
3. Identifying the most dominant parameter(s) governing the transport and deposition of MPs in the channel of water bodies.
4. Determine the accuracy of CFD-based and AI-based models in simulating MPs transport and deposition. This represents a state-of-the-art methodology in this field of study.

1.6 Research Scope

MPs present in water undergo various transformational processes, including biofouling (Kooi et al., 2017), degradation, and fragmentation (Atugoda et al., 2022; Cole et al., 2011; Nikpay, 2022), as well as hetero- and homo-aggregation (Atugoda et al., 2022; Besseling et al., 2017), commonly

referred to as particle-particle interactions (Van Sebille et al., 2020). These processes significantly impact on the destiny of MPs within their receiving environment. Furthermore, MPs have become widely distributed throughout marine ecosystems (Eriksen et al., 2014; Galgani et al., 2015a) due to various physical transport mechanisms, including horizontal and vertical advection, diffusion, and other factors. The transport of MPs in aquatic environments is influenced by a range of processes, including advection and dispersion driven by ambient currents, Stokes drift, sinking, resuspension, beaching, washing-off, deposition, aggregation, degradation, and fouling.

However, it's important to note that this study's specific focus is on addressing the existing knowledge gap regarding the transport and deposition of marine MPs, particularly those characterized by different bathymetric conditions. As a result, addressing transformational processes or other factors influencing MPs transport and deposition in water bodies is beyond the scope of this research. This limitation does not affect considerations related to the hydraulic conditions of the flow and the physical properties of the particles.

1.7 Thesis Outline

The remainder of this thesis is structured in the following way. Section 2 presents a literature review of the physical characteristics of MPs and the processes they undergo, as well as the Lagrangian modeling of the fate and transport of marine MPs. Section 3 presents an experimental study on the transport and deposition of large spherical and cylindrical MPs that can be employed to validate numerical models. Section 4 discusses the dynamic prediction of large spherical and cylindrical MPs deposition using the ELM. Section 5 deals with numerical modelling of the large spherical MPs transport and deposition using CFD-DEM and Section 6 offers essential insights as the concluding remarks.

1.8 List of Publications (from the thesis)

- **Bigdeli, M.**, Mohammadian, A., Pilechi, A., Taheri, M. (2022). “Lagrangian modeling of marine microplastics fate and transport: the state of the science”, published by Journal of Marine Science and Engineering, MDPI.
  https://doi.org/10.3390/jmse10040481

- **Bigdeli, M.**, Mohammadian, A., Pilechi, A. (2022). "Numerical Modeling of Marine Microplastics Deposition using coupled CFD-DEM" accepted in 3rd IAHR Young Professionals Congress.
- **Bigdeli, M.**, Mohammadian, A., Pilechi, A. (2024). "A Laboratory Dataset on Transport and Deposition of Spherical and Cylindrical Large Microplastics for Validation of Numerical Models", published by Journal of Marine Science and Engineering, MDPI. https://doi.org/10.3390/jmse12060953
- **Bigdeli, M.**, Mohammadian, A., Pilechi, A., Bonakdari, H. (2025). "Dynamic Prediction of Large Spherical and Cylindrical Microplastic Deposition: A Machine Learning Approach for Transport and Deposition", (submitted).
- **Bigdeli, M.**, Mohammadian, A., Pilechi, A. (2025). "Numerical Modeling of Large Spherical Microplastics Transport and Deposition using CFD-DEM", (submitted).

1.9 Appendix

There are substantial disparities in the findings regarding whether MPs abundance is linked to sediment composition, including grain size and organic matter content. Some studies, such as (Strand et al., 2013) have suggested a potential relationship, while others, such as (Renzi et al., 2018) have failed to establish such a connection. The existence of this controversy in literature underscores the existing gaps in our knowledge regarding the possible association between MPs and sediment.

MPs dynamics have previously been studied primarily in terms of rising and settling processes (Yu et al., 2022). Considering the density of half of all plastics is higher than that of seawater (Morét-Ferguson et al., 2010), the terminal settling velocity is a key parameter used to characterize the migration of MPs into water bodies (Khatmullina and Isachenko, 2017). The density, shape, and particle size of MPs have been found to have a significant impact on the terminal settling velocity (Yu et al., 2022).

There is also a relationship between surface wettability and the settling velocity and drag coefficient of micro-sized particles (Wang et al., 2020). In this respect, hyporheic zones have also been investigated for the settling mechanisms of MPs. Thus, stagnant zones are vital reservoirs for the long-term sink of MPs, which are remobilized and resuspended at higher flow rates (Kumar et al., 2021). It has been observed that MPs with varying particle diameters settle at different speeds

(Kumar et al., 2021). In addition to natural sediments, MPs particles' settling and rising velocities significantly affect their erosivity (Waldschläger and Schüttrumpf, 2019a). MPs settle and sediment primarily as a result of gravitational forces (Frei et al., 2019). Also, MPs have been observed to settle in rivers that have sloped beds, i.e., as flow velocity increases, MPs travel over longer distances (Kumar et al., 2021). However, according to (Hoellein et al., 2019), there is a positive correlation between MPs diameter and deposition velocity (V_{dep}), as opposed to a negative correlation between deposition velocity and settling velocity (V_{fall}). Particles with diameters between 50 and 500 meters are deposited under the influence of gravity when V_{dep}/V_{fall} ratio is equal to 1. By contrast, when $V_{dep}/V_{fall} \gg 1$, particles with a diameter < 50 m have a high retention rate while for $V_{dep}/V_{fall} \ll 1$, particles with a diameter > 500 µm are influenced by hydrologic actions including momentum and resuspension which are both larger than gravitational settlings (Hoellein et al., 2019).

As stated above, MPs and sediments are different in terms of the physical properties (e.g., density, size, and shape) that affect their transport. The application of the basic and governing principles of sediment transport to MPs transport has therefore remained in doubt for this reason and due to the lack of sufficient knowledge of the prevailing transport mechanisms. Additionally, it is also important to determine whether it is possible to calculate the terminal settling and rising velocities of MPs, which have physical properties different from sediments, using theoretical methods that are derived from sediment transport models. In order to investigate the aforesaid concerns, the nutshell of the reviewed papers are summarized as below:

- It has been reported that there is often a correlation between MPs and sediment grain size. Different conclusions have been reached regarding the impact of sediment composition, such as grain size and organic matter content, on the abundance of MPs. Some of them reported indications of such a relationship, but others were unable to prove it. There are currently knowledge gaps regarding the potential relationship between MPs and sediment as a result of a controversy of this nature in literature.

- The bed-load transport phenomenon occurs when successive particle contacts with the bed are strictly limited by gravity while during suspended load transport, turbulent eddies impart upward impulses to support all the excess weight of the particles. Depending on the particle size,

weight, shape, and ambient hydraulic conditions, an individual particle may be transported as a suspended load or as a bedload.

- In partial transport, a type of bed load transport, finer material is mobilized, and coarser material remains immobile when the bed shear stress is too low to mobilize it.

- Due to the fact that the start of a particle trajectory is determined by random fluid forces, the length and height of the trajectory are also random variables. The saltation model can be used to determine the heights, lengths, and velocities of hopping grains.

- Different MPs settle at different rates depending on their particle diameter. As well as natural sediments, MPs particles' settling and rising velocities have a significant impact on their erosivity.

- Given the aforementioned and due to the similar geometric characteristics between MPs and non-cohesive sediment particles, principles associated with sediment incipient motion can be applicable to MPs as well (Waldschläger and Schüttrumpf, 2019b, Yu et al., 2022). MPs particles begin to move under the action of currents after they settle on the riverbed or seafloor. Incipient sediment motion is extensively governed by the critical shear stress, which is the minimum flow shear stress required for a single particle to move.

- Due to the hiding exposure effect, large grains may be exposed on the far side of the layer as a result of MPs of smaller dimensions being layered over them. By varying the hiding-exposure coefficient, the hiding-exposure effect can be fitted.

As reviewed in earlier sections, most previous studies have focused on applying sediment transport equations to MPs by considering only the onset of sediment motion (incipient motion). However, this leaves a significant knowledge gap regarding how MPs behave when they interact with the bed surface. This study aimed to address that gap by providing deeper insights into how MPs are trapped, rolled, slid, or saltated across a reliable range of conditions, using precise experimental testing. Subsequently, numerical models were calibrated based on these experimental observations.

1.10 References

Alvarez-Zeferino, Juan Carlos, Sara Ojeda-Benítez, Arely Areanely Cruz-Salas, Carolina Martínez-Salvador, and Alethia Vázquez-Morillas. 2020. 'Microplastics in Mexican beaches', Resources, Conservation and Recycling, 155: 104633.

Atugoda, Thilakshani, Hansika Piyumali, Sureka Liyanage, Kushani Mahatantila, and Meththika Vithanage. 2022. 'Fate and behavior of microplastics in freshwater systems.' in, Handbook of Microplastics in the Environment (Springer).

Ballent, Anika, Patricia L Corcoran, Odile Madden, Paul A Helm, and Fred J Longstaffe. 2016. 'Sources and sinks of microplastics in Canadian Lake Ontario nearshore, tributary and beach sediments', Marine pollution bulletin, 110: 383-95.

Besseling, Ellen, Joris TK Quik, Muzhi Sun, and Albert A Koelmans. 2017. 'Fate of nano-and microplastic in freshwater systems: A modeling study', Environmental pollution, 220: 540-48.

Bujaczek, Taylor, Sheldon Kolter, David Locky, and Matthew S Ross. 2021. 'Characterization of microplastics and anthropogenic fibers in surface waters of the North Saskatchewan River, Alberta, Canada', Facets, 6: 26-43.

Castañeda, Rowshyra A, Suncica Avlijas, M Anouk Simard, and Anthony Ricciardi. 2014. 'Microplastic pollution in St. Lawrence river sediments', Canadian Journal of Fisheries and Aquatic Sciences, 71: 1767-71.

Cole, Matthew, Pennie Lindeque, Claudia Halsband, and Tamara S Galloway. 2011. 'Microplastics as contaminants in the marine environment: a review', Marine pollution bulletin, 62: 2588-97.

Corcoran, Patricia L, Sara L Belontz, Kelly Ryan, and Mary Jane Walzak. 2019. 'Factors controlling the distribution of microplastic particles in benthic sediment of the Thames River, Canada', Environmental science & technology, 54: 818-25.

Enders, K., Käppler, A., Biniasch, O., Feldens, P., Stollberg, N., Lange, X., Fischer, D., Eichhorn, K.J., Pollehne, F., Oberbeckmann, S. and Labrenz, M., 2019. Tracing microplastics in aquatic environments based on sediment analogies. Scientific Reports, 9(1), p.15207.

Eriksen, Marcus, Laurent CM Lebreton, Henry S Carson, Martin Thiel, Charles J Moore, Jose C Borerro, Francois Galgani, Peter G Ryan, and Julia Reisser. 2014. 'Plastic pollution in the

world's oceans: more than 5 trillion plastic pieces weighing over 250,000 tons afloat at sea', PLoS One, 9: e111913.

Frei, S., Piehl, S., Gilfedder, B.S., Löder, M.G., Krutzke, J., Wilhelm, L. and Laforsch, C., 2019. Occurence of microplastics in the hyporheic zone of rivers. Scientific reports, 9(1), p.15256.

Galgani, François, Georg Hanke, and Thomas Maes. 2015. 'Global distribution, composition and abundance of marine litter', Marine anthropogenic litter: 29-56.

Geyer, Roland, Jenna R Jambeck, and Kara Lavender Law. 2017. 'Production, use, and fate of all plastics ever made', Science advances, 3: e1700782.

Hoellein, T.J., Shogren, A.J., Tank, J.L., Risteca, P. and Kelly, J.J., 2019. Microplastic deposition velocity in streams follows patterns for naturally occurring allochthonous particles. Scientific reports, 9(1), p.3740.

Kaiser, David, Nicole Kowalski, and Joanna J Waniek. 2017. 'Effects of biofouling on the sinking behavior of microplastics', Environmental research letters, 12: 124003.

Khatmullina, L. and Isachenko, I., 2017. Settling velocity of microplastic particles of regular shapes. Marine pollution bulletin, 114(2), pp.871-880.

Klaine, Stephen J, Pedro JJ Alvarez, Graeme E Batley, Teresa F Fernandes, Richard D Handy, Delina Y Lyon, Shaily Mahendra, Michael J McLaughlin, and Jamie R Lead. 2008. 'Nanomaterials in the environment: behavior, fate, bioavailability, and effects', Environmental Toxicology and Chemistry: An International Journal, 27: 1825-51.

Kooi, Merel, Egbert H van Nes, Marten Scheffer, and Albert A Koelmans. 2017. 'Ups and downs in the ocean: effects of biofouling on vertical transport of microplastics', Environmental science & technology, 51: 7963-71.

Kumar, R., Sharma, P., Verma, A., Jha, P.K., Singh, P., Gupta, P.K., Chandra, R. and Prasad, P.V., 2021. Effect of physical characteristics and hydrodynamic conditions on transport and deposition of microplastics in riverine ecosystem. Water, 13(19), p.2710.

Martin, J., Lusher, A., Thompson, R.C. and Morley, A., 2017. The deposition and accumulation of microplastics in marine sediments and bottom water from the Irish continental shelf. Scientific Reports, 7(1), p.10772.

Masliyah, Jacob. 1998. 'Particle Deposition and Aggregation: Measurement, Modelling and Simulation. M. Elimelechet al', Journal of Colloid and Interface Science, 200: 195.

Nikpay, Mitra. 2022. 'Wastewater fines influence the adsorption behavior of pollutants onto microplastics', Journal of Polymers and the Environment, 30: 776-83.

Renzi, M., Blašković, A., Fastelli, P., Marcelli, M., Guerranti, C., Cannas, S., Barone, L. and Massara, F., 2018. Is the microplastic selective according to the habitat? Records in amphioxus sands, Mäerl bed habitats and Cymodocea nodosa habitats. Marine pollution bulletin, 130, pp.179-183.

Strand, J., Lassen, P., Shashoua, Y. and Andersen, J., 2013. Microplastic particles in sediments from Danish waters.

Van Sebille, Erik, Stefano Aliani, Kara Lavender Law, Nikolai Maximenko, José M Alsina, Andrei Bagaev, Melanie Bergmann, Bertrand Chapron, Irina Chubarenko, and Andrés Cózar. 2020. 'The physical oceanography of the transport of floating marine debris', Environmental research letters, 15: 023003.

Vermaire, Jesse C, Carrington Pomeroy, Sofia M Herczegh, Owen Haggart, and Meaghan Murphy. 2017. 'Microplastic abundance and distribution in the open water and sediment of the Ottawa River, Canada, and its tributaries', Facets, 2: 301-14.

Vethaak, A Dick, and Juliette Legler. 2021. 'Microplastics and human health', Science, 371: 672-74.

Waldschläger, K. and Schüttrumpf, H., 2019a. Effects of particle properties on the settling and rise velocities of microplastics in freshwater under laboratory conditions. Environmental science & technology, 53(4), pp.1958-1966.

Waldschläger, K. and Schüttrumpf, H., 2019b. Erosion behavior of different microplastic particles in comparison to natural sediments. Environmental science & technology, 53(22), pp.13219-13227.

Wang, L., Zheng, K., Ding, Z., Yan, X., Zhang, H., Cao, Y. and Guo, C., 2020. Drag coefficient and settling velocity of fine particles with varying surface wettability. Powder Technology, 372, pp.8-14.

Wiesner, Mark R, and Jean-Yves Bottero. 2017. 'Surface Chemistry of Nanoparticles as It Affects Attachment', Environmental Nanotechnology: Applications and Impacts of Nanomaterials, Second Edition.

Yu, Z., Yao, W., Loewen, M., Li, X. and Zhang, W., 2022. Incipient motion of exposed microplastics in an open-channel flow. Environmental Science & Technology, 56(20), pp.14498-14506.

Zhang, Jiaxu, Chenglong Zhang, Yixiang Deng, Ruixue Wang, En Ma, Jingwei Wang, Jianfeng Bai, Jin Wu, and Yongjie Zhou. 2019. 'Microplastics in the surface water of small-scale estuaries in Shanghai', Marine pollution bulletin, 149: 110569.

2 Lagrangian Modeling of Marine Microplastics Fate and Transport: The State of the Science

2.1 Abstract

Microplastics pollution has led to irreversible environmental consequences and has triggered global concerns. It has been shown that water resources and marine food consumers are adversely affected by microplastics due to their physico-chemical characteristics. This study attempts to comprehensively review the structure of four well-known Lagrangian particle-tracking models, i.e., Delft3D - Water Quality Particle tracking module (D-WAQ PART), Ichthyoplankton (Ichthyop), Track Marine Plastic Debris (TrackMPD), and Canadian Microplastic Simulation (CaMPSim-3D) in simulating the fate and transport of microplastics. Accordingly, the structure of each model is investigated with respect to addressing the involved physical transport processes (including advection, diffusion, windage, beaching, and washing-off) and transformation processes (particularly biofouling and degradation) that play key roles in microplastics' behavior in the marine environment. In addition, the effects of the physical properties (mainly size, diameter, and shape) of microplastics on their fate and trajectories are reviewed. The models' capabilities and shortcomings in the simulation of microplastics are also discussed. The present review sheds light on some aspects of microplastics' behavior in water that were not properly addressed in particle-tracking models, such as homo- and hetero-aggregation, agglomeration, photodegradation, and chemical and biological degradation as well as additional advection due to wave-induced drift. This study can be regarded as a reliable steppingstone for the future modification of the reviewed models.

2.2 Introduction

Aquatic environments, including oceans, coastal regions, estuaries, seas, and rivers, as major planetary water resources, have been affected by marine plastic debris accumulation and distribution, which has triggered global environmental concern and irreversible pollution consequences (Bergmann et al., 2015; Panno et al., 2019; Wagner & Lambert, 2018). Macro ($>$ 1 cm) (N. Hartmann et al., 2015), meso (5 mm – 2 cm) (N. Hartmann et al., 2015), micro ($<$ 5 mm) (Rocha-Santos & Duarte, 2015), and nano-size (1 nm – 100 nm) (EU, 2019b) plastics pollution has become a critical environmental problem due to their persistence, toxicological properties, and destructive effects on not only Earth's hydrosphere (Barnes et al., 2009) but also

aquatic organisms (Koelmans et al., 2016; Ryan et al., 2009; Thevenon et al., 2014a; Wright et al., 2013), wildlife, and human health (Lithner et al., 2011; Napper & Thompson, 2019; Rochman et al., 2013; Wright & Kelly, 2017). The tendency of microplastics to adsorb and react with wastewater agents is relatively high due to their physical properties, such as hydrophobicity (Nikpay, 2021), as well as the large ratio of their surface area to volume, allowing them to adsorb toxic pollutants (e.g., heavy metals) and invasive species (Bakir et al., 2014). Microplastics are classified into two categories: primary and secondary. Primary microplastics are mainly detected with an original size of less than 5 mm in textiles and some personal care products (Bergmann et al., 2015; Cole et al., 2011). They can be transported through discharges of water treatment plants, rivers, surface run-off, and wind into aquatic environments (Gall & Thompson, 2015). Large plastic debris under fragmentation may produce secondary microplastics through some processes including physical, chemical, and biological interactions and photo-degradation (Galgani et al., 2013; Thompson et al., 2009). The secondary microplastics originate mainly from industrial resin pellets, fishing nets, and other thrown-away plastic litters (Eerkes-Medrano et al., 2015), and they can also be formed from the fragmentation of any larger plastic particle in the ocean, regardless of its source. Microplastics in the environment majorly consist of secondary microplastics (Eriksen et al., 2013). The possibility of microplastics breaking down into nanoplastics may increase during their exposure to the environment, leading to higher environmental risks given the nano-size nature of these materials (Li et al., 2018). In addition, plastic pollution impacts have been observed at economic and social scales (Jeftic et al., 2009). The tourism industry accounts for a considerable percentage of the gross domestic product (GDP) of many countries, which indicates the market value of all services provided within a country's territory during a specific temporal period; thus, governments schedule various plans to attract more tourists and introduce different sightseeing places in order to boost tourism income. Nevertheless, beaches confront some challenges with respect to their sustainability in terms of preservation and operation from the touristic and economic perspectives. The uncontrolled release of microplastics causes the pollution of the seawater and the shore.

Plastic debris enters the ocean directly or through rivers by uncontrolled dumping from land-based or maritime sources, such as fishing or shipping sectors, and recreational activities (Galgani et al., 2015b; Ivar do Sul & Costa, 2013; Li et al., 2020). Plastics will be degraded and broken down into microplastics (i.e., particles less than 5 mm in size) after entering the ocean if not treated at early

stages. Microplastics are found throughout the water column in oceans and also on the seabed (Desforges et al., 2014; Woodall et al., 2014). Numerous studies have been conducted to quantify and characterize microplastics in aquatic environments (Eerkes-Medrano et al., 2015; Eriksen et al., 2013; Hartmann et al., 2015; Thompson et al., 2009) including lakes (Eriksen et al., 2013; Free et al., 2014), rivers (Klein et al., 2015; Kooi et al., 2016; Lechner et al., 2014; McCormick et al., 2014; Yonkos et al., 2014), and shorelines (Browne et al., 2011) by employing different field surveys and using a set of lab experiments. Recent advances in computer science and technology have also promoted the application of Machine Learning (ML) approaches in the automated quantification and characterization of microplastics (Girshick, 2015; Girshick et al., 2014; Liu et al., 2016; Lorenzo-Navarro et al., 2021; Redmon et al., 2016; Ren et al., 2015).

Microplastics in water undergo some transformational processes such as biofouling (Kooi et al., 2017), degradation and fragmentation (Atugoda et al., 2020; Cole et al., 2011; Nikpay, 2022), and hetero- and homo-aggregation (Atugoda et al., 2020; Besseling et al., 2017), known also as particle–particle interactions (Van Sebille et al., 2020), which influence their fate in their receiving environment. Accordingly, their physical (mainly size, density, and shape), chemical, and biological properties may change as a result of their ambient environment properties, including sea surface temperature, sunlight, salinity, etc. The growth of ultrafine bacteria or microorganisms and the attachment of organic material, invertebrates, and algae on the exterior surfaces of these particles cause biofouling that results in not only density and size increases in the particles but consequently decreases buoyancy (Rummel et al., 2017). Thus, it can be concluded that the sinking process can be accelerated by biofouling (Ryan, 2015) and may result in the sedimentation of fouled particles. In addition, microplastics have been widely pervasive in marine habitats (Eriksen et al., 2014; Galgani et al., 2015b) due to physical transport processes including horizontal and vertical advection and diffusion. Previous studies have shown that microplastics have reached very remote regions in the Arctic (Obbard et al., 2014) and Antarctic (Lusher et al., 2015; Waller et al., 2017). They can be found on the sea surface (Cózar et al., 2014), the seabed (Galgani et al., 2000), and also in deep-sea sediments (Courtene-Jones et al., 2020; Peng et al., 2020). Predicting such transport processes, given their dependencies on different hydrological and atmospheric variables spanning over a wide temporal and spatial scale, is important for the accurate simulation of microplastics' fate and transport in water bodies. The transport of microplastics in water bodies is controlled by advection and dispersion driven by ambient currents, Stokes drift, sinking,

resuspension, beaching and washing-off, deposition, aggregation, degradation, and fouling, which need to be simulated by numerical models.

Four sources for transport processes can be considered: (1) ambient currents (e.g., tidal and wind-driven flows), leading to transport by advection; (2) wind-induced drift, i.e., windage, which is an additional advection term because of wind drag and has an undeniable effect on plastic particles' displacement (Van Utenhove, 2019)—in other words, the wind-driven drag force exerted on the water's surface causes the drifting of floating particles exposed to wind; (3) wave action; and (4) buoyancy, which influences the vertical transport. Indeed, the influence of buoyancy on vertical transport and associated vertical mixing can be significant (Zhang, 2017).

Physical processes involved in the transport and fate of microplastics can occur at different spatio-temporal scales, which makes the simulation challenging. In this respect, short-term processes (e.g., particle–particle interactions at local and regional scales) may last for several hours or a few days (Gouin et al., 2019); however, medium-term processes including biofouling, sedimentation, and advection from freshwater bodies to marine environments may occur within several days or weeks (Kooi et al., 2017). Long-term processes need months or even years to be completed (Jalón-Rojas et al., 2019). For instance, some processes, such as degradation (or fragmentation), sinking, and transport (due to advection and diffusion) from coastal water bodies to oceans are long-term processes that increase computational costs. From the spatial scale perspective, the simulation of physical processes in large study areas with global scales is of orders of thousands of square kilometers, while the computational domains for regional and local areas are of orders of hundreds and tens of square kilometers, respectively.

Numerical simulation has been widely employed in the past decades to predict marine microplastics' behavior (Ballent et al., 2012; Critchell et al., 2015; Critchell & Lambrechts, 2016; Declerck et al., 2019; Díez-Minguito et al., 2020; Pereiro et al., 2019; Raimundo et al., 2020). There are also some studies that have predicted the main sources, transport, and fate of microplastics under different environmental conditions based on numerical simulations (Isobe et al., 2019; Lebreton et al., 2012; Liubartseva et al., 2016; Maximenko et al., 2012; Van Sebille et al., 2015). Some of these studies have employed particle-tracking (Jalón-Rojas et al., 2019) and hydrodynamic models (Bondelind et al., 2020a), individually or coupled with each other (Alosairi et al., 2020; Collins & Hermes, 2019; Sousa et al., 2021). Numerical modeling is inexpensive by

far in comparison with experimental measurements and in situ observations and can predict potential accumulation zones in remote areas where water quality monitoring is not feasible. Furthermore, numerical models can simulate some key physical processes using fine grid resolution, given the ever-increasing computational capacity and the ongoing development of numerical techniques. Moreover, these models are capable of simulating different vertical and horizontal flow patterns encompassing microplastics with good accuracy.

Numerical simulations of microplastics' fate and transport in water are generally carried out using Eulerian and Lagrangian models. Unlike Lagrangian trajectory models that use a movable coordinate system in space, Eulerian grid models typically employ a non-movable frame of reference (Van Utenhove, 2019). In other words, a Lagrangian framework, known as the particle-tracking method, tracks only individual particles, while an Eulerian approach addresses advection and diffusion for given locations (computational nodes) (Van Sebille et al., 2018). Numerical Eulerian hydrodynamic models can be coupled with Lagrangian models. Accordingly, hydrodynamic modeling provides the ambient hydrological parameters as inputs for particle-tracking models (PTM), which are known as promising, cost-effective tools for interpreting the fate and transport of microplastics and providing better insights into microplastics' behavior in dynamic flow systems (Hardesty et al., 2017). Although some studies have used an Eulerian approach for the mixing and dispersion processes in dynamic water systems (Alosairi & Alsulaiman, 2019), some other studies have used Lagrangian models for tracking particles to investigate plastic particles' fate and transport (Van Utenhove, 2019). Lagrangian models solve for a lower number of equations per node so that they do not need to solve the equations for each location in the mesh. However, given the pros and cons of both Eulerian and Lagrangian approaches, they can be employed to complement each other. The particle-tracking model coupled with the hydrodynamic model can provide invaluable details about the potential trajectories of plastic litter from local (Lammerts, 2016; Rodríguez-Díaz et al., 2020; Stuparu et al., 2015) to global scales (Lebreton et al., 2012) that lead to the assessment of microplastics' transportation, distribution, residence time, and fate under various conditions (Carlson et al., 2017; Critchell & Lambrechts, 2016; Ebbesmeyer et al., 2012; Isobe et al., 2009; Lebreton et al., 2012; Liubartseva et al., 2018; Van Utenhove, 2019).

Particle-tracking methods simulate the trajectory of particles and their transport in water bodies. They are applicable to a wide range of plastic particles' transport in their surrounding environment (Lynch et al., 2014; Van Sebille et al., 2018). PTM has been employed in many studies as a reliable alternative for field surveys. This is due to the logistic challenges involved in field surveys (Hoffman & Hittinger, 2017; Lebreton et al., 2012; Mason et al., 2020; Maximenko et al., 2012; Van Sebille et al., 2012; Vennell et al., 2021). Most Lagrangian particle-tracking models do not simulate the flow hydrodynamics. They can be considered as an important tool to simulate physical processes and transport mechanisms that microplastics undergo.

Unlike the structured mesh, the unstructured mesh enables numerical models not only to mesh complex geometries more easily but also to address arbitrary positions, even though it should be noted that greater memory is needed for executing the simulation for unstructured mesh. Hydrodynamic values in each element of the Eulerian mesh are interpolated in the same location of the particle (as the host element) in PTM.

On the other hand, the spatio-temporal interpolation of the flow characteristics (mainly including the velocity, diffusivities, salinity, sea surface height, temperature, etc.) in both horizontal and vertical directions may be necessary, especially when the duration between successive hydrodynamic outputs is different in comparison with the time step of particles' motion. Thus, the hydrodynamic information provided on an Eulerian grid, as an input to the PTM model, should be interpolated for the spatio-temporal location of the particles before being read by the PTM (Jalón-Rojas et al., 2019). For instance, the particle's velocity at each location is found using the spatial and temporal interpolation of the hydrodynamic model's velocity.

Most available numerical models have limitations in considering all effective factors relevant to microplastics' fate and transport. For example, some models have ignored beaching, sinking, and fragmentation processes as well as biofouling, deposition, resuspension, washing-off from the beach, or wind drift (Critchell & Lambrechts, 2016; Ebbesmeyer et al., 2012; Murray et al., 2018).

Moreover, some physical properties of microplastics, including shape, size, and density, which are dominant factors related to microplastics' buoyancy and mobility (Browne et al., 2010; Chubarenko et al., 2016; Filella, 2015; Zhang, 2017), have not been parameterized in some numerical models. Furthermore, most of the aforementioned models use a 2D approach, neglect the dynamic behavior of microplastics, and only model marine debris neutral drifting within the

surface layers (Carlson et al., 2017; Ebbesmeyer et al., 2012; Isobe et al., 2009; Lebreton et al., 2012; Liubartseva et al., 2018; Murray et al., 2018).

Among the numerical models that are employed for the simulation of marine microplastics' behavior, we studied four PTMs, i.e., D-WAQ PART, Ichthyop, TrackMPD, and CaMPSim-3D. D-WAQ PART is the particle-tracking module of Delft-3D, which is an open-source simulating software equipped with different modules for predicting hydrodynamics in an aquatic environment. Ichthyop, as a free Java-based numerical model, has been employed for tracking plastic particles, although it has been originally used for studying the dynamics of ichthyoplankton. TrackMPD has been developed in recent years to simulate microplastic debris fates and transport. The latest developed numerical model that can be employed as a particle-tracking model is Canadian microplastic simulation (CaMPSim). It utilizes a coupling of an Eulerian and Lagrangian numerical model in the simulation of marine microplastics' behavior.

The current paper systematically reviews recent progress in the numerical modeling of the transport and distribution of microplastics in marine environments with the aims of (1) reviewing the structure of Lagrangian particle-tracking models, (2) determining the substantial improvements that are still needed, and (3) discussing the consideration of physical processes that microplastics undergo and their physical properties in the simulation of microplastics' fate and transport. In this respect, different 2D and 3D numerical models are categorized, as shown in Table 1.

Table 1. The most popular numerical 2D and 3D models used for simulating microplastics' fate and transport.

Particle-Tracking Model	Hydrodynamic Model	Dimensionality	Method	Simulating Fate or Transport	Ref.
D-WAQ PART	Delft3D-FLOW	2D/3D	Lagrangian	Transport	(Alosairi et al., 2020; Sousa et al., 2021)
Ichthyop	ROMS	2D/3D	Lagrangian	Transport	(Collins & Hermes, 2019;

Particle-Tracking Model	Hydrodynamic Model	Dimensionality	Method	Simulating Fate or Transport	Ref.
					Lett et al., 2008)
TrackMPD	OGCM [1]	3D	Lagrangian	Both	(Jalón-Rojas et al., 2019)
CaMPSim-3D	TELEMAC	3D	Lagrangian	Both	(Pilechi et al., 2022)

1 Ocean General Circulation Models.

2.3 Materials and Methods

As stated above, the concept and framework of different numerical models for modeling microplastics' fate and transport are reviewed in this study in detail, considering various ranges of microplastics' behavior characteristics and key physical processes affecting their variations. Lagrangian particle-tracking models are investigated in terms of considering physical properties (and hydrodynamic aspects), physical transformational processes, physical transport processes, and numerical schemes (Figure 1). In other words, the reviewed models have been compared based on capability in considering the physical properties of microplastics (mainly size, shape, and density), and in simulating the physical transformational and transport processes that microplastics undergo. Moreover, the numerical methods that have been employed by each of them in terms of considering the type of mesh they can read, their computational schemes, and the methods they employ for implementing interpolation have been addressed. Finally, limitations and gaps in the reviewed models and needed areas of improvement are determined and discussed in full.

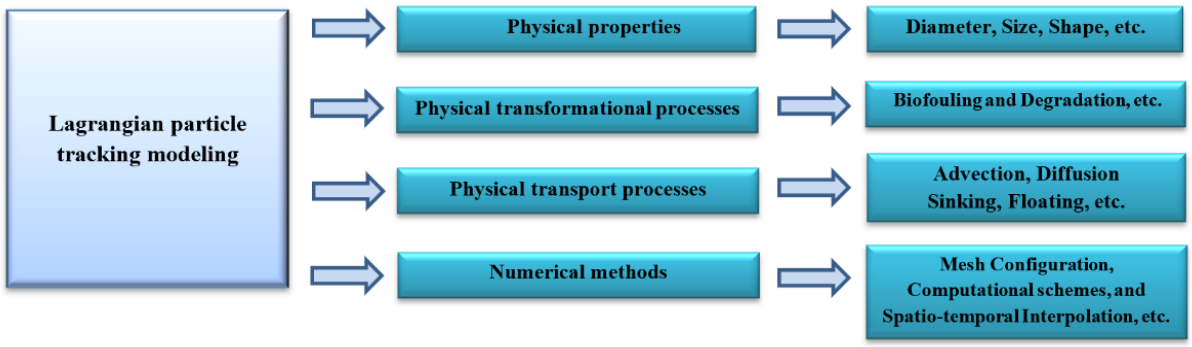

Figure 1. The structure of Lagrangian particle-tracking models in the simulation of microplastics' physical properties, physical transformation processes, physical transport processes, and numerical methods.

2.4 Physical Properties and Processes

2.1.1 Physical Properties

The behavior and transport of microplastics mainly depend on major physical properties including the size, density, and shape (Ballent et al., 2012; Chubarenko et al., 2016; Khatmullina & Isachenko, 2017; Kooi et al., 2017) of the particles. Microplastics are identified in varied sizes and shapes, and denser particles normally settle faster even with similar shapes and sizes (Kooi et al., 2017). Moreover, larger particles in terms of size but with the same density experience an increase in the ratio of the gravitational force applied on the particle to the fluid viscous resistance, which results in higher settling velocities and faster settling (Jalón-Rojas et al., 2019). In addition, the shape of microplastics can affect their movements and settling velocity as well (Isachenko et al., 2016). It has been observed that elongated particles such as films and fibers, known as larger particles, settle faster than smaller, circular particles (Chubarenko et al., 2016). Microplastics come in various regular (e.g., spherules, cylinders, and beads) and irregular shapes with different geometries (pellets and fibers). Regular shapes usually belong to primary microplastics while irregular shapes often can be seen among the secondary particles as a result of degradation (Khatmullina & Isachenko, 2017). Moreover, the physical properties of microplastics undergo changes due to the impacts of different processes and ambient factors such as algae invasion (Nava & Leoni, 2021), salinity (Liu et al., 2020), UV index (Miranda et al., 2021), temperature (Miranda et al., 2021), and Stokes drift generated by wave action (De Leo et al., 2021). For instance, unlike

freshly emitted particles, the edges of microplastics become smooth during aging as a result of mechanical degradation since they are under polishing imposed by other fragments (Doyle et al., 2011). Different equations used in the reviewed models for modeling hydrodynamic aspects (including microplastics' physical properties) pertinent to the transport of microplastics have been summarized in this study in Table 2.

Table 2. Various equations used for the modeling of hydrodynamic aspects in the reviewed models. *

No.	Mathematical or Empirical Relationships	Application	Defining Parameters	Employed in	Ref.
1	$v_s = c^n \times \left[A_0 + A_1 sin\left(\frac{2\pi(t+\emptyset)}{T}\right)\right]$	Settling velocity	v_s (ms^{-1}) is the settling velocity of each particle at time t (hours), c indicates the local concentration of particles (kgm^{-3}), n is the exponent for adjusting concentration-dependent settling velocities, A_0 (Hall, 2017) is the non-cyclic component of the settling velocity (ms^{-1}), A_1 represents the amplitude of a periodic sinusoidal variation in time (ms^{-1}), T is the period of the sinusoidal variation (hours), and $\emptyset$ is the phase lag for the sinusoidal variation (hours).	D-WAQ PART	(Deltares, 2021)
2	$v_s = \frac{\vartheta}{2R} d_*^3 (38.1 + 0.93 d_*^{12/7})^{-7/8}$	Settling velocity of	ϑ is the kinematic viscosity of water ($m^2 s^{-1}$), d_* represents the dimensionless diameter of	TrackMPD	(Khatmullina & Isachenko, 2017)

No.	Mathematical or Empirical Relationships	Application	Defining Parameters	Employed in	Ref.
		spherical particles	the particle, and R is the radius of the particle (mm).		
3	$d_* = 2R(g(\rho_p - \rho_w)/\rho_w \vartheta^2)^{1/3}$	Dimensionless diameter of the particle	g is the gravitational acceleration (ms^{-2}), and ρ_p and ρ_w indicate the density of the particle and the suspending medium, respectively, with the same units (gm^{-3}).		(Khatmullina & Isachenko, 2017)
4	$v_s = \frac{\pi}{2}\frac{1}{\vartheta} g \frac{(\rho_p - \rho_w)}{\rho_w} \frac{2RL}{55.238L + 12.6}$	Settling velocity of cylindrical particles	L indicates the length of cylinders (mm).		(Khatmullina & Isachenko, 2017)
5	$v_s = \sqrt{\frac{4}{3}\frac{d}{C_D}\left\lvert\frac{\rho_p - \rho_w}{\rho_w}\right\rvert g}$	Settling velocity	d is particle diameter (mm), ρ_p (gm^{-3}) and ρ_w (gm^{-3}) indicate the density of the particle and the surrounding medium, respectively, g is the gravitational acceleration (ms^{-2}), and C_D represents drag coefficient.	CaMPSim-3D	(Pilechi et al., 2022)
6	$C_D = \frac{24}{Re_p}\left(\frac{1-\Psi}{Re_p} + 1\right)^{0.25} + \frac{24}{Re_p}\left(0.1806 {Re_p}^{0.6559}\right)\Psi^{-{Re_p}^{0.08}} + \frac{0.4251}{1 + \frac{6880.95}{Re_p}\Psi^{5.05}}$	Drag coefficient	Re_p is particle Reynolds number and Ψ is the particle shape factor (Dioguardi et al., 2018). Equation (6) has been reported as the best fit for modeling drag when interpreting microplastics'		(Pilechi et al., 2022)

No.	Mathematical or Empirical Relationships	Application	Defining Parameters	Employed in	Ref.
			sinking (Van Melkebeke et al., 2020).		

586 * The Ichthyop model uses the Stokes law in calculating the settling velocity.

587 ### 2.1.2 Biofouling and Degradation (Physical Transformation Processes)

588 According to previous studies, microplastic particles are subjected to some natural transformation
589 processes including fouling, degradation, and mechanical breakdown during their residence time
590 in an aquatic ecosystem that may lead to changes in their physical properties (Van Utenhove,
591 2019). Biofouling is controlled by different ambient environmental factors such as temperature,
592 salinity, and the availability of sunlight, which is necessary for biofilm (including fine and ultrafine
593 organisms and plankton) growth (Collins & Hermes, 2019). On the other hand, particles become
594 more brittle and break apart into smaller pieces as a result of mechanical degradations by
595 weathering, wave actions, interaction with other particles, the seabed, and the shore (Andrady,
596 2011). Degradation is typically a slow process that takes over 50 years to be fully completed for
597 plastics since they are highly resistant to weathering (Andrady, 2011; Barnes et al., 2009).
598 However, in the swash zone (Efimova et al., 2018) and some energetic coastal areas (e.g., salt
599 marshes), natural abrasives including sediment and rock are present, and the degradation may be
600 completed sooner, even within 8 weeks based on (Weinstein et al., 2016), thereby affecting
601 seasonal microplastics' transport. The main equations employed in the reviewed models in this
602 study for considering biofouling and degradation processes are provided in Table 3. It should be
603 noted that none of the reviewed models are capable of simulating different types of aggregation.

604 **Table 3.** The main equations used in the reviewed models for the consideration of biofouling and
605 degradation.

No.	Mathematical or Empirical Relationships	Application	Defining Parameters	Employed in	Ref.
7	$\rho_p = \rho_0 \frac{R_0^3}{(R_0 + BT)^3} + \rho_D \left[1 - \frac{R_0^3}{(R_0 + BT)^3}\right]$	Biofouling of spherical particles	ρ_p (gm^{-3}) is the density of a fouled spherical particle, ρ_0 (gm^{-3}) is the density of a plastic particle, R (mm) indicates microplastic radius, and BT and ρ_D represent the thickness (µm) and density (gm^{-3}) of a biofilm layer, respectively.	TrackMPD–CaMPSim-3D	(Chubarenko et al., 2016)
8	$\rho_p = \rho_0 \frac{R_0^2}{(R_0 + BT)^2} + \rho_D \left[1 - \frac{R_0^2}{(R_0 + BT)^2}\right]$	Biofouling of cylindrical particles	ρ_p (gm^{-3}) is the density of a fouled cylindrical particle, ρ_0 (gm^{-3}) is the density of a plastic particle, R (mm) indicates microplastic radius, and BT (µm) and ρ_D (gm^{-3}) represent the thickness and density of a biofilm layer, respectively.	TrackMPD–CaMPSim-3D	(Chubarenko et al., 2016)
9	$BT = BT_0 + BR\Delta t$	Biofouling	BT_0 (µm) is the thickness of initial biofouling, BR is a constant biofilm thickness in stationary biofouling, and Δt indicates the time interval.	TrackMPD–CaMPSim-3D	(Jalón-Rojas et al., 2019)

10	$Size(D\ or\ L) = Size_0(1 - DR \cdot T/100)$	Degradation	D (mm) and L (mm) are the particle's diameter and length, respectively. $Size_0$ indicates the particle's initial diameter and length. DR as a constant rate shows the percentage of decrease in size of the particle per day (Weinstein et al., 2016), and T represents the duration of degradation from the beginning to the present time step.	TrackMPD–CaMPSim-3D	(Jalón-Rojas et al., 2019)

2.1.3 Physical Transport Processes

In addition to the transformation processes (biofouling, degradation, aggregation), numerical fate and transport models can simulate different physical processes driving microplastics' transport in water such as advection, diffusion, windage, resuspension, beaching, and washing-off. The transport of microplastics is generally governed by a generic advection–diffusion reaction, as follows (Pilechi et al., 2022):

$$\frac{\partial C}{\partial t} = \nabla.(CU) + \nabla.(K\nabla CU) + \rho(C) \quad (11)$$

where C indicates the concentration at time t, U is the velocity of a surrounding medium, K represents the dispersion coefficient, and $\rho(C)$ shows the reaction function.

Given the aforesaid concept, the main equations used in the reviewed models for addressing the main physical processes controlling microplastics' transport in aquatic systems are provided in Table 4.

618 **Table 4.** The mathematical or empirical equations employed in the reviewed models for
619 considering the physical transport processes that microplastics undergo in aquatic environments.

No.	Mathematical or Empirical Relationships	Application	Defining Parameters	Employed in	Ref.
12	$\frac{d\vec{X}(t)}{dt} = \vec{u}(X,t) + \frac{d\vec{X}'(t)}{dt}$	Trajectory Calculation	$\vec{X}$ is the 3D position vector with components in the horizontal plane, d is the total derivative, $\vec{u}$ is the 3D velocity vector, and $\vec{X}'$ is the fluctuation of the position vector.	D-WAQ PART	(Van Utenhove, 2019)
13	$V_{adv} = V_{flow} + V_{windage}$	Advection velocity	V_{adv} ($\mathrm{ms^{-1}}$) represents the velocity field, which is responsible for advection. V_{flow} ($\mathrm{ms^{-1}}$) is the velocity of flow, and $V_{windage} = C_{wd}(V_w - V_{flow})$. $\mathrm{C_{wd}}$ is an empirical wind drag coefficient that is related to particle characteristics and V_w ($\mathrm{ms^{-1}}$) represents the wind velocity at 10 m above sea level.		(Van Utenhove, 2019)
14	$K_{h(x,y)} = at^b$	Turbulent horizontal component of the diffusion coefficient	$K_{h(x,y)}$ is the horizontal component of the diffusion coefficient ($\mathrm{m^2 s^{-1}}$) at time t (which is defined from $t = 0$), a (which is equal to the	D-WAQ PART	(López et al., 2021)

No.	Mathematical or Empirical Relationships	Application	Defining Parameters	Employed in	Ref.
			dispersion coefficient for small t), and b ($\in$ [0,1]) are calibrating coefficients. It should be noted that the upper and lower limits of $K_{h(x,y)}$ are equal to at and a, respectively, and $K_{h(x,y)}$ increases with time. It has been used in Equation (11).		
15	$D_z = \frac{c_\mu^{1/4} L\sqrt{k}}{\sigma_C}$	Turbulent vertical diffusion coefficient	D_z is the vertical dispersion coefficient, C_μ indicates a calibrating constant for local equilibrium shear layers that is equal to 0.09, approximately. L is the mixing length (m), k represents turbulent kinetic energy, and σ_C is the Prandtl–Schmidt number. It has been used in Equation (11).	D-WAQ PART	(Deltares, 2021)
16	$P = 0.5^{-t/T}$	The probability of being washed-off	P is the probability of a particle being washed off, t is the time step, and T is	D-WAQ PART—TrackMPD	(Liubartseva et al., 2018)

No.	Mathematical or Empirical Relationships	Application	Defining Parameters	Employed in	Ref.
			the half-life of plastic litter.		
17	$v_{part} = v_{water} + \frac{1}{24} g d^2 \frac{\Delta\rho}{\rho_w} \vartheta^{-1} \ln\left(\frac{2I}{d} + \frac{1}{2}\right)$	Vertical velocity of particle	v_{water} is vertical velocity of water, g is the gravitational force (ms^{-2}), d and I are prolate spheroid axes (indicating the area of a particle), $\Delta\rho = \rho_{part} - \rho_w$, ρ_{part} (gm^{-3}) is particle density and ρ_w (gm^{-3}) is the density of water, and ϑ indicates the kinematic viscosity.	Ichthyop	(Parada et al., 2003)
18	$K_h = \varepsilon^{1/3} l^{4/3}$	Horizontal turbulent diffusion coefficient	ε is the turbulent dissipation rate and l is the cell size. It has been used in Equation (11).	Ichthyop	(Peliz et al., 2007)
19	$x_{n+1} = x_n + U\Delta t_i$ $y_{n+1} = y_n + V\Delta t_i$ $z_{n+1} = z_n + W\Delta t_i$	First-order Euler method for advection	Δt_i is an internal time interval and $U = (U, V, W)$ is the velocity vector. This is a first-order discretization of Equation (11).	TrackMPD	(Jalón-Rojas et al., 2019)
20	$x_{n+1} = x_n + R(2r^{-1} K_h \Delta t_i)^{1/2}$	Calculation of horizontal displacement due to	R indicates a random number with an average of zero and r is its standard deviation that equals 1,		(Jalón-Rojas et al., 2019)

No.	Mathematical or Empirical Relationships	Application	Defining Parameters	Employed in	Ref.
		diffusion Equation (11)	and K_h is horizontal diffusivity (m^2s^{-1}).		
21	$z_{n+1} = z_n + R(2r^{-1}K_v\Delta t_i)^{1/2}$	Calculation of vertical diffusion term Equation (11)	K_v is vertical diffusivity (m^2s^{-1}).		(Jalón-Rojas et al., 2019)
22	$U = \frac{U_f + U_w\sqrt{\frac{\rho_{air}}{\rho_w}\frac{S_{above}}{S_{below}}}}{1 + \sqrt{\frac{\rho_{air}}{\rho_w}\frac{S_{above}}{S_{below}}}}$	Velocity field as a function of current and wave velocities	U_f is the current velocity, U_w is the wind velocity, ρ_{air} and ρ_w indicate the density of air and water, S_{above} and S_{below} represent the cross-sectional areas of spherical and cylindrical particles in dry and wet conditions, respectively. Note that Equation (17) and (21) use the same principles and their difference is only in some coefficients.	TrackMPD	(Jalón-Rojas et al., 2019)
23	$\frac{S_{above}}{S_{below}} = \frac{2\pi}{(\alpha - sin\alpha)} - 1$	The ratio of the dry cross-sectional area of the particles to its wet cross-sectional area.	α is defined by Equation (24).		(Jalón-Rojas et al., 2019)

No.	Mathematical or Empirical Relationships	Application	Defining Parameters	Employed in	Ref.
24	$\alpha = 2arcccos\left(1 - \frac{h}{R}\right)$	Parameter for Equation (23)	h is the Archimedean force, R is the radius of the particle.		(Jalón-Rojas et al., 2019)
25	$\left(\frac{h}{R}\right)^2 \cdot \left(3 - \frac{h}{R}\right) = 4\frac{\rho}{\rho_w}$	Archimedean force	ρ (gm^{-3}) and ρ_w (gm^{-3}) are the density of the particle and water, respectively.		(Jalón-Rojas et al., 2019)
26	$R_j = R_{jmax}(\frac{\tau}{\tau_{crit}} - 1)$	Resuspension flux	R_{jmax} is the maximum resuspension constant for microplastics. τ and τ_{crit} are shear stress and critical shear stress, respectively.	CaMPSim-3D	(Blom & Aalderink, 1998)
27	$\tau = \rho_w(\frac{g^{0.5}v_w}{Chezy})^2$	Actual shear stress	ρ_w (gm^{-3}) is the density of seawater, g (ms^{-2}) is gravitational acceleration, v_w is the mean velocity of the seawater, and $Chezy$ is the Chezy coefficient ($\mathrm{m}^{0.5}\mathrm{s}^{-1}$).		(Blom & Aalderink, 1998)
28	$v_p = \frac{\sum_{i=1}^{6}\frac{1}{\propto_i}v_i}{\sum_{i=1}^{6}\frac{1}{\propto_i}} + v_s$	Vertical displacement velocity of particles	where v_p is the vertical displacement velocity of particles, v_i is particle velocity at the computational cells, $\propto_i$ is vertex, and v_s is particles settling/rising velocity (obtained from Equation (5)).	CaMPSim-3D	(Pilechi et al., 2022)

No.	Mathematical or Empirical Relationships	Application	Defining Parameters	Employed in	Ref.
29	$Diff = \frac{\partial K}{\partial X}\Delta t + R\left\{\sqrt{2K_p\left[X_p(t) + \frac{1}{2}\frac{\partial K}{\partial X}\Delta t\right]\Delta t}\right\}$	Calculation of diffusion term	where K is the diffusion coefficient (obtained from Equation (14)), Δt is the time step, R is a random number, and K_p is the diffusion coefficient.		(Pilechi et al., 2022)

620

621 **2.5 Numerical Lagrangian Models**

622 In PTM models, a velocity value is allocated to each particle. This is typically done by the
623 interpolation of values from an Eulerian hydrodynamic model onto the position of microplastic
624 particles. The advection velocity typically includes the settling velocity, the velocity of flow
625 provided by the hydrodynamic model, and a diffusion-based velocity that is randomly generated,
626 typically based on a Gaussian distribution (Collins & Hermes, 2019; Peliz et al., 2007). Many PTM
627 models use numerical methods such as the fourth-order Runge–Kutta method to solve equations
628 in time.

629 In most PTM models, the number of required particles will be determined based on several factors
630 such as the simulation period, the extent of particle dispersion, the cells' size in the computational
631 domain, computational resources, etc. (Deltares, 2021).

632 The majority of PTM models calculate the settling velocity considering the impacts of the
633 aforementioned physical properties such as density, size, and shape. The settling velocity of each
634 particle, v_s, is defined based on the relationships, as shown in Table 2.

635 **2.5.1 D-WAQ PART**

636 Delft3D, as open-source software, can be applied for simulating flows, the transport of sediments,
637 tidal currents, water quality, waves, etc. in various water settings. Delft3D has several modules as
638 shown in Figure 2. The modules are linked to each other in order to simulate the multi-dimensional
639 transport and hydrodynamics (in 2D or 3D) (Deltares, 2020). Particle transport and dynamical
640 spatial distribution are simulated by the PART module of Delft3D using particle-tracking

modeling using the inputs provided by the FLOW module (i.e., two- or three-dimensional flow data). In other words, velocity and other hydrodynamic parameters are computed by the FLOW module using an offline coupling and provided as inputs for the D-WAQ PART module.

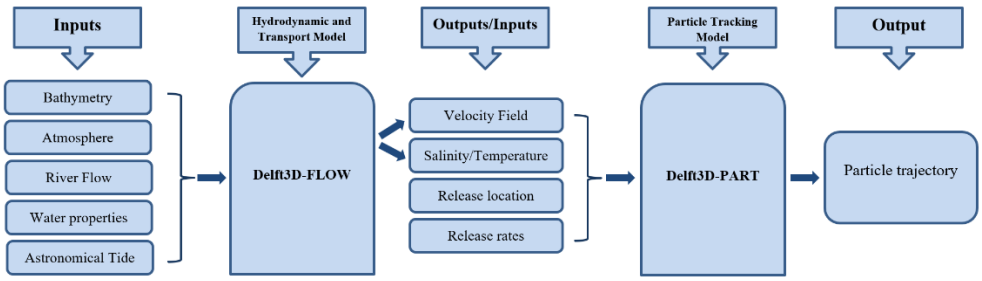

Figure 2. Schematic diagram of the Delft3D structure adapted from (Sousa et al., 2021), with permission from Elsevier, 2021.

D-WAQ PART is not capable of considering the impact of the biofouling process on the trajectories of micro-size particles via increasing the density and size of the particles since it cannot consider the thickness of the biofilm layer, and so, the density of a fouled particle. D-WAQ PART also lacks a specific tool to provide insight and appropriately predict complex processes including degradation as a long-term and aggregation as a short-term process.

Particle trajectories are computed over time in three dimensions by modeling the advection and dispersion processes (Rubinstein, 1981). As stated above, each individual particle can be advected by water currents and wind or wave drag as additional sources and also displaced randomly due to diffusion in order to explain unresolved processes.

The velocity of particles due to advection includes the local current velocity prepared by the hydrodynamic model in the Eulerian velocity field and the wind velocity at the location of a particle as shown in Equation (13) (Van Utenhove, 2019). The wind-drag coefficient is related to object characteristics as an empirical parameter. In addition, D-WAQ PART employs a random-walk particle-tracking model in order to describe the movement of particles due to diffusion processes. The diffusion is described using kinetic gas theory and the theory of Brownian motion (Deltares, 2021).

D-WAQ PART addresses beaching and washing-off using the probability of being washed off, as shown in Equation (16).

Many numerical models, including D-WAQ PART, are not capable of reading the unstructured mesh information provided by an Eulerian model. However, some of the other Delft-3D modules (e.g., D-Water Quality and GPP) can solve the advection–diffusion equation numerically on arbitrary, unstructured grids and structured, shaped grids such as triangles, rectangles, and curved elements.

On the other hand, D-WAQ PART utilizes the linear and block interpolation implemented for all time functions between time intervals (Deltares, 2021). In the linear interpolation, D-WAQ PART interpolates the hydrodynamic inputs linearly between the time records while it interpolates the two different subsequent inputs with similar time as the block interpolation.

2.5.2 Ichthyop

Ichthyop is a free Java-based particle tracking numerical model which was originally developed to study ichthyoplankton dynamics (Lett et al., 2008). Ichthyop has also been employed for modeling the fate and transport of microplastics and toxic algae (Collins & Hermes, 2019; Frere et al., 2017). The model can use three-dimensional hydrodynamic information including temperature, velocity, and salinity, simulated by oceanic numerical models such as the Regional Oceanic Modelling System, called ROMS, and the Model for Applications at Regional Scale, named MARS, as input (Lett et al., 2008). Ichthyop is capable of providing two types of microplastics simulations: (1) modeling plastic particle trajectories, and (2) ensemble simulation (i.e., executing a series of numerous particle tracking simulations) (Lett et al., 2008). Ichthyop can also simulate the trajectory of more than one million particles as passive tracers (Frere et al., 2017).

Similar to D-WAQ PART, Ichthyop does not consider the integration of complex particle transformation processes including biofouling, different types of aggregation, degradation, and fragmentation.

Ichthyop uses the Runge–Kutta method (Lett et al., 2008) for solving the advection equation (Collins & Hermes, 2019). Horizontal and vertical advection and dispersion can be simulated in Ichthyop (Collins & Hermes, 2019; Frere et al., 2017; Lett et al., 2008; López et al., 2021; Pilechi et al., 2022; Previmer, 2007). The model follows D-WAQ PART and uses Equation (11) to simulate the horizontal advection. Ichthyop utilizes a terminal velocity (v_{part}) in order to address the vertical movement of particles, as defined in Equation (17) (Parada et al., 2003).

Ichthyop uses Equation (18) for the consideration of horizontal diffusion. Accordingly, horizontal diffusion is defined as a function of the turbulent dissipation rate and the cell size of the computational domain (Peliz et al., 2007). Furthermore, the vertical diffusion of particles is predicted based on a proposed random-walk simulation (Visser, 1997).

Ichthyop is incapable of simulating some other effective physical processes on microplastics' fate and transport, such as beaching and washing-off, windage, resuspension, and aggregation, which can be regarded as an important limitation.

Hydrodynamic parameters are simulated on a rectangular structured mesh in some hydrodynamic models such as ROMS and MARS. Then, they are interpolated linearly and extracted at time steps in order to be prepared as inputs for Ichthyop.

2.5.3 TrackMPD

Amongst the three-dimensional numerical models, TrackMPD is an open-source model that has been released in recent years (Jalón-Rojas et al., 2019) based on the framework of the Particle Tracking and Analysis Toolbox (PaTATO) (Fredj et al., 2016). TrackMPD is compatible with various ocean models in order to address the fate and transport of marine microplastic debris in coastal areas. TrackMPD is capable of simulating microplastics' behavior in three dimensions considering different physical processes, including beaching and washing-off, biofouling and degradation, advection, windage, turbulent dispersion, and sinking, as well as different physical properties such as density (Equations (7) and (8)), size (Equation (10)), and shape (Equations (2)–(4), (7), and (8)). The physical properties of microplastics can be parametrized in TrackMPD, particularly in the calculation of the settling velocity. TrackMPD utilizes the empirical equations of (Khatmullina & Isachenko, 2017) and (Zhiyao et al., 2008) in estimating the settling velocity of microplastics with different shapes as a function of particle density and radius. Accordingly, the settling velocity (v_s) of spherical particles (ms^{-1}) is obtained based on a calibrated formulation provided by (Zhiyao et al., 2008), as shown in Equations (2) and (3), while this is different, as determined in Equation (4), for cylindrical fragments (mms^{-1}) (Khatmullina & Isachenko, 2017).

The effects of biofouling on the fate and transport of microplastics can be investigated by TrackMPD. In other words, TrackMPD uses some empirical equations in order to approximate the thickness of the biofilm layer. In this respect, the thickness of biofilm layers of spherical and

cylindrical particles can be estimated based on Equations (7) and (8), respectively (Chubarenko et al., 2016). Accordingly, biofilm thickness can be given either a constant or variable value over time. The case of constant biofilm thickness is referred to as stationary biofouling, while the case of variable biofilm thickness is considered as non-stationary biofouling.

TrackMPD simply predicts mechanical degradation by using an empirical relation (Equation (10)). In this respect, the size of plastic particles (their diameter or length) decreases based on a constant rate and time. While TrackMPD can simulate biofouling and degradation, it suffers from incapability in simulating some other transformational processes such as hetero- and homo-aggregation.

To simulate the horizontal and vertical movements of plastic particles due to advection, TrackMPD employs the Runge–Kutta method (Jalón-Rojas et al., 2019). In this respect, the velocity of the flow is calculated iteratively in three directions at the location of a particle to consider velocity values ($\mathrm{m s^{-1}}$) at past and future times. Then, to calculate particle displacements (m) and obtain their new location in each direction, the previous location of microplastics is added to the multiplication of the internal time interval (Δt_i) and the flow velocity's components ($U = (u, v, w)$), as shown in Equation (19). Moreover, the horizontal (in x or y directions) and vertical diffusion of particles is predicted in TrackMPD based on a random-walk model, as demonstrated in Equation (20) and (21), respectively (Jalón-Rojas et al., 2019).

As with D-WAQ PART, TrackMPD can consider the windage effect in the calculation of particle velocity. Accordingly, the horizontal wind-induced drift of microplastics is considered using Equations (22)–(25) (Jalón-Rojas et al., 2019).

TrackMPD estimates the probability of microplastics' washing-off based on a Monte Carlo method, as shown in Equation (16) (Jalón-Rojas et al., 2019). The probability (P) of being washed off in TrackMPD is an exponential function of the time step (t), and the half-life of plastic litter (T) is equal to the time that microplastics remain on the beach (Liubartseva et al., 2018). If P is higher than a random number, which varies from 0 to 1, beached microplastics can be transported (i.e., washed off) seaward at extreme tides. D-WAQ PART uses a basically similar approach in the calculation of the probability of wash-off.

Currently, TrackMPD can read hydrodynamic parameters off-line from some models such as ROMS in only a rectangular structured mesh. Moreover, hydrological properties are interpolated spatially at each time step, and then the hydrodynamic model assigns the values to particles located in the corresponding grid cells of TrackMPD (Jalón-Rojas et al., 2019).

2.5.4 CaMPSim-3D

Canadian microplastic simulation (CaMPSim), the newest three-dimensional Eulerian–Lagrangian framework (Pilechi et al., 2022), has been developed recently for simulating microplastics' fate and transport in different aquatic environments. CaMPSim-3D is based on the coupling of a three-dimensional Lagrangian particle-tracking model and TELEMAC modeling system as the Eulerian hydrodynamic numerical model. Similar to procedures followed by the aforesaid models, hydrodynamic inputs such as atmospheric pressure, the direction and speed of the wind, hydrodynamic and water quality parameters (including velocity, temperature, salinity, water level, and algae concentration), wave height and direction as well as its time period, and characteristics of suspended sediments that are all prepared by the Eulerian model are fed into the Lagrangian particle-tracking model. On the other hand, CaMPSim-3D considers the physical properties of microplastics (such as density, size, and shape) and physical processes (including the effect of positive/negative buoyancy, advection, biofouling, spatio-temporal varying diffusion, degradation, washing-off, and beaching, etc.).

In CaMPSim-3D, the physical properties of plastic particles such as density, diameter, gravity, and shape are parameterized in the calculation of the rising or settling velocity. Unlike TrackMPD, the formulation employed in CaMPSim-3D for calculating the settling velocity can be used for particles with different shapes, such as spherules, films, fragments, and fibers (Pilechi et al., 2022). CaMPSim-3D calculates the settling velocity (v_s) based on force balance formulation Equations (5) and (6) provided for Newtonian fluids (Pilechi et al., 2022). CaMPSim-3D can predict the formation of biofilm layers on plastic particles. In this respect, CaMPSim-3D utilizes some proposed empirical equations for estimating the biofilm thickness, e.g., Equations (7)–(9). In addition, CaMPSim-3D considers the degradation of microplastics based on empirical relationships provided in the literature, e.g., Equation (10). However, it cannot simulate both types of aggregation (i.e., hetero- and homo-aggregation) that microplastics undergo.

As with some of the aforementioned models, the Lagrangian particle-tracking model, CaMPSim-3D, can simulate not only the advection and diffusion of particles but also beaching and washing-off. It is also capable of considering the effect of buoyancy on particle movement (Pilechi et al., 2022). In CaMPSim-3D, the displacement of particles due to horizontal and vertical advection is calculated by solving the first- to the fourth-order of Equations (19)–(21). In addition, the vertical displacement velocity of particles (v_p) is calculated based on the vertical component of flow velocity, and particle settling/rising velocity (v_s, obtained from Equation (5)), as shown in Equation (28) (Pilechi et al., 2022). Furthermore, CaMPSim-3D considers the impact of wind as a driving factor on the transport of microplastics (see Equations (20)–(22). The turbulent diffusion of plastic particles is simulated in CaMPSim-3D by using a modified relationship, as shown in Equation (29) as a function of K (diffusion coefficient, see Equation (14)), Δt (the time step), R (a random number obtained from a normal distribution, which varies between -1 and 1), and K_p (diffusion coefficient at X_p as a function of t) (Pilechi et al., 2022).

K_p is calculated using the eddy viscosity (ϑ_t) calculated by the Eulerian hydrodynamic model (Pilechi et al., 2022). Moreover, CaMPSim-3D predicts resuspension and deposition as well as beaching and washing-off using the proposed relationships (see Equation (16)).

One of the advantages of CaMPSim-3D, in comparison with the aforesaid models, is its ability to employ an unstructured grid (Pilechi et al., 2022). It should be mentioned that the CaMPSim-3D model reads hydrodynamic parameters from an Eulerian hydrodynamic model (TELEMAC). Although this approach has some benefits by reducing interpolation errors, it imposes more computational time for point locations in an unstructured mesh. Furthermore, CaMPSim-3D employs an inverse distance-weighted method for the interpolation (or map) of hydrodynamic inputs in space, which is implemented for each particle (Pilechi et al., 2022).

2.6 Results and Discussion

Despite the fact that the reviewed models have generally acceptable accuracy in simulating the physical transformational and transport processes, each has some noticeable limitations in this regard. In this section, we have tried to discuss the reviewed models' limitations in detail regarding the consideration of microplastics' physical properties and processes. It can be concluded that this section can give better insights into the current gaps in the reviewed models.

D-WAQ PART and Ichthyop assume microplastics as passive particles without inertia when they are floated at the sea surface, which is different in real ocean conditions (Frere et al., 2017; Van Utenhove, 2019) since the shape and geometry of microplastics have impacts on their behavior, particularly during the different physical processes that they undergo. TrackMPD considers plastic particles as both active and passive particles using different scenarios. It means TrackMPD can simulate microplastics with different shapes (spherical and cylindrical) and sizes (Jalón-Rojas et al., 2019). CaMPSim-3D is more powerful in this regard in comparison with the aforesaid models. This is because it utilizes the shape factor (Ψ) which capable CaMPSim-3D in considering particles with different sphericity and circularity (Pilechi et al., 2022).

As stated in Section 2.5, D-WAQ PART and Ichthyop cannot simulate biofouling and degradation, while both TrackMPD and CaMPSim-3D are capable of simulating these processes using the same empirical relationships. It should be noted that TrackMPD and CaMPSim-3D cannot simulate biofouling and degradation together within the same simulation. On the other hand, there are some other transformational processes in the real ocean condition such as hetero- and homo-aggregation (Domercq et al., 2022) and agglomeration (known as the formation of particle clusters in which weak physical interactions are dominant between particles (Sturm et al., 2021)). In addition, microplastics undergo weathering, photodegradation, chemical and biological degradation, and defouling (known as the biofilm layer disintegration (Kooi et al., 2017)) in real conditions. However, none of the reviewed models can simulate any of the aforementioned processes yet.

Unlike Ichthyop, D-WAQ PART, TrackMPD, and CaMPSim-3D can predict beaching and washing-off using a probability empirical theory with the same accuracy. However, actual beaching and washing-off in the real condition are highly complex processes since they depend on many other factors, such as the characteristics of winds, tides, waves, and coastline structure (Van Utenhove, 2019). Moreover, microplastics may undergo stranding at the shoreline and be washed off from it repeatedly in subsequent episodes. Accordingly, the aforesaid models are currently incapable of simulating beaching and washing-off more accurately.

All of the reviewed models can predict advection and diffusion; however, their accuracy in this regard is different. All models can simulate advection and windage (except for Ichthyop). Moreover, all of them are capable of modeling horizontal and vertical diffusion, although some of them employ different methods and relationships in calculating the horizontal/vertical diffusion

coefficient. However, CaMPSim-3D utilizes a modified relationship for the calculation of turbulent diffusion, which seems to be a more accurate approach in comparison with the methods employed by other models. Among the reviewed models, only CaMPSim-3D can predict resuspension. On the other hand, there are some additional important driving transport processes such as Stokes drift (as a result of wave action (De Leo et al., 2021; Van Utenhove, 2019)), burial into the deep sediment of the waterbodies (Domercq et al., 2022), and remobilization (Liro et al., 2020), which none of the reviewed models can predict.

All of the reviewed models (except for CaMPSim-3D) are incapable of reading hydrodynamic parameters from an unstructured mesh provided by an Eulerian model. It should be noted that although reading hydrodynamic data from an unstructured mesh leads to a decrease in interpolation errors, it increases the computational costs of particle-tracking simulations.

D-WAQ PART and TrackMPD can read and then simulate spatio-temporally interpolated hydrodynamic parameters, while Ichthyop is only capable of utilizing temporally interpolated data. CaMPSim-3D can consider only spatially interpolated hydrodynamic values in the particle-tracking of plastic particles. It seems D-WAQ PART and TrackMPD utilize more accurate numerical schemes in this regard. On the other hand, the efficiency and computational speed of each of the reviewed models can be compared in systematic case studies. It should be noted that there are other numerical models such as TRACMASS and OceanParcels which have not been reviewed in this paper for the sake of briefness and to focus on models with more capabilities.

To make a general comparison among the reviewed models, the main characteristics and capabilities of the reviewed models have been summarized in Table 5. It can be seen which of the reviewed models are free for non-commercial use. Moreover, the capability of the reviewed models in terms of the particle tracking of what type and shape of particles have been compared. In addition, the main physical transformational and transport process each model can simulate are shown.

867 **Table 5.** Summary of the main information of the reviewed models.

Particle-Tracking Model	Open Access (Free to Use)	Application (Particle Tracking of)	Shape and Type of the Simulated Particles	Main Mechanism Can be Simulated	Initial Year of Release *	Ref.
D-WAQ PART	No	Microplastics, Sediments (first-order decaying substances)	Different shapes and types	Advection (and windage), Diffusion, Beaching and washing-off, Sinking	2019	(Alosairi et al., 2020; Sousa et al., 2021)
Ichthyop	Yes	Microplastics	Prolate spheroids	Advection, Diffusion, Sinking	2008	(Collins & Hermes, 2019; Lett et al., 2008)
TrackMPD	Yes	Microplastics	Spherical and cylindrical particles	Advection (and windage), Diffusion, Beaching and washing-off, Sinking, Biofouling, Degradation	2019	(Jalón-Rojas et al., 2019)
CaMPSim-3D	Yes	Microplastics	Spherules, films, fragments, and fibers	Advection (and windage), Diffusion, Beaching and washing-off, Sinking,	2021	(Pilechi et al., 2022)

				Biofouling, Degradation		

* Based on the publication date of the paper which introduces the model.

2.7 Conclusions and Future Research Directions

The current study aims, as a worthwhile endeavor, to systematically review some well-known Lagrangian numerical particle-tracking models that have been used for predicting the fate and transport of microplastics. In this regard, four Lagrangian particle-tracking models, i.e., D-WAQ PART, Ichthyop, TrackMPD, and CaMPSim-3D, have been investigated in terms of addressing physical transport processes (advection, diffusion, windage, beaching and washing-off, and resuspension) and physical transformation processes (biofouling and degradation) with consideration of the effects of the physical properties (mainly size, diameter, and shape) of microplastics on their fate and transport. Moreover, a numerical scheme of each model is described based on its spatio-temporal interpolation scheme and the structure of the adopted mesh. Accordingly, it has been shown that some of these models are more powerful than others in capturing the physical properties of particles and predicting their behavior under different physical transport and transformation processes. Some concluding remarks for the current study are summarized below:

- With respect to the consideration of the physical properties of microplastics, D-WAQ PART and Ichthyop use simplified equations for calculating the settling velocity as a function of the size and density of plastic particles, while TrackMPD and CaMPSim-3D employ more accurate equations to meet the effect of particle shape as well. In other words, D-WAQ PART utilizes an equation for calculating the settling velocity of plastic particles with different shapes and types, while Ichthyop is suited for considering the settling velocity of prolate spheroids. TrackMPD can differentiate spherical and cylindrical particles in the simulation of the settling velocity. CaMPSim-3D can be applied for simulating particles with different shapes, including spherules, films, fragments, and fibers.
- Among the transformation processes reviewed in this study (i.e., biofouling and degradation), although biofouling has been regarded as one of the important processes in the fate of microplastics, D-WAQ PART and Ichthyop are unable to predict the behavior of particles under the influence of this process. However, TrackMPD and CaMPSim-3D can simulate fouled particles using empirical equations. Unlike D-WAQ PART and

Ichthyop, TrackMPD, and CaMPSim-3D can predict the degradation of microplastics based on the proposed relationship in the literature.

- Four particle-tracking models employ generally universal advection–diffusion equations, while the equations for parameterizing various physical processes may be different. However, only D-WAQ PART, TrackMPD, and CaMPSim-3D consider the effect of wind-induced drift as an additional term of advection. In addition, all models are capable of meeting horizontal and vertical diffusion (dispersion). All reviewed models use spatio-temporally varying diffusion coefficients. D-WAQ PART, TrackMPD, and CaMPSim-3D can predict beaching and washing-off using some probability-based relationships.
- D-WAQ PART, Ichthyop, and TrackMPD can read the extracted hydrodynamic data and simulate particle behavior and particle trajectories only on a structured mesh, while CaMPSim-3D reads hydrodynamic data from an unstructured mesh system. Moreover, the hydrodynamic data are only interpolated linearly at each time step and prepared as inputs for Ichthyop. D-WAQ PART and TrackMPD utilize the spatio-temporal interpolation of the current characteristics, while CaMPSim-3D can use only spatially interpolated data.

Given the aforesaid descriptions, there are some physical transport and transformation processes that some of the studied models are unable to simulate or exhibit less accuracy for in modeling. In fact, in order to understand the impacts of microplastics on the sustainability of water resources comprehensively, with higher levels of accuracy, we need to fully understand their behavior, which can be elucidated by using a versatile and accurate modeling system. None of the reviewed models can simulate homo- and hetero-aggregation or agglomeration. None of the four models can predict photodegradation or chemical and biological degradation as important processes in the fate of plastic particles. Wave-induced drift as an additional advection is observed only in CaMPSim-3D. It is suggested that further studies be conducted in order to expand the current knowledge of microplastics' fate and transport. There are some important processes that need to be further studied with regard to the behavior of microplastics in the real condition (e.g., hetero- and homo-aggregation, agglomeration, weathering, photodegradation, chemical and biological degradation, defouling, resuspension, Stokes drift, and remobilization). More in-depth studies, as well as more accurate numerical models in capturing the microplastics' behavior, along with significant modifications in the numerical simulation structure of the reviewed models, are recommended for the future.

2.8 References

Alosairi, Y., Al-Salem, S., & Al Ragum, A. (2020). Three-dimensional numerical modelling of transport, fate and distribution of microplastics in the northwestern Arabian/Persian Gulf. Marine pollution bulletin, 161, 111723.

Alosairi, Y., & Alsulaiman, N. (2019). Hydro-environmental processes governing the formation of hypoxic parcels in an inverse estuarine water body: Model validation and discussion. Marine pollution bulletin, 144, 92-104.

Andrady, A. L. (2011). Microplastics in the marine environment. Marine pollution bulletin, 62(8), 1596-1605.

Atugoda, T., Piyumali, H., Liyanage, S., Mahatantila, K., & Vithanage, M. (2020). Fate and Behavior of Microplastics in Freshwater Systems. Handbook of Microplastics in the Environment, 1-31.

Bakir, A., Rowland, S. J., & Thompson, R. C. (2014). Transport of persistent organic pollutants by microplastics in estuarine conditions. Estuarine, Coastal and Shelf Science, 140, 14-21.

Ballent, A., Purser, A., de Jesus Mendes, P., Pando, S., & Thomsen, L. (2012). Physical transport properties of marine microplastic pollution. Biogeosciences Discussions, 9(12).

Barnes, D. K., Galgani, F., Thompson, R. C., & Barlaz, M. (2009). Accumulation and fragmentation of plastic debris in global environments. Philosophical transactions of the royal society B: biological sciences, 364(1526), 1985-1998.

Bergmann, M., Gutow, L., & Klages, M. (2015). Marine anthropogenic litter. Springer Nature.

Besseling, E., Quik, J. T., Sun, M., & Koelmans, A. A. (2017). Fate of nano-and microplastic in freshwater systems: A modeling study. Environmental pollution, 220, 540-548.

Blom, G., & Aalderink, R. H. (1998). Calibration of three resuspension/sedimentation models. Water science and technology, 37(3), 41-49.

Bondelind, M., Sokolova, E., Nguyen, A., Karlsson, D., Karlsson, A., & Björklund, K. (2020). Hydrodynamic modelling of traffic-related microplastics discharged with stormwater into the Göta River in Sweden. Environmental Science and Pollution Research, 27(19), 24218-24230.

Browne, M. A., Crump, P., Niven, S. J., Teuten, E., Tonkin, A., Galloway, T., & Thompson, R. (2011). Accumulation of microplastic on shorelines woldwide: sources and sinks. Environmental science & technology, 45(21), 9175-9179.

Browne, M. A., Galloway, T. S., & Thompson, R. C. (2010). Spatial patterns of plastic debris along estuarine shorelines. Environmental science & technology, 44(9), 3404-3409.

Carlson, D. F., Suaria, G., Aliani, S., Fredj, E., Fortibuoni, T., Griffa, A., Russo, A., & Melli, V. (2017). Combining litter observations with a regional ocean model to identify sources and sinks of floating debris in a semi-enclosed basin: the Adriatic Sea. Frontiers in marine science, 4, 78.

Chubarenko, I., Bagaev, A., Zobkov, M., & Esiukova, E. (2016). On some physical and dynamical properties of microplastic particles in marine environment. Marine pollution bulletin, 108(1-2), 105-112.

Cole, M., Lindeque, P., Halsband, C., & Galloway, T. S. (2011). Microplastics as contaminants in the marine environment: a review. Marine pollution bulletin, 62(12), 2588-2597.

Collins, C., & Hermes, J. (2019). Modelling the accumulation and transport of floating marine micro-plastics around South Africa. Marine pollution bulletin, 139, 46-58.

Courtene-Jones, W., Quinn, B., Ewins, C., Gary, S. F., & Narayanaswamy, B. E. (2020). Microplastic accumulation in deep-sea sediments from the Rockall Trough. Marine pollution bulletin, 154, 111092.

Cózar, A., Echevarría, F., González-Gordillo, J. I., Irigoien, X., Úbeda, B., Hernández-León, S., Palma, Á. T., Navarro, S., García-de-Lomas, J., & Ruiz, A. (2014). Plastic debris in the open ocean. Proceedings of the National Academy of Sciences, 111(28), 10239-10244.

Critchell, K., Grech, A., Schlaefer, J., Andutta, F., Lambrechts, J., Wolanski, E., & Hamann, M. (2015). Modelling the fate of marine debris along a complex shoreline: Lessons from the Great Barrier Reef. Estuarine, Coastal and Shelf Science, 167, 414-426.

Critchell, K., & Lambrechts, J. (2016). Modelling accumulation of marine plastics in the coastal zone; what are the dominant physical processes? Estuarine, Coastal and Shelf Science, 171, 111-122.

De Leo, A., Cutroneo, L., Sous, D., & Stocchino, A. (2021). Settling velocity of microplastics exposed to wave action. Journal of Marine Science and Engineering, 9(2), 142.

Declerck, A., Delpey, M., Rubio, A., Ferrer, L., Basurko, O., Mader, J., & Louzao, M. (2019). Transport of floating marine litter in the coastal area of the south-eastern Bay of Biscay: A Lagrangian approach using modelling and observations. Journal of Operational Oceanography, 12(sup2), S111-S125.

Deltares. (2020). Delft3D-FLOW User Manual.

Deltares. (2021). Delft3D-D-WAQ PART User Manual.

Desforges, J.-P. W., Galbraith, M., Dangerfield, N., & Ross, P. S. (2014). Widespread distribution of microplastics in subsurface seawater in the NE Pacific Ocean. Marine pollution bulletin, 79(1-2), 94-99.

Díez-Minguito, M., Bermúdez, M., Gago, J., Carretero, O., & Viñas, L. (2020). Observations and idealized modelling of microplastic transport in estuaries: The exemplary case of an upwelling system (Ría de Vigo, NW Spain). Marine Chemistry, 222, 103780.

Dioguardi, F., Mele, D., & Dellino, P. (2018). A new one-equation model of fluid drag for irregularly shaped particles valid over a wide range of Reynolds number. Journal of Geophysical Research: Solid Earth, 123(1), 144-156.

Domercq, P., Praetorius, A., & MacLeod, M. (2022). The Full Multi: An open-source framework for modelling the transport and fate of nano-and microplastics in aquatic systems. Environmental Modelling & Software, 148, 105291.

Doyle, M. J., Watson, W., Bowlin, N. M., & Sheavly, S. B. (2011). Plastic particles in coastal pelagic ecosystems of the Northeast Pacific ocean. Marine environmental research, 71(1), 41-52.

Ebbesmeyer, C. C., Ingraham, W., Jones, J. A., & Donohue, M. J. (2012). Marine debris from the Oregon Dungeness crab fishery recovered in the Northwestern Hawaiian Islands: identification and oceanic drift paths. Marine pollution bulletin, 65(1-3), 69-75.

Eerkes-Medrano, D., Thompson, R. C., & Aldridge, D. C. (2015). Microplastics in freshwater systems: a review of the emerging threats, identification of knowledge gaps and prioritisation of research needs. Water Research, 75, 63-82.

Efimova, I., Bagaeva, M., Bagaev, A., Kileso, A., & Chubarenko, I. P. (2018). Secondary microplastics generation in the sea swash zone with coarse bottom sediments: laboratory experiments. Frontiers in marine science, 5, 313.

Eriksen, M., Lebreton, L. C., Carson, H. S., Thiel, M., Moore, C. J., Borerro, J. C., Galgani, F., Ryan, P. G., & Reisser, J. (2014). Plastic pollution in the world's oceans: more than 5 trillion plastic pieces weighing over 250,000 tons afloat at sea. PLoS One, 9(12), e111913.

Eriksen, M., Mason, S., Wilson, S., Box, C., Zellers, A., Edwards, W., Farley, H., & Amato, S. (2013). Microplastic pollution in the surface waters of the Laurentian Great Lakes. Marine pollution bulletin, 77(1-2), 177-182.

EU. (2019). Environmental and Health Risks of Microplastic Pollution. European Commission.

Filella, M. (2015). Questions of size and numbers in environmental research on microplastics: methodological and conceptual aspects. Environmental Chemistry, 12(5), 527-538.

Fredj, E., Carlson, D. F., Amitai, Y., Gozolchiani, A., & Gildor, H. (2016). The particle tracking and analysis toolbox (PaTATO) for Matlab. Limnology and Oceanography: Methods, 14(9), 586-599.

Free, C. M., Jensen, O. P., Mason, S. A., Eriksen, M., Williamson, N. J., & Boldgiv, B. (2014). High-levels of microplastic pollution in a large, remote, mountain lake. Marine pollution bulletin, 85(1), 156-163.

Frere, L., Paul-Pont, I., Rinnert, E., Petton, S., Jaffré, J., Bihannic, I., Soudant, P., Lambert, C., & Huvet, A. (2017). Influence of environmental and anthropogenic factors on the composition, concentration and spatial distribution of microplastics: a case study of the Bay of Brest (Brittany, France). Environmental pollution, 225, 211-222.

Galgani, F., Hanke, G., & Maes, T. (2015). Global distribution, composition and abundance of marine litter. In Marine anthropogenic litter (pp. 29-56). Springer, Cham.

Galgani, F., Hanke, G., Werner, S., & De Vrees, L. (2013). Marine litter within the European marine strategy framework directive. ICES Journal of Marine Science, 70(6), 1055-1064.

Galgani, F., Leaute, J., Moguedet, P., Souplet, A., Verin, Y., Carpentier, A., Goraguer, H., Latrouite, D., Andral, B., & Cadiou, Y. (2000). Litter on the sea floor along European coasts. Marine pollution bulletin, 40(6), 516-527.

Gall, S. C., & Thompson, R. C. (2015). The impact of debris on marine life. Marine pollution bulletin, 92(1-2), 170-179.

Girshick, R. (2015). Fast r-cnn. Proceedings of the IEEE international conference on computer vision,

Girshick, R., Donahue, J., Darrell, T., & Malik, J. (2014). Rich feature hierarchies for accurate object detection and semantic segmentation. Proceedings of the IEEE conference on computer vision and pattern recognition,

Gouin, T., Becker, R. A., Collot, A. G., Davis, J. W., Howard, B., Inawaka, K., Lampi, M., Ramon, B. S., Shi, J., & Hopp, P. W. (2019). Toward the development and application of an environmental risk assessment framework for microplastic. Environmental toxicology and chemistry, 38(10), 2087-2100.

Hall, S. (2017). Rules of thumb for chemical engineers. Butterworth-Heinemann.

Hardesty, B. D., Harari, J., Isobe, A., Lebreton, L., Maximenko, N., Potemra, J., Van Sebille, E., Vethaak, A. D., & Wilcox, C. (2017). Using numerical model simulations to improve the understanding of micro-plastic distribution and pathways in the marine environment. Frontiers in marine science, 4, 30.

Hartmann, N., Nolte, T., Sørensen, M., Jensen, P., & Baun, A. (2015). Aquatic ecotoxicity testing of nanoplastics. LessonsLearnedFromNanoecotoxicology. DTU Environment.

Hoffman, M. J., & Hittinger, E. (2017). Inventory and transport of plastic debris in the Laurentian Great Lakes. Marine pollution bulletin, 115(1-2), 273-281.

Isachenko, I., Khatmullina, L., Chubarenko, I., & Stepanova, N. (2016). Settling velocity of marine microplastic particles: laboratory tests. EGU General Assembly Conference Abstracts,

Isobe, A., Iwasaki, S., Uchida, K., & Tokai, T. (2019). Abundance of non-conservative microplastics in the upper ocean from 1957 to 2066. Nature communications, 10(1), 1-13.

Isobe, A., Kako, S. i., Chang, P.-H., & Matsuno, T. (2009). Two-way particle-tracking model for specifying sources of drifting objects: application to the East China Sea Shelf. Journal of Atmospheric and oceanic technology, 26(8), 1672-1682.

Ivar do Sul, J. A., & Costa, M. F. (2013). Plastic pollution risks in an estuarine conservation unit. Journal of Coastal Research(65 (10065)), 48-53.

Jalón-Rojas, I., Wang, X. H., & Fredj, E. (2019). A 3D numerical model to track marine plastic debris (TrackMPD): sensitivity of microplastic trajectories and fates to particle dynamical properties and physical processes. Marine pollution bulletin, 141, 256-272.

Jeftic, L., Sheavly, S., Adler, E., & Meith, N. (2009). Marine litter: a global challenge.

Khatmullina, L., & Isachenko, I. (2017). Settling velocity of microplastic particles of regular shapes. Marine pollution bulletin, 114(2), 871-880.

Klein, S., Worch, E., & Knepper, T. P. (2015). Occurrence and spatial distribution of microplastics in river shore sediments of the Rhine-Main area in Germany. Environmental science & technology, 49(10), 6070-6076.

Koelmans, A. A., Bakir, A., Burton, G. A., & Janssen, C. R. (2016). Microplastic as a vector for chemicals in the aquatic environment: critical review and model-supported reinterpretation of empirical studies. Environmental science & technology, 50(7), 3315-3326.

Kooi, M., Nes, E. H. v., Scheffer, M., & Koelmans, A. A. (2017). Ups and downs in the ocean: effects of biofouling on vertical transport of microplastics. Environmental science & technology, 51(14), 7963-7971.

Kooi, M., Reisser, J., Slat, B., Ferrari, F. F., Schmid, M. S., Cunsolo, S., Brambini, R., Noble, K., Sirks, L.-A., & Linders, T. E. (2016). The effect of particle properties on the depth profile of buoyant plastics in the ocean. Scientific reports, 6(1), 1-10.

Lammerts, M. (2016). Marine litter in port areas-developing a propagation model.

Lebreton, L.-M., Greer, S., & Borrero, J. C. (2012). Numerical modelling of floating debris in the world's oceans. Marine pollution bulletin, 64(3), 653-661.

Lechner, A., Keckeis, H., Lumesberger-Loisl, F., Zens, B., Krusch, R., Tritthart, M., Glas, M., & Schludermann, E. (2014). The Danube so colourful: a potpourri of plastic litter outnumbers fish larvae in Europe's second largest river. Environmental pollution, 188, 177-181.

Lett, C., Verley, P., Mullon, C., Parada, C., Brochier, T., Penven, P., & Blanke, B. (2008). A Lagrangian tool for modelling ichthyoplankton dynamics. Environmental Modelling & Software, 23(9), 1210-1214.

Li, J., Liu, H., & Chen, J. P. (2018). Microplastics in freshwater systems: A review on occurrence, environmental effects, and methods for microplastics detection. Water research, 137, 362-374.

Li, Y., Zhang, H., & Tang, C. (2020). A review of possible pathways of marine microplastics transport in the ocean. Anthropocene Coasts, 3(1), 6-13.

Liro, M., Emmerik, T. v., Wyżga, B., Liro, J., & Mikuś, P. (2020). Macroplastic storage and remobilization in rivers. Water, 12(7), 2055.

Lithner, D., Larsson, Å., & Dave, G. (2011). Environmental and health hazard ranking and assessment of plastic polymers based on chemical composition. Science of the total environment, 409(18), 3309-3324.

Liu, P., Zhan, X., Wu, X., Li, J., Wang, H., & Gao, S. (2020). Effect of weathering on environmental behavior of microplastics: Properties, sorption and potential risks. Chemosphere, 242, 125193.

Liu, W., Anguelov, D., Erhan, D., Szegedy, C., Reed, S., Fu, C.-Y., & Berg, A. C. (2016). Ssd: Single shot multibox detector. European conference on computer vision,

Liubartseva, S., Coppini, G., Lecci, R., & Clementi, E. (2018). Tracking plastics in the Mediterranean: 2D Lagrangian model. Marine pollution bulletin, 129(1), 151-162.

Liubartseva, S., Coppini, G., Lecci, R., & Creti, S. (2016). Regional approach to modeling the transport of floating plastic debris in the Adriatic Sea. Marine pollution bulletin, 103(1-2), 115-127.

López, A. G., Najjar, R. G., Friedrichs, M. A., Hickner, M. A., & Wardrop, D. H. (2021). Estuaries as Filters for Riverine Microplastics: Simulations in a Large, Coastal-Plain Estuary. Frontiers in marine science, 26(715924).

Lorenzo-Navarro, J., Castrillón-Santana, M., Sánchez-Nielsen, E., Zarco, B., Herrera, A., Martínez, I., & Gómez, M. (2021). Deep learning approach for automatic microplastics counting and classification. Science of the total environment, 765, 142728.

Lusher, A. L., Tirelli, V., O'Connor, I., & Officer, R. (2015). Microplastics in Arctic polar waters: the first reported values of particles in surface and sub-surface samples. Scientific reports, 5(1), 1-9.

Lynch, D. R., Greenberg, D. A., Bilgili, A., McGillicuddy Jr, D. J., Manning, J. P., & Aretxabaleta, A. L. (2014). Particles in the coastal ocean: Theory and applications. Cambridge University Press.

Mason, S. A., Daily, J., Aleid, G., Ricotta, R., Smith, M., Donnelly, K., Knauff, R., Edwards, W., & Hoffman, M. J. (2020). High levels of pelagic plastic pollution within the surface waters of Lakes Erie and Ontario. Journal of Great Lakes Research, 46(2), 277-288.

Maximenko, N., Hafner, J., & Niiler, P. (2012). Pathways of marine debris derived from trajectories of Lagrangian drifters. Marine pollution bulletin, 65(1-3), 51-62.

McCormick, A., Hoellein, T. J., Mason, S. A., Schluep, J., & Kelly, J. J. (2014). Microplastic is an abundant and distinct microbial habitat in an urban river. Environmental science & technology, 48(20), 11863-11871.

Miranda, M. N., Sampaio, M. J., Tavares, P. B., Silva, A. M., & Pereira, M. F. R. (2021). Aging assessment of microplastics (LDPE, PET and uPVC) under urban environment stressors. Science of the Total Environment, 796, 148914.

Murray, C. C., Maximenko, N., & Lippiatt, S. (2018). The influx of marine debris from the Great Japan Tsunami of 2011 to North American shorelines. Marine pollution bulletin, 132, 26-32.

Napper, I. E., & Thompson, R. C. (2019). Marine plastic pollution: Other than microplastic. Waste,

Nava, V., & Leoni, B. (2021). A critical review of interactions between microplastics, microalgae and aquatic ecosystem function. Water Research, 188, 116476.

Nikpay, M. (2021). Wastewater Fines Influence the Adsorption Behavior of Pollutants onto Microplastics. Journal of Polymers and the Environment, 1-8.

Nikpay, M. (2022). Wastewater fines influence the adsorption behavior of pollutants onto microplastics. Journal of Polymers and the Environment, 30(2), 776-783.

Obbard, R. W., Sadri, S., Wong, Y. Q., Khitun, A. A., Baker, I., & Thompson, R. C. (2014). Global warming releases microplastic legacy frozen in Arctic Sea ice. Earth's Future, 2(6), 315-320.

Panno, S. V., Kelly, W. R., Scott, J., Zheng, W., McNeish, R. E., Holm, N., Hoellein, T. J., & Baranski, E. L. (2019). Microplastic contamination in karst groundwater systems. Groundwater, 57(2), 189-196.

Parada, C., Van Der Lingen, C., Mullon, C., & Penven, P. (2003). Modelling the effect of buoyancy on the transport of anchovy (Engraulis capensis) eggs from spawning to nursery grounds in the southern Benguela: an IBM approach. Fisheries oceanography, 12(3), 170-184.

Peliz, A., Marchesiello, P., Dubert, J., Marta-Almeida, M., Roy, C., & Queiroga, H. (2007). A study of crab larvae dispersal on the Western Iberian Shelf: Physical processes. Journal of Marine Systems, 68(1-2), 215-236.

Peng, G., Bellerby, R., Zhang, F., Sun, X., & Li, D. (2020). The ocean's ultimate trashcan: Hadal trenches as major depositories for plastic pollution. Water research, 168, 115121.

Pereiro, D., Souto, C., & Gago, J. (2019). Dynamics of floating marine debris in the northern Iberian waters: A model approach. Journal of Sea Research, 144, 57-66.

Pilechi, A., Mohammadian, A., & Murphy, E. (2022). A numerical framework for modeling fate and transport of microplastics in inland and coastal waters. Marine pollution bulletin, 184, 114119.

Previmer. (2007). ICHTHYOP, Lagrangian Tool for Modelling Ichthyoplankton Dynamics User Guide. In. France.

Raimundo, G. I., Sousa, M. C., & Dias, J. M. (2020). Numerical Modelling of Plastic Debris Transport and Accumulation throughout Portuguese Coast. Journal of Coastal Research, 95(SI), 1252-1257.

Redmon, J., Divvala, S., Girshick, R., & Farhadi, A. (2016). You only look once: Unified, real-time object detection. Proceedings of the IEEE conference on computer vision and pattern recognition,

Ren, S., He, K., Girshick, R., & Sun, J. (2015). Faster r-cnn: Towards real-time object detection with region proposal networks. Advances in neural information processing systems, 28, 91-99.

Rocha-Santos, T., & Duarte, A. C. (2015). A critical overview of the analytical approaches to the occurrence, the fate and the behavior of microplastics in the environment. TrAC Trends in analytical chemistry, 65, 47-53.

Rochman, C. M., Browne, M. A., Halpern, B. S., Hentschel, B. T., Hoh, E., Karapanagioti, H. K., Rios-Mendoza, L. M., Takada, H., Teh, S., & Thompson, R. C. (2013). Classify plastic waste as hazardous. Nature, 494(7436), 169-171.

Rodríguez-Díaz, L., Gómez-Gesteira, J., Costoya, X., Gómez-Gesteira, M., & Gago, J. (2020). The Bay of Biscay as a trapping zone for exogenous plastics of different sizes. Journal of Sea Research, 163, 101929.

Rubinstein, R. (1981). Simulation and Monte Carlo Method. New York: John & Wiley & Sons. In: Inc.

Rummel, C. D., Jahnke, A., Gorokhova, E., Kühnel, D., & Schmitt-Jansen, M. (2017). Impacts of biofilm formation on the fate and potential effects of microplastic in the aquatic environment. Environmental science & technology letters, 4(7), 258-267.

Ryan, P. G. (2015). Does size and buoyancy affect the long-distance transport of floating debris? Environmental research letters, 10(8), 084019.

Ryan, P. G., Moore, C. J., Van Franeker, J. A., & Moloney, C. L. (2009). Monitoring the abundance of plastic debris in the marine environment. Philosophical transactions of the royal society B: biological sciences, 364(1526), 1999-2012.

Sousa, M. C., DeCastro, M., Gago, J., Ribeiro, A. S., Des, M., Gómez-Gesteira, J. L., Dias, J. M., & Gomez-Gesteira, M. (2021). Modelling the distribution of microplastics released by

wastewater treatment plants in Ria de Vigo (NW Iberian Peninsula). Marine pollution bulletin, 166, 112227.

Stuparu, D., van der Meulen, M., Kleissen, K., Vethaak, A., & El Serafy, G. (2015). Developing a transport model for plastic distribution in the North Sea. 36th IAHR World Congress,

Sturm, M. T., Horn, H., & Schuhen, K. (2021). Removal of microplastics from waters through agglomeration-fixation using organosilanes—effects of polymer types, water composition and temperature. Water, 13(5), 675.

Thevenon, F., Carroll, C., & Sousa, J. (2014). Plastic debris in the ocean: the characterization of marine plastics and their environmental impacts, situation analysis report. Gland, Switzerland: IUCN, 52.

Thompson, R. C., Moore, C. J., Vom Saal, F. S., & Swan, S. H. (2009). Plastics, the environment and human health: current consensus and future trends. Philosophical transactions of the royal society B: biological sciences, 364(1526), 2153-2166.

Van Melkebeke, M., Janssen, C., & De Meester, S. (2020). Characteristics and sinking behavior of typical microplastics including the potential effect of biofouling: implications for remediation. Environmental science & technology, 54(14), 8668-8680.

Van Sebille, E., Aliani, S., Law, K. L., Maximenko, N., Alsina, J. M., Bagaev, A., Bergmann, M., Chapron, B., Chubarenko, I., & Cózar, A. (2020). The physical oceanography of the transport of floating marine debris. Environmental research letters, 15(2), 023003.

Van Sebille, E., England, M. H., & Froyland, G. (2012). Origin, dynamics and evolution of ocean garbage patches from observed surface drifters. Environmental Research Letters, 7(4), 044040.

Van Sebille, E., Griffies, S. M., Abernathey, R., Adams, T. P., Berloff, P., Biastoch, A., Blanke, B., Chassignet, E. P., Cheng, Y., & Cotter, C. J. (2018). Lagrangian ocean analysis: Fundamentals and practices. Ocean Modelling, 121, 49-75.

Van Sebille, E., Wilcox, C., Lebreton, L., Maximenko, N., Hardesty, B. D., Van Franeker, J. A., Eriksen, M., Siegel, D., Galgani, F., & Law, K. L. (2015). A global inventory of small floating plastic debris. Environmental Research Letters, 10(12), 124006.

Van Utenhove, E. (2019). Modelling the transport and fate of buoyant macroplastics in coastal waters.

Vennell, R., Scheel, M., Weppe, S., Knight, B., & Smeaton, M. (2021). Fast lagrangian particle tracking in unstructured ocean model grids. Ocean Dynamics, 71(4), 423-437.

Visser, A. W. (1997). Using random walk models to simulate the vertical distribution of particles in a turbulent water column. Marine Ecology Progress Series, 158, 275-281.

Wagner, M., & Lambert, S. (2018). Freshwater microplastics: emerging environmental contaminants? Springer Nature.

Waller, C. L., Griffiths, H. J., Waluda, C. M., Thorpe, S. E., Loaiza, I., Moreno, B., Pacherres, C. O., & Hughes, K. A. (2017). Microplastics in the Antarctic marine system: an emerging area of research. Science of the Total Environment, 598, 220-227.

Weinstein, J. E., Crocker, B. K., & Gray, A. D. (2016). From macroplastic to microplastic: Degradation of high-density polyethylene, polypropylene, and polystyrene in a salt marsh habitat. Environmental toxicology and chemistry, 35(7), 1632-1640.

Woodall, L. C., Sanchez-Vidal, A., Canals, M., Paterson, G. L., Coppock, R., Sleight, V., Calafat, A., Rogers, A. D., Narayanaswamy, B. E., & Thompson, R. C. (2014). The deep sea is a major sink for microplastic debris. Royal Society open science, 1(4), 140317.

Wright, S. L., & Kelly, F. J. (2017). Plastic and human health: a micro issue? Environmental science & technology, 51(12), 6634-6647.

Wright, S. L., Thompson, R. C., & Galloway, T. S. (2013). The physical impacts of microplastics on marine organisms: a review. Environmental pollution, 178, 483-492.

Yonkos, L. T., Friedel, E. A., Perez-Reyes, A. C., Ghosal, S., & Arthur, C. D. (2014). Microplastics in four estuarine rivers in the Chesapeake Bay, USA. Environmental science & technology, 48(24), 14195-14202.

Zhang, H. (2017). Transport of microplastics in coastal seas. Estuarine, Coastal and Shelf Science, 199, 74-86.

Zhiyao, S., Tingting, W., Fumin, X., & Ruijie, L. (2008). A simple formula for predicting settling velocity of sediment particles. Water Science and Engineering, 1(1), 37-43.

3 A Laboratory Dataset on Transport and Deposition of Spherical and Cylindrical Large Microplastics for Validation of Numerical Models

3.1 Abstract

The widespread presence of micro-sized plastic pollution has raised concerns due to their unique physical and toxic properties. Each year, water bodies carry millions of tons of plastic into the ocean. The inherent characteristics (such as size, shape, and density) of microplastics (MPs), along with flow factors like speed, depth, and pressure, significantly influence how MPs are transported and deposited. Therefore, this research aimed to gather experimental data on the transport and deposition of MPs to serve as a benchmark for numerical modeling. To achieve this goal, various test scenarios were set up in a straight channel flume to investigate different flow velocities, channel dimensions, and particle shapes. It was observed that cylindrical particles with the same density and similar size were more likely to become trapped compared to spherical particles. This study represents progress towards validating numerical models concerning the transport and deposition of microplastics.

3.2 Introduction

Oceans have been affected adversely because of the huge transport of plastic waste from lands, which occurs through different conduits, such as rivers, with an estimated annual rate ranging from 0.41 to 4.0 Mt (Corcoran et al., 2019). The presence of macro-(>1 cm) (N. I. B. Hartmann et al., 2015), meso-(5 mm–2 cm) (N. I. B. Hartmann et al., 2015), micro-(<5 mm) (Rocha-Santos & Duarte, 2015), and nano-sized (1–100 nm) (EU, 2019a) plastics has emerged as a significant environmental challenge due to their persistent nature, toxic properties, and detrimental impact on the Earth's hydrosphere (Barnes et al., 2009), aquatic organisms (Koelmans et al., 2016; Thevenon et al., 2014b), wildlife, and human health (Napper & Thompson, 2019; Wright & Kelly, 2017).

MPs exhibit diverse regular shapes (e.g., spherical, cylindrical, beads, and fibers) (Khatmullina & Isachenko, 2017) and irregular shapes (fragments) (Schwarzer et al., 2022). Furthermore, the physical properties of MPs undergo changes due to various processes and ambient environmental factors, such as algae invasion, salinity, UV index, temperature, and Stokes drift generated by wave action (De Leo et al., 2021; Liu et al., 2020; Miranda et al., 2021; Nava & Leoni, 2021). The interaction between microplastics and microalgae, including colonization and hetero-aggregation, alters the buoyancy of particles, affecting their settling and impacting their fate and transport in

surface waters (Nava & Leoni, 2021). On the other hand, microplastics pose a threat to microalgae, impeding their growth, diminishing chlorophyll levels and photosynthesis, and inducing morphological changes (Nava & Leoni, 2021). Aging MPs, in contrast to freshly emitted particles, exhibit smoother edges as a result of mechanical degradation caused by interactions with other fragments (Doyle et al., 2011).

The behavior and transport of MPs depend on their key physical attributes, including size, density, and shape (Bigdeli et al., 2022; Kooi et al., 2017). Denser particles settle faster, even when sharing similar shapes and sizes, and larger particles with the same density experience increased settling velocities due to the higher ratio of gravitational force to fluid viscous resistance (Jalón-Rojas et al., 2019). The shape of MPs also influences their movement and settling velocity, with elongated particles settling faster than smaller circular ones of comparable size (Decuzzi et al., 2005; Mason et al., 2020).

The prediction of MP transport and deposition considering their different physical properties is of great importance. In this regard, there are several ways to investigate the behavior of MPs within different water bodies. Physical modeling, numerical simulations, and field surveys have been the most popular methods employed in previous studies. Physical and numerical modeling serve as valuable tools for predicting the fate and transport of plastic debris, offering a potential solution to mitigate the plastic pollution problem. Numerical fate and transport models can simulate different physical processes driving MP transport in water, such as advection, diffusion, windage, resuspension, beaching, and washing-off as well as the transformation (biofouling, degradation, and aggregation) (Bigdeli et al., 2022). Laboratory experiments have been acknowledged as one of the principal approaches to obtain reliable outcomes. However, there are limitations to physical modeling, numerical simulations, and field analyses. Conducting physical modeling is expensive and may raise questions regarding scaling waterbody geometry and particle transport and deposition patterns, although it can provide reliable results. Numerical modeling can predict potential accumulation zones in remote areas where water quality monitoring is not feasible. Furthermore, numerical models can simulate some key physical processes using fine grid resolution, given the ever-increasing computational capacity and ongoing development of numerical techniques. Moreover, these models can accurately simulate different vertical and horizontal flow patterns encompassing microplastics. In this respect, numerical models can be

employed for predicting pathways, hot spots/accumulation zones, and potential sources of plastic pollution in different water settings promisingly (particularly in the calculation of mass balance and the estimation of moving plastic debris versus settled ones). Accordingly, numerical modeling can be considered a promising and relatively inexpensive tool in the simulation of MP behavior, but it must be validated using reliable experimental or field datasets. In other words, the lack of reliable datasets of different MPs in terms of physical properties limits the validation processes of numerical modeling approaches. It should be noted that such a validated numerical model, especially when coupled with field and lab data, can be substantially useful in providing accurate simulations. Field analysis is the most expensive choice when compared to the other two methods, and its feasibility may vary depending on the location and timing.

From a physical modeling perspective, simplified and generic experiments can be useful for generating reliable data for the validation of numerical models. In this regard, several studies have been conducted to experimentally investigate the transport and fate of MPs, which can be helpful in developing numerical methods for predicting MP behavior. For instance, a research study (Choi et al., 2022) sought to uncover and describe how the secondary movements of microplastic fibers impact their movement. Secondary movements refer to the oscillating movements exhibited by a particle as it descends in calm or still water. Another study (Boos et al., 2021) introduced an experimental configuration designed for the real-time tracking and measurement of microplastic quantities at the pore scale (ranging from 1 μm to 10 μm) in three distinct environments: (a) surface flow, (b) at the interface of the streambed, and (c) within hyporheic sediments within an experimental flume setting. To investigate the transportation and burial of MPs by turbidity currents, a previous study (Pohl et al., 2020) introduced microplastic fragments and fibers into scaled-down turbidity currents during flume experiments. The primary objective of this study was to assess the presence of MPs in sediment samples collected from turbidity currents and their resulting deposits. Another study (Kerpen et al., 2020) investigated the driving forces and processes that control the movement of microplastic particles and their accumulation in the surf zone. To achieve this goal, systematic physical model tests were conducted using MPs of various sizes, shapes, and densities. Additional experimental investigations were conducted (Waldschläger & Schüttrumpf, 2019) to assess the settling and rising velocities of microplastic particles in relation to their density, diameter, and shape. The objective was to explore whether the equations commonly used in sediment transport studies could be applied to MPs and, if necessary, develop

more suitable formulas. To ensure robust data and accuracy, the settling or rising rate of each particle was measured three times in separate experiments.

Given the aforementioned descriptions, it is crucial to thoroughly characterize and quantify the deposition of plastic debris in bed materials, especially when developing numerical models to simulate the fate and transport of plastic debris in water bodies. This information is vital for tasks such as mass balance calculations and the estimation of the transport of plastic debris versus their deposition. Accordingly, this study aimed to provide an experimental dataset that can be employed to validate numerical models utilized in the prediction of MP behavior in water bodies. In other words, we aimed to bridge the gap between our present knowledge regarding MP transport and deposition and what happens in real conditions when the velocity of the flow or the geometry of the channel changes by providing an experimental dataset.

This paper is organized as follows. Section 3.3 describes the experimental setup including details of the instrumentation, the physical characteristics of particles, the flow conditions, and the employed geometrical characteristics of the channel. Section 3.4 presents the experimental outcomes derived from four distinct cases, varying in terms of the flow velocity and particle shape. Section 3.5 discusses the implications of these observations, and provides concluding remarks based on the conducted experiments.

3.3 Experimental Setup

Physical testing was conducted in a tilting flume at the National Research Council Canada Ocean, Coastal, and River Engineering Research Centre (NRC-OCRE) physical testing facility in Ottawa (Figure 3). The model was constructed in a flume measuring 10 m in length, 40 cm in height, and 38 cm in width. It was built using plexiglass and PVC sheets with a thickness of 1 cm. The schematics of the model, illustrating its geometrical characteristics and dimensions of the different components, are shown in Figure 4.

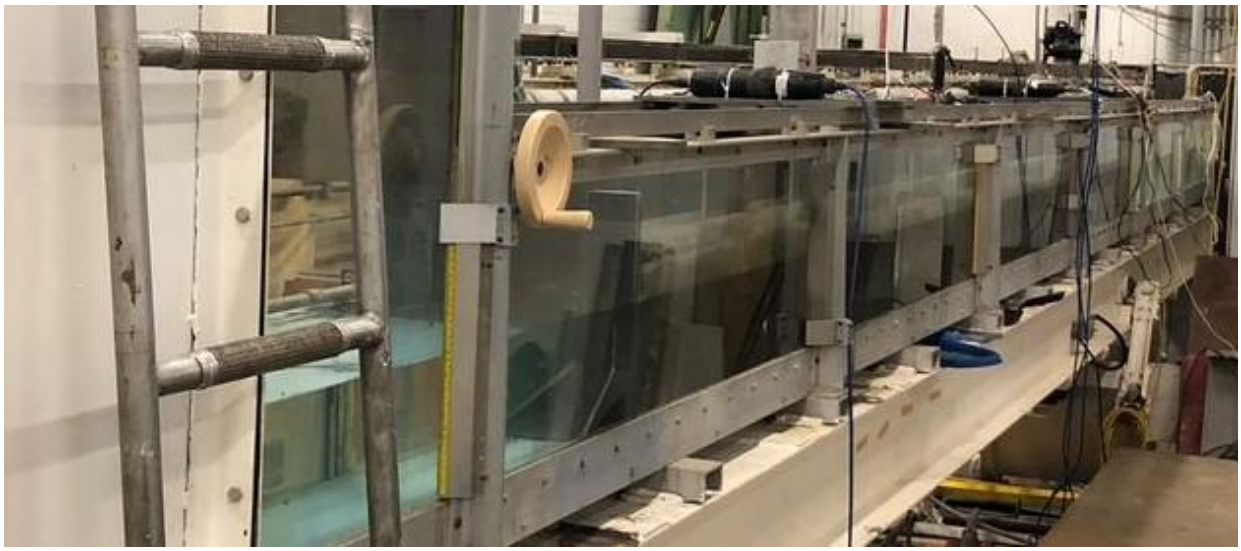

Figure 3. Tilting flume at NRC-OCRE.

The water surface elevations in the model were measured using three Nortek wave probes, which were mounted at different locations within the flume: first, at the very beginning of the flume (point 1 in Figure 4); second, in zone A, point 2, very close to the area where large expansion and deepening applied to the channel (i.e., zone B); and third (point 6), at the end of the flume just before the titling gate (comprised of a panel supported by a hinge along its lower side, allowing water to pass over it when it is lowered) and a screen for capturing particles before entering the basin. Mesh screens were placed before the first wave probe to help maintain a uniform and steady flow within the model. Moreover, the flume inlet started five meters ahead of zone B. Thus, the flow was fully developed before it reached this area.

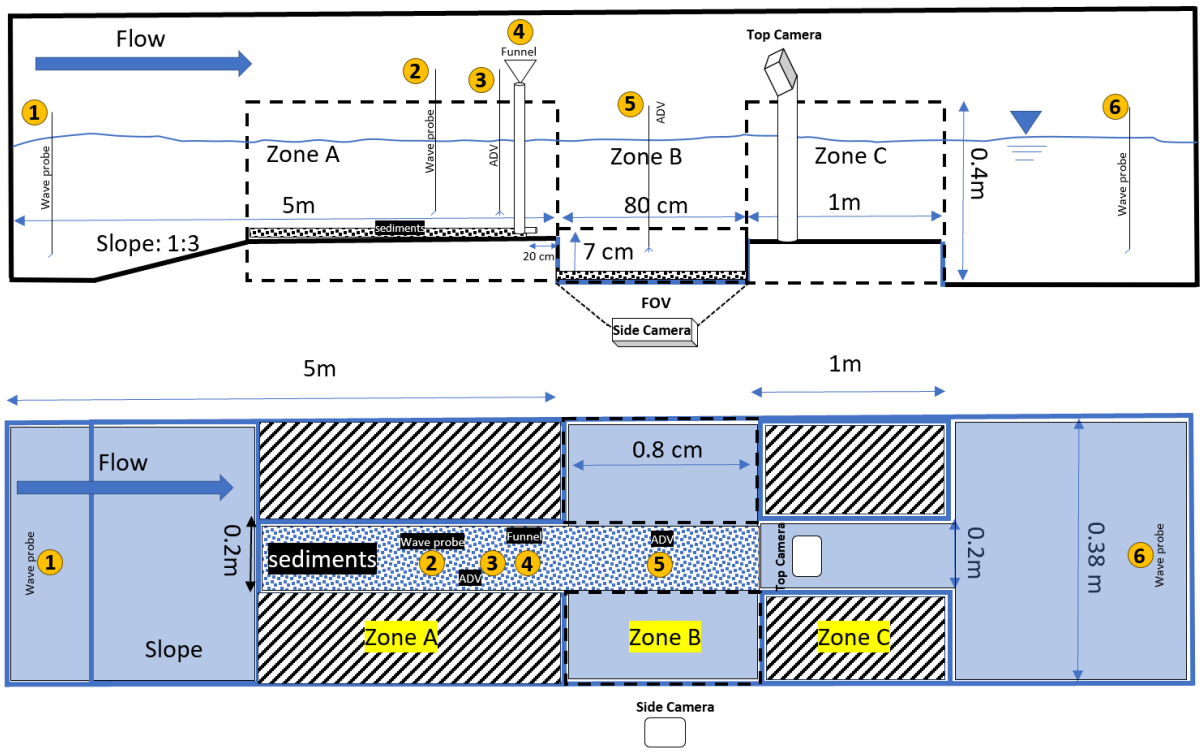

Figure 4. Schematic of the experimental setup: Top figure: Side view, Bottom figure: Top view.

As depicted in Figure 4, a ramp with a slope of 1:3 has been added at the initial section of the flume just before the channel that starts in zone A. This addition serves to elevate the bed of the channel and enables the creation of a larger depth area in zone B. In order to replicate river conditions, the model bed was covered with a layer of sediment (i.e., coarse sand (or pebble) (Middleton, 1976) with a mean diameter range of 4 mm ≤ D50 ≤ 6 mm) glued to the channel bed in zones A and B. The movement of particles within the channel was recorded by two high-resolution digital cameras positioned above (in zone C) and on the side (in zone B) of the flume at the locations shown in Figure 4. MPs were injected through funnels and injection tubes that were only five centimeters above the flume bed in zone A (Figure 4, point 4) and 20 cm away from the area of the channel (i.e., zone B) where large and moderate expansion and large deepening occurred. Thus, they were injected into the flow from a depth very close to the bed. This allowed the particles to be transported and deposited freely on the bed or between the sediments. Water velocity profiles were measured before and after the funnel and injection tubes to ensure that there was no regime change in the flow's condition in zone A and just before zone B due to the presence

of injection tubes. This setup covers the entire area of zone B. The field of view (FOV) for each of the mentioned cameras is illustrated in Figure 5.

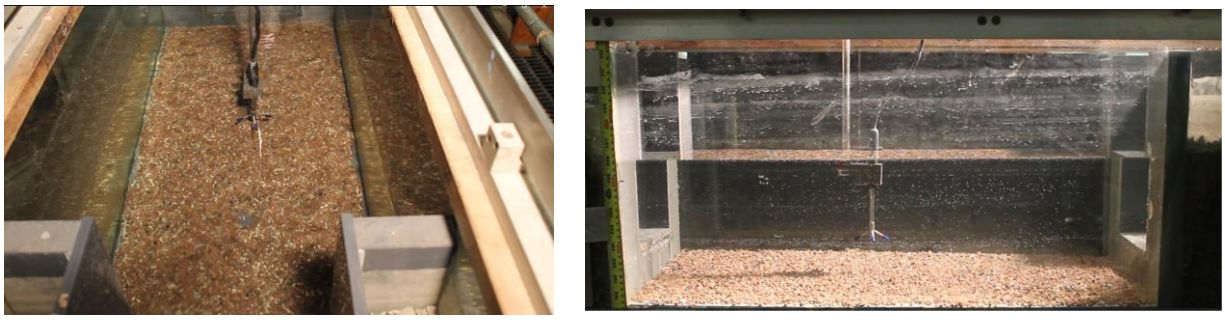

(**a**) (**b**)

Figure 5. FOV in the experimental setup from (a) top and (b) side view.

To circulate the flow within the flume, we employed an 8 psi pressure pump. Water velocities were measured using two Nortek Acoustic Doppler Velocimeter (ADV), an adaptable and precise device utilized for measuring three-dimensional water velocity, probes—one deployed (in zone A, point 3) very close to the funnels and injection tubes (in zone A, point 4) and the other in the middle of zone B, in point 5 (see Figure 4). The probes were mounted at 0.6 of the total depth from the water surface. Velocity measurements for each test were recorded at a frequency of 25 Hz for a duration of 5 min. The selection of this duration and frequency was part of an iterative process aimed at ensuring that the resolution and duration of the recorded data were sufficient in the sense that the slope of the spectrum of the measured velocity satisfied Kolmogorov's −5/3 law. The reported velocity magnitudes in this study are the averages of the recorded data over a 300 s measurement period.

The time of each test started 100 s before releasing the particles and it lasted five minutes. The experiments were repeated three times for each test, and all were recorded using a digital camera to track the particle path, ensuring minimized errors and uncertainties.

The experiments were conducted using fresh water with a density of 1000 kg/m3. Two types of microplastic particles, polyethylene terephthalate (PET) and polyvinyl chloride (PVC), each with an approximate density of 1380 kg/m^3, were used for testing. The PET and PVC particles were shaped as spherical and cylindrical particles, respectively (Figure 6).

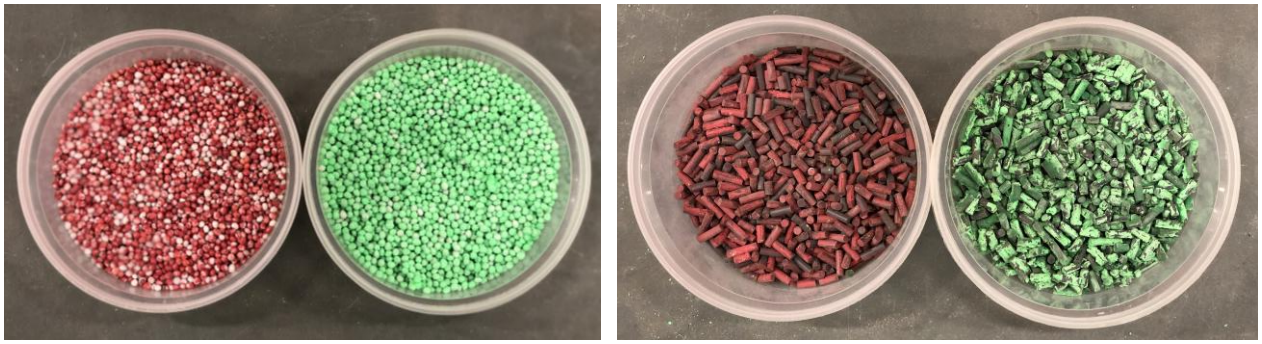

(**a**) (**b**)

Figure 6. Particles used in the experiments. (**a**) Spherical. (**b**) Cylindrical.

The diameters of both the spherical and cylindrical particles were 3 mm, and the average length of the cylindrical particles was 4 mm.

The spherical and cylindrical particles were coated both in green and red. They were coated with waterproof dyes in order to differentiate them along the channel's bed. The density of the coated particles was checked very carefully to see if the coating changed their density, and we found that the change in their density was negligible. The green particles were injected into the flow from the middle funnel while the red particles reached the channel through two side funnels, as shown in Figure 7. The experiments were performed for two flow velocities, 0.1 m/s and 0.5 m/s, at the location of the first ADV (i.e., zone A, point 3 in Figure 4). However, because of expansion and deepening, the velocities in zone B were much less than 0.1 m/s and 0.5 m/s; thus, the particles had more time to settle and dynamically interact with the near-bed flow.

Figure 7. Injection tubes across the channel's width.

3.3.1 Experimental Cases

Multiple model setups were constructed, incorporating both expansions in the width of the channel along with increases in the depth of the channel. Four test series were defined for this study based on two particle shapes (spherical and cylindrical) and two flow conditions (0.1 m/s and 0.5 m/s), as outlined in Table 6. Each test series involved the examination of two width and depth values for the expansion region, resulting in a total of 16 tests.

Table 6. Experimental cases implemented in this study.

Case	Flow Velocity (m/s)	Deepening in Depth (cm)	Expansion in Width (cm)	Material	Shape
Case 1—Spherical MP deposition in channel with a low velocity of flow	Low velocity U = 0.1 m/s	0 and 7	10 and 18	PET	Spherical
Case 2—Spherical MP deposition in channel with a high velocity of flow	High velocity U = 0.5 m/s	0 and 7	10 and 18	PET	Spherical
Case 3—Cylindrical MP deposition in channel with a low velocity of flow	Low velocity U = 0.1 m/s	0 and 7	10 and 18	PVC	Cylindrical
Case 4—Cylindrical MP deposition in channel with a high velocity of flow	High velocity U = 0.5 m/s	0 and 7	10 and 18	PVC	Cylindrical

On the other hand, the aforesaid cases were classified as shown in Table 7 in terms of large deepening or moderate and large expansion in the width of the channel. Both expansion and deepening were applied to the channel in zone B. The expansion applied to the width of the channel and increased its value from 20 cm to 38 cm within zone B. In addition, deepening made the channel bed 7 cm deeper in zone B.

Table 7. Definition of large and moderate expansion in this study.

Case	Test	Flow Velocity (m/s)	Water Surface Elevation (cm)	Channel Depth at Zone B (cm)	Channel Width at Zone B(cm)	Large/Moderate Expansion/Deepening
Case 1	A	Low velocity U = 0.1 m/s	19.1	0	38	Large expansion
	B		19.8	7	38	Large expansion and deepening
	C		19.8	7	30	Moderate expansion and large deepening
Case 2	A	High velocity U = 0.5 m/s	35	0	38	Large expansion
	B		37	7	38	Large expansion and deepening
	C		37	7	30	Moderate expansion and large deepening
Case 3	A	Low velocity U = 0.1 m/s	19.1	0	38	Large expansion
	B		19.8	7	38	Large expansion and deepening
	C		19.8	7	30	Moderate expansion and large deepening
Case 4	A	High velocity U = 0.5 m/s	35	0	38	Large expansion
	B		37	7	38	Large expansion and deepening

3.4 Results

In this section, the observed trap efficiencies for the testing program are provided and discussed. In this study, 1000 particles were injected into the flow in each single test and also in the repeats. The number of settled MPs in zone B (as shown in Figure 4) was considered the trap efficiency (TE) in each test. It is important to highlight that when calculating the TEs, only the number of particles that both reached and potentially departed from this area was considered. In other words, particles deposited before this area were excluded from the study. As shown in Table 7, each case includes different tests (A to C) in terms of the depth and width of zone B, while the velocity of

the flow and the shape of particles remained the same. In addition, each of these tests (i.e., Test A to C) was repeated three times. Thus, we named the first trial in implementing each test Trial 1. Trial 2 and Trial 3 indicated the second and third trials in each test, respectively. It should be noted that outliers (i.e., the unreasonable observations that may have occurred by laboratory errors) were excluded from the observations in each case when preparing the dataset. For instance, if the number of observed green MPs that were trapped in zone B was more than the red ones, the test was considered an outlier.

In this study, the water velocity profiles for two flow conditions (i.e., the average velocity profile of 0.1 m/s and 0.5 m/s) were measured, as shown in Figure 12, in order to provide a better picture of the boundary conditions of the implemented tests. Moreover, the Reynolds stresses profiles are depicted in Figure 13 and Figure 14 (see Appendix).

3.4.1 Settling Velocity of Spherical and Cylindrical Microplastics

There are various equations for determining the settling velocity of spherical microplastics (Cheng, 2009; Clift & Gauvin, 1971; Zhiyao et al., 2008), and there are some equations for cylindrical plastic particles (Khatmullina & Isachenko, 2017). Thus, the measured settling velocities of both spherical and cylindrical particles in this study were compared to the calculated velocities. The settling velocity was obtained using a graduated breaker with a height of 25 cm. MPs were injected into the flow from the water surface and the time that each of the spherical and cylindrical particles took to reach the breaker bottom was recorded. The settling velocity of the spherical and cylindrical particles was recorded as 0.14 and 0.18 m/s, respectively.

The settling velocity, w_s (m/s), of the spherical particles was calculated using the Equation (1) (Zhiyao et al., 2008):

$$w_s = \frac{v}{2R} d_*^3 (38.1 + 0.93 d_*^{12/7})^{-7/8} \quad (1)$$

where v is the water kinematic viscosity (m^2/s), R is the radius of the spherical particle (m), d_* is the dimensionless diameter of the particle ($d_* = 2R(g(\rho_p - \rho_w)/\rho_w v^2)^{1/3}$), g is the gravity acceleration (m/s^2), and ρ_p and ρ_w are the particle and the water density (with the same units), respectively.

In addition, some previous studies employed Equation (2) to determine the settling velocity of spherical particles (Cheng, 2009; Clift & Gauvin, 1971; Shankar et al., 2021):

$$w_s = \sqrt{\frac{4(\rho_p - \rho_w) g d_n}{3\rho_w C_d}} \quad (2)$$

where d_n is the dimensionless diameter of the volume equivalent sphere ($d_n = \sqrt[3]{6V/\pi}$) and V is the volume of the particle. C_d is the drag coefficient and can be calculated using different methods (e.g., (Cheng, 2009; Clift & Gauvin, 1971)). In this study, C_d was calculated using Equation (3) (Clift & Gauvin, 1971), which covers the turbulent regime ($10^3 \leq Re_p < 2 \times 10^5$) as well:

$$C_d = \frac{24}{Re_p} + \frac{24}{Re_p}\left(0.15 Re_p^{0.687}\right) + \frac{0.42}{1 + \frac{42{,}500}{Re_p^{1.16}}} \quad (3)$$

where Re_p is the Reynolds number of the particle ($Re_p = \frac{\rho_w w_s d_n}{\mu}$). In this study, the settling velocity was calculated as 0.11 and 0.13 $\mathrm{m/s}$ using Equations (1) and (2), respectively.

On the other hand, in this study, the settling velocity of the cylindrical particles was calculated based on the equation proposed in the previous study (Khatmullina & Isachenko, 2017), which was not close to the measured settling velocity in the lab.

3.4.2 Case 1—Spherical MP Deposition in Channel with a Low Velocity of Flow

In this case, the observations demonstrate the deposition of spherical particles in a flow with a mean streamwise velocity of 0.1 m/s, which is considered a low velocity in this study, by varying the depth and width of the channel (Figure 8). Notably, across all the tests, the trap efficiency (TE) of the red particles (i.e., particles came from the sides of the channel) consistently surpassed that of the green particles that were injected into the flow from the middle of the channel. In Figure 8a, the average values of TE, in Test A, for the green, red, and total particles are approximately 44, 70, and 57%, respectively. In Figure 8b, the observations in Test B (with large expansion and deepening) indicated that the average TE was notably (over 20%) higher than that in Test A, involving only a large expansion (Figure 8a). The average TEs for the green, red, and total particles were approximately 80, 89, and 84%, respectively. In Test C, when moderate changes were applied to the width of the channel while maintaining large deepening, the resulting TE values for the

green, red, and total particles were considerably lower than that in Test B, at approximately 59, 68, and 63%, respectively, as indicated in Figure 8c. Trial 1 was excluded in Test C because it was identified as an outlier.

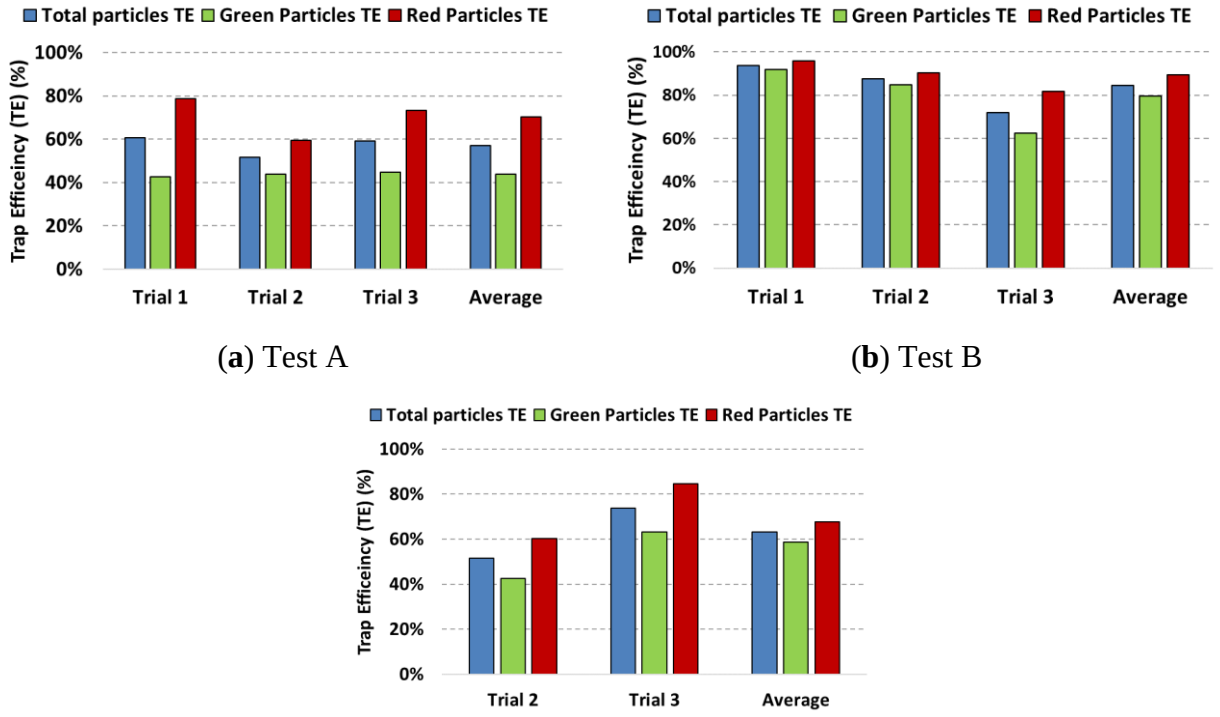

(**a**) Test A

(**b**) Test B

(**c**) Test C

Figure 8. Trap Efficiency of MPs in Case 1: Spherical MP deposition in the channel with a low velocity of flow (U = 0.1 m/s). (a) Test A (large expansion). (b) Test B (large expansion and deepening). (c) Test C (moderate expansion and large deepening). The graphs illustrate the results of two repetitions of each test along with the average trap efficiency for both green and red particles, with the total trap efficiency depicted in blue columns.

3.4.3 Case 2—Spherical MP Deposition in Channel with a High Velocity of Flow

The observations of spherical particle deposition in a flow with a mean streamwise velocity of 0.5 m/s, considered a high-velocity condition in this study, are shown in Figure 9, considering the changes in the depth and width of the channel. Significantly, in all the tests, the TE for the red particles injected from the sides of the channel consistently exceeded that of the green particles (i.e., particles came into the flow from the middle of the channel) despite the minimal difference between the observed values for the green and red particles. The average values of the TE for the

green, red, and total particles were approximately 3, 7, and 5%, respectively, as shown in Figure 9a for Test A (i.e., where only a large expansion applies to the width of the channel). The observations in Test B, where large deepening applies to the channel in addition to large expansion, indicate that there is no significant change in the TE values (Figure 9b) compared to that in Test A. The average TEs for the green, red, and total particles were approximately 7, 9, and 8%, respectively. In Figure 9b, the observations in Trial 1 and Trial 3 were excluded because they yielded outlier data. In the case of moderate changes applied only to the width of the channel while the deepening in depth was large (i.e., Test C), the TE values for the green (4%), red (12%), and total particles (8%) are depicted in Figure 9c.

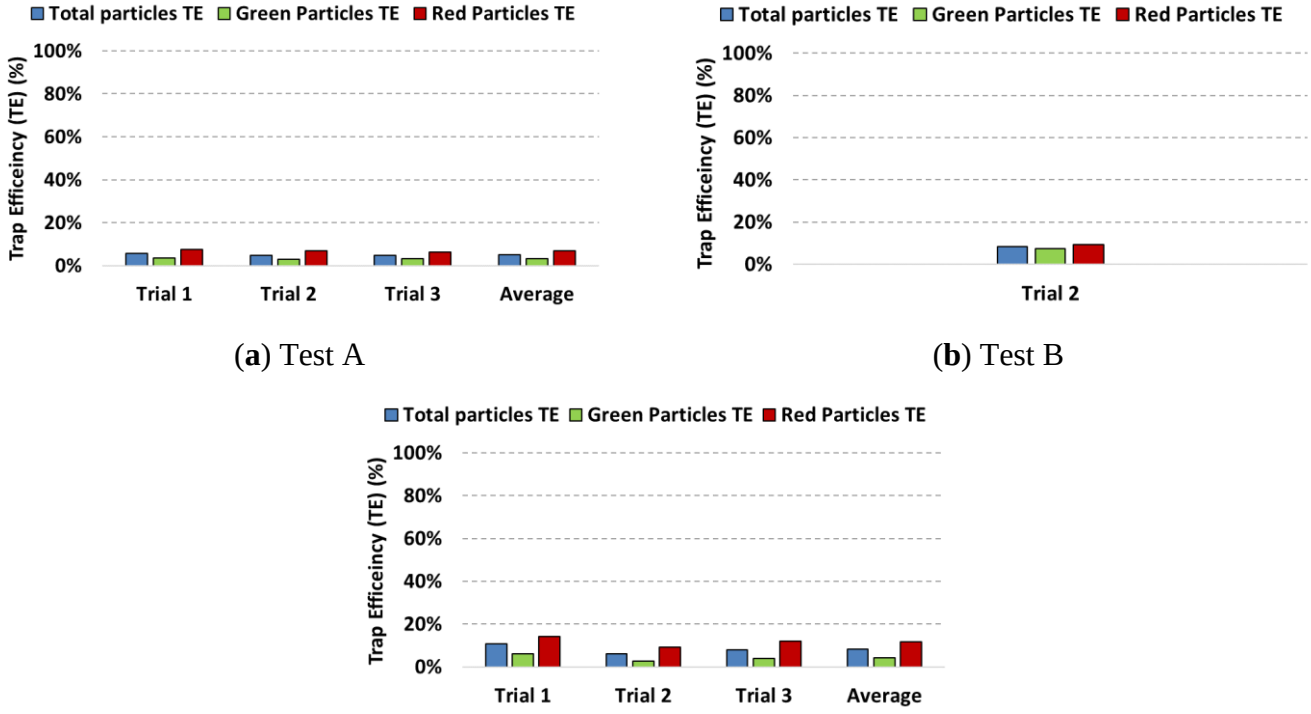

(**a**) Test A

(**b**) Test B

(**c**) Test C

Figure 9. Trap Efficiency of MPs in Case 2: Spherical MP deposition in the channel with a high velocity of flow (U = 0.5 m/s). (a) Test A (large expansion). (b) Test B (large expansion and deepening). (c) Test C (moderate expansion and large deepening). The graphs illustrate the results of two repetitions of each test along with the average trap efficiency for both green and red particles, with the total trap efficiency depicted in blue columns.

3.4.4 Case 3—Cylindrical MP Deposition in Channel with a Low Velocity of Flow

As shown in Figure 10, the laboratory observations illustrate the deposition of cylindrical particles in the different conditions of the channel (in terms of different depths and widths) where the flow with a mean streamwise velocity of 0.1 m/s may translocate particles. Among all the tests in this case, the trap efficiency (TE) for the red particles injected into the flow from the sides of the channel was higher than that for the green particles injected into the flow from the middle of the channel. In Test A, the average values of the TE for the green, red, and total particles were approximately 77, 85, and 82%, respectively (Figure 10a). The application of a large expansion and deepening on the channel (i.e., Test B) led to a significant increase in the TEs of the green and red particles. Accordingly, the average TEs for the green, red, and total particles were approximately 96, 98, and 97%, respectively. While a moderate change was applied only to the width of the channel (i.e., Test C), compared to the previous test (i.e., Test B), the resulting TE values for the green, red, and total particles were considerably smaller (i.e., 78%, 84%, and 81%, respectively), as indicated in Figure 10c. Two replicates of this test (i.e., Trials 2 and 3) were excluded from the dataset because they were identified as outliers.

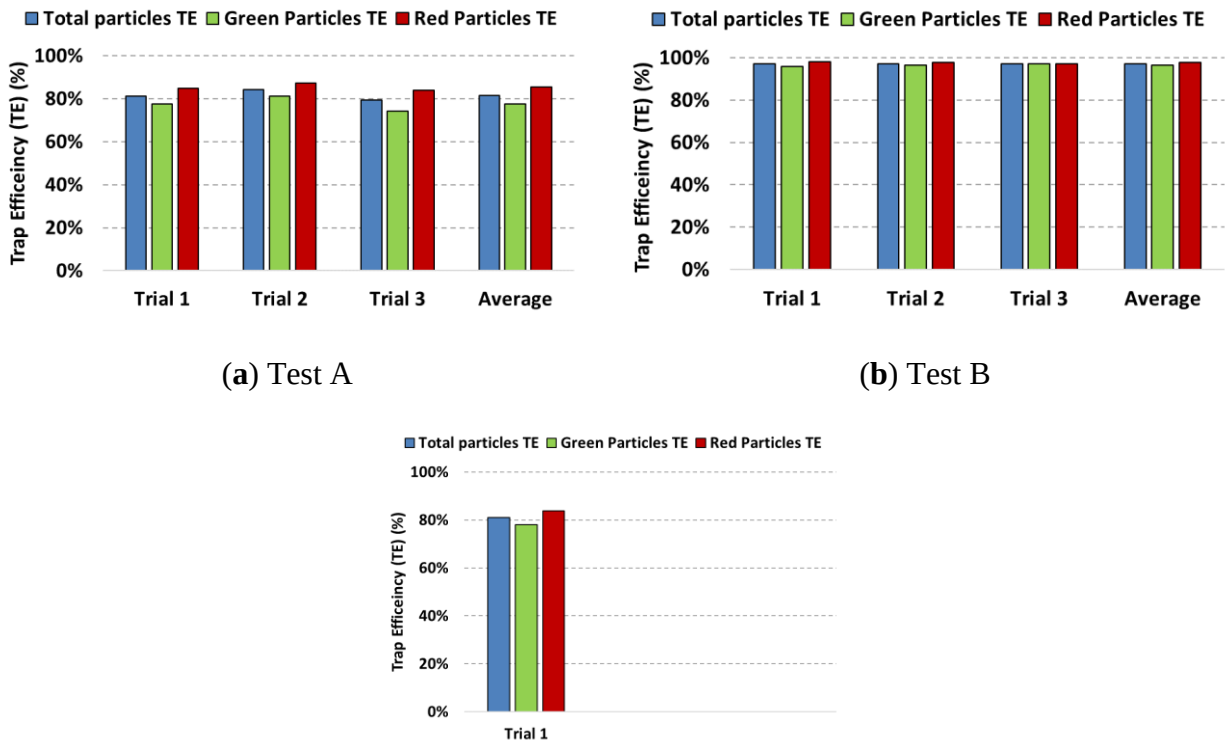

(**a**) Test A

(**b**) Test B

(**c**) Test C

Figure 10. Trap Efficiency of MPs in Case 3: Cylindrical MP deposition in the channel with a low velocity of flow (U = 0.1 m/s). (a) Test A (large expansion). (b) Test B (large expansion and deepening). (c) Test C (moderate expansion and large deepening). The graphs illustrate the results of two repetitions of tests along with the average trap efficiency for both green and red particles, with the total trap efficiency depicted in blue columns.

3.4.5 Case 4—Cylindrical MP Deposition in Channel with a High Velocity of Flow

In this case, it was observed that some cylindrical particles were deposited on the bed in a flow even with a mean streamwise velocity of 0.5 m/s, as shown in Figure 11. As stated above, the red and green particles were injected into the flow from the sides and the middle of the channel, respectively. In both tests (i.e., Test A and B) of this case, the values of the TE for the red particles were consistently higher than those of the green particles, as in the previous cases. When only a large expansion was applied to the width of the channel (i.e., Test A), the average values of the TE for the green, red, and total particles were approximately 7, 11, and 9%, respectively, as shown in Figure 11a. By applying both a large deepening and expansion to the depth and width of the channel (i.e., Test B), different TE values were observed for both the green and red particles. In

this regard, the average TEs for the green, red, and total particles were approximately 19, 29, and 21%, respectively, as shown in (Figure 11b). One of the limitations of this study is the lack of observations of cylindrical particles when they undergo moderate expansion in width and a large increase in the depth of the channel.

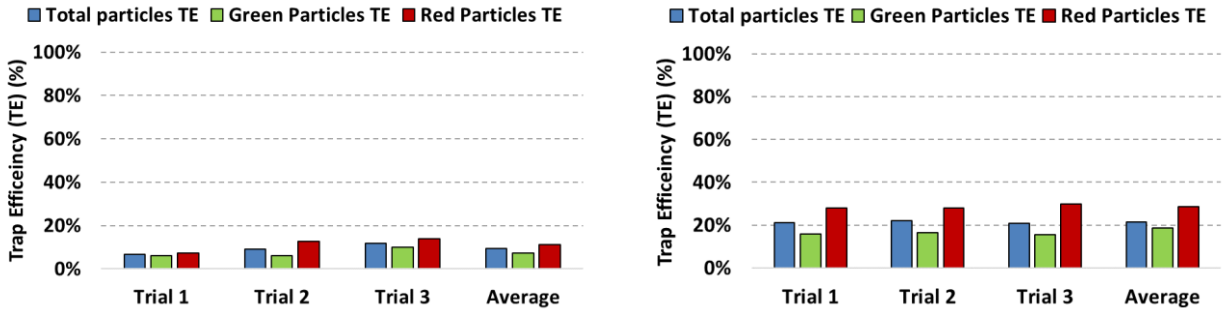

(**a**) Test A (**b**) Test B

Figure 11. Trap Efficiency of MPs in Case 4: Cylindrical MP deposition in the channel with a high velocity of flow (U = 0.5 m/s). (a) Test A (large expansion). (b) Test B (large expansion and deepening). The graphs illustrate the results of two repetitions of tests along with the average trap efficiency for both green and red particles, with the total trap efficiency depicted in blue columns.

3.5 Discussion and Conclusions

It is crucial to know how different shapes of MPs are transported and deposited in channels. Here, a simple and typical geometry was used without any complexity. Numerical models need to be fed by experimental or field data in order to yield reliable results. Experimental tests can validate numerical simulations so that they can be employed when there is no access to experimental results observed in real conditions. The results of this study shed light on the behavior of MPs when they undergo different flow velocities. On the other hand, MP transport and deposition were observed when bathymetrical changes were applied to the channel's bed. Accordingly, numerical simulations can be calibrated and validated based on experimental observations. The applications of the generated dataset are the calibration and validation of numerical models. In this regard, the initial conditions and boundary conditions in numerical models, particularly CFD models, need to be defined properly in order to simulate the real conditions. This is an essential step to determine some parameters in the numerical model, including the initial flow velocity and pressure, the flow and particle density, the size of the particles, their material, and the static and rolling friction

between the particles and the walls (or boundaries) of the channel. According to the dataset, it is possible to define the parameters for the numerical models that affect particle transport and deposition appropriately so that numerical models can be validated and employed for other cases where there is no access to experimental data.

According to the aforementioned observations, it can be seen that by increasing the velocity of the flow from 0.1 m/s to 0.5 m/s, the values of the TE for both the green and red particles become smaller among all the cases, as expected. It was observed that fewer green particles injected into the middle of the channel were trapped compared to the red particles injected into the sides of the channel because the velocity at the centerline of the channel was higher than that at the sides. Among the different tests for each case, the values of the TE for both the green and red particles were the highest when large expansion and deepening were applied simultaneously to the width and depth of the channel, respectively. By comparing the observed results between the cases implemented using spherical and cylindrical particles, it was observed that more cylindrical particles were trapped, which is compatible with previous studies (e.g., (Mason et al., 2020)). However, it should be noted that since PVC and PET have the same density of 1380 kg/m3, there is no significant difference in the settling velocity of these materials.

There are some limitations in this study that need to be investigated further in the future. For instance, this study focused on the investigation of the deposition of microplastics of the same density and size, overlooking the diverse range of microplastics observed in water bodies, which vary in terms of both density and size. In addition, there are various shapes of microplastics, including regular and irregular, found in aquatic environments, whereas spherical and cylindrical particles were solely investigated in this study. On the other hand, the effect of a slope on the bottom of the channel was not investigated. In this study, only coarse sand was considered as the sediment on the bed of the channel. Moreover, a very limited range of Froude numbers (using two flow velocities and water levels) were included in implementing the tests.

It has been suggested that more in-depth studies are needed in future to obtain a better insight into MP transport and deposition.

3.6 Appendix

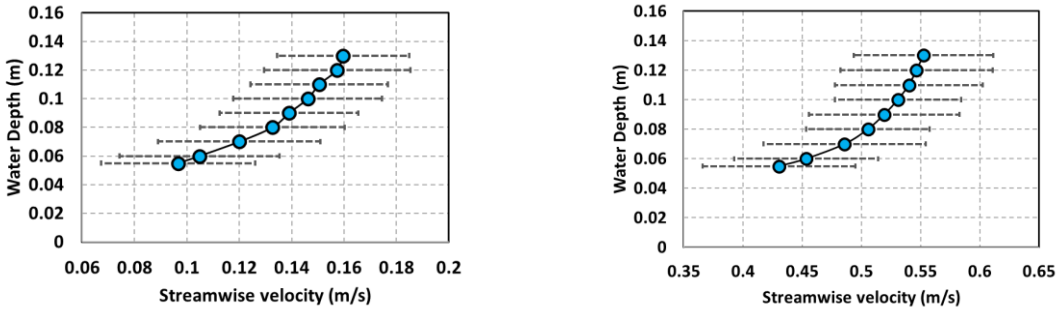

Figure 12. The streamwise water velocity profile in the channel with (a) a low velocity of flow (U = 0.1 m/s) and (b) a high velocity of flow (U = 0.5 m/s). The error bars indicate the standard deviation.

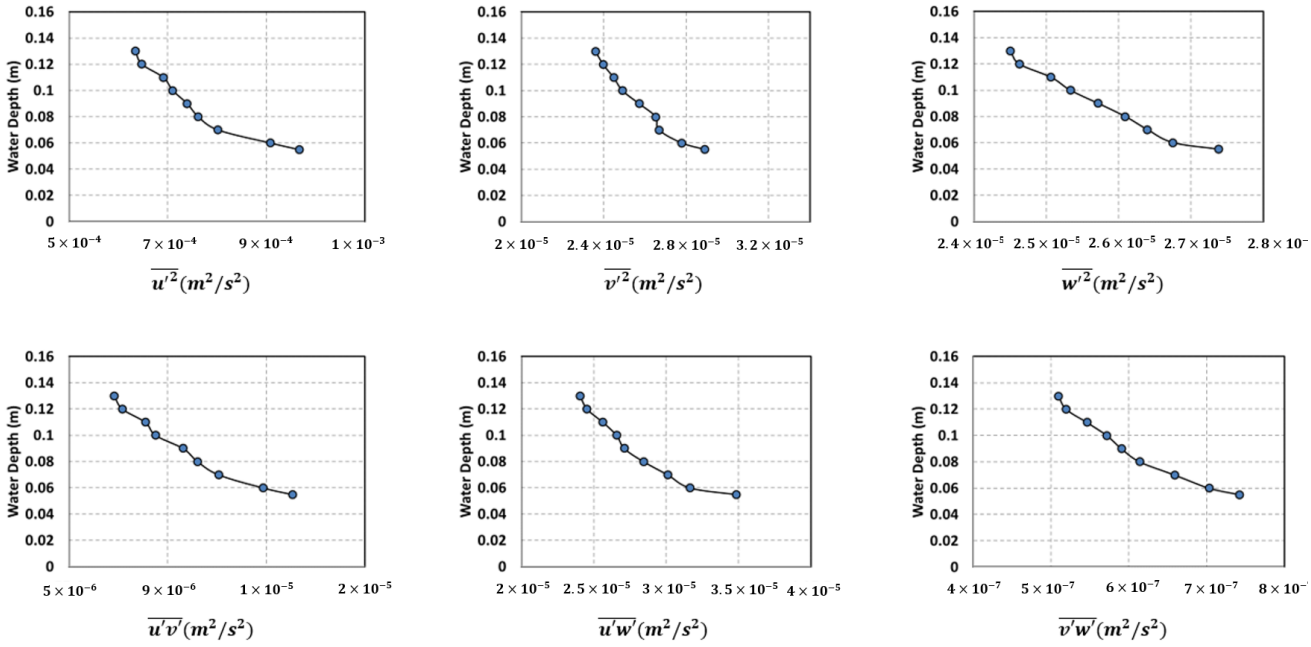

Figure 13. The profiles of Reynolds stresses in the channel with a low velocity of flow (U = 0.1 m/s).

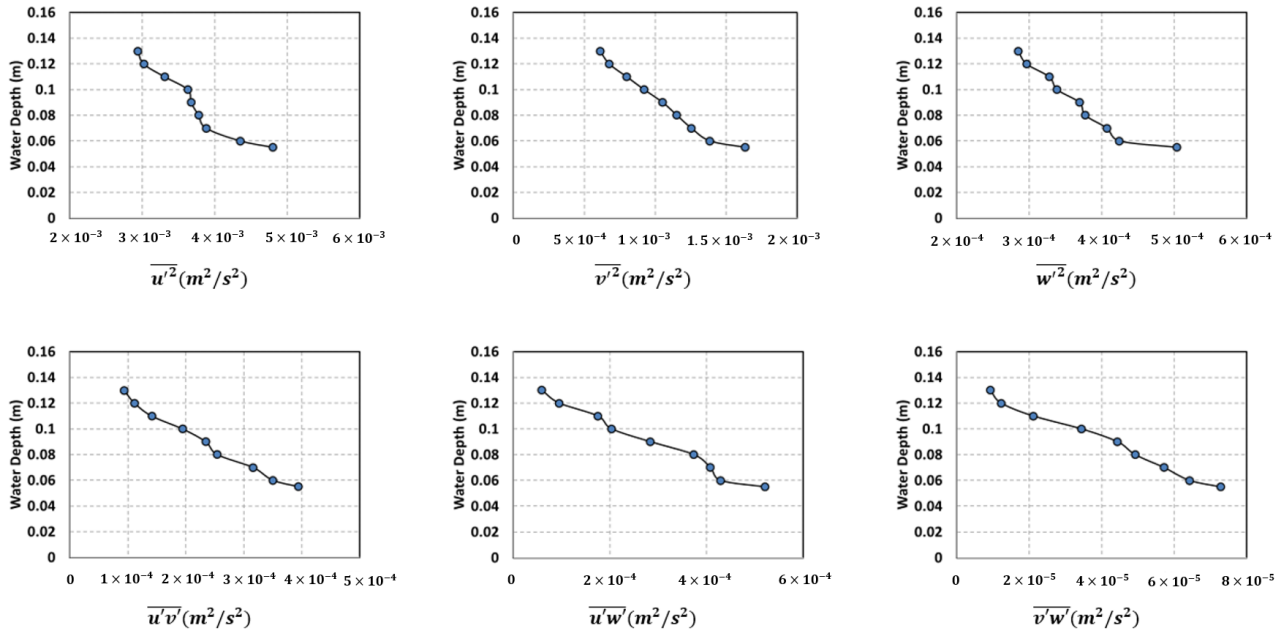

Figure 14. The profiles of Reynolds stresses in the channel with a high velocity of flow (U = 0.5 m/s).

3.7 References

Barnes, D. K., Galgani, F., Thompson, R. C., & Barlaz, M. (2009). Accumulation and fragmentation of plastic debris in global environments. Philosophical transactions of the royal society B: biological sciences, 364(1526), 1985-1998.

Bigdeli, M., Mohammadian, A., Pilechi, A., & Taheri, M. (2022). Lagrangian modeling of marine microplastics fate and transport: The state of the science. Journal of Marine Science and Engineering, 10(4), 481.

Boos, J. P., Gilfedder, B. S., & Frei, S. (2021). Tracking microplastics across the streambed interface: Using laser-induced-fluorescence to quantitatively analyze microplastic transport in an experimental flume. Water Resources Research, 57(12), e2021WR031064.

Cheng, N.-S. (2009). Comparison of formulas for drag coefficient and settling velocity of spherical particles. Powder technology, 189(3), 395-398.

Choi, C. E., Zhang, J., & Liang, Z. (2022). Towards realistic predictions of microplastic fiber transport in aquatic environments: Secondary motions. Water Research, 218, 118476.

Clift, R., & Gauvin, W. (1971). Motion of entrained particles in gas streams. The Canadian Journal of Chemical Engineering, 49(4), 439-448.

Corcoran, P. L., Belontz, S. L., Ryan, K., & Walzak, M. J. (2019). Factors controlling the distribution of microplastic particles in benthic sediment of the Thames River, Canada. Environmental science & technology, 54(2), 818-825.

De Leo, A., Cutroneo, L., Sous, D., & Stocchino, A. (2021). Settling velocity of microplastics exposed to wave action. Journal of Marine Science and Engineering, 9(2), 142.

Decuzzi, P., Lee, S., Bhushan, B., & Ferrari, M. (2005). A theoretical model for the margination of particles within blood vessels. Annals of biomedical engineering, 33, 179-190.

Doyle, M. J., Watson, W., Bowlin, N. M., & Sheavly, S. B. (2011). Plastic particles in coastal pelagic ecosystems of the Northeast Pacific ocean. Marine environmental research, 71(1), 41-52.

EU. (2019). Environmental and health risks of microplastic pollution.

Hartmann, N. I. B., Nolte, T., Sørensen, M. A., Jensen, P. R., & Baun, A. (2015). Aquatic ecotoxicity testing of nanoplastics: lessons learned from nanoecotoxicology. ASLO Aquatic Sciences Meeting,

Jalón-Rojas, I., Wang, X. H., & Fredj, E. (2019). A 3D numerical model to track marine plastic debris (TrackMPD): sensitivity of microplastic trajectories and fates to particle dynamical properties and physical processes. Marine pollution bulletin, 141, 256-272.

Kerpen, N. B., Schlurmann, T., Schendel, A., Gundlach, J., Marquard, D., & Hüpgen, M. (2020). Wave-induced distribution of microplastic in the surf zone. Frontiers in Marine Science, 7, 590565.

Khatmullina, L., & Isachenko, I. (2017). Settling velocity of microplastic particles of regular shapes. Marine pollution bulletin, 114(2), 871-880.

Koelmans, A. A., Bakir, A., Burton, G. A., & Janssen, C. R. (2016). Microplastic as a vector for chemicals in the aquatic environment: critical review and model-supported reinterpretation of empirical studies. Environmental science & technology, 50(7), 3315-3326.

Kooi, M., Nes, E. H. v., Scheffer, M., & Koelmans, A. A. (2017). Ups and downs in the ocean: effects of biofouling on vertical transport of microplastics. Environmental science & technology, 51(14), 7963-7971.

Liu, P., Zhan, X., Wu, X., Li, J., Wang, H., & Gao, S. (2020). Effect of weathering on environmental behavior of microplastics: Properties, sorption and potential risks. Chemosphere, 242, 125193.

Mason, S. A., Daily, J., Aleid, G., Ricotta, R., Smith, M., Donnelly, K., Knauff, R., Edwards, W., & Hoffman, M. J. (2020). High levels of pelagic plastic pollution within the surface waters of Lakes Erie and Ontario. Journal of Great Lakes Research, 46(2), 277-288.

Middleton, G. V. (1976). Hydraulic interpretation of sand size distributions. The Journal of Geology, 84(4), 405-426.

Miranda, M. N., Sampaio, M. J., Tavares, P. B., Silva, A. M., & Pereira, M. F. R. (2021). Aging assessment of microplastics (LDPE, PET and uPVC) under urban environment stressors. Science of the Total Environment, 796, 148914.

Napper, I. E., & Thompson, R. C. (2019). Marine plastic pollution: Other than microplastic. Waste,

Nava, V., & Leoni, B. (2021). A critical review of interactions between microplastics, microalgae and aquatic ecosystem function. Water Research, 188, 116476.

Pohl, F., Eggenhuisen, J. T., Kane, I. A., & Clare, M. A. (2020). Transport and burial of microplastics in deep-marine sediments by turbidity currents. Environmental science & technology, 54(7), 4180-4189.

Rocha-Santos, T., & Duarte, A. C. (2015). A critical overview of the analytical approaches to the occurrence, the fate and the behavior of microplastics in the environment. TrAC Trends in analytical chemistry, 65, 47-53.

Schwarzer, M., Brehm, J., Vollmer, M., Jasinski, J., Xu, C., Zainuddin, S., Fröhlich, T., Schott, M., Greiner, A., & Scheibel, T. (2022). Shape, size, and polymer dependent effects of microplastics on Daphnia magna. Journal of Hazardous Materials, 426, 128136.

Shankar, M. S., Pandey, M., & Shukla, A. K. (2021). Analysis of existing equations for calculating the settling velocity. Water, 13(14), 1987.

Thevenon, F., Carroll, C., & Sousa, J. (2014). Plastic debris in the ocean: the characterization of marine plastics and their environmental impacts, situation analysis report. Gland, Switzerland: IUCN, 52, 549-562.

Waldschläger, K., & Schüttrumpf, H. (2019). Effects of particle properties on the settling and rise velocities of microplastics in freshwater under laboratory conditions. Environmental science & technology, 53(4), 1958-1966.

Wright, S. L., & Kelly, F. J. (2017). Plastic and human health: a micro issue? Environmental science & technology, 51(12), 6634-6647.

Zhiyao, S., Tingting, W., Fumin, X., & Ruijie, L. (2008). A simple formula for predicting settling velocity of sediment particles. Water Science and Engineering, 1(1), 37-43.

4 Dynamic Prediction of Large Spherical and Cylindrical Microplastic Deposition: A Machine Learning Approach for Transport and Deposition

4.1 Abstract

The prevalence of microplastics (MPs) pollution has cast a shadow over aquatic ecosystems and their inhabitants, including humans. Each year, water bodies transport millions of tons of plastic into the ocean, with a considerable portion of this plastic settling in aquatic environments, leading to complex deposition patterns that impact aquatic ecosystems. This study aimed to develop a novel machine learning model to predict the deposition patterns of spherical and cylindrical microplastics (MPs) with identical particle diameters (d_p) and flow dynamic viscosities (v), utilizing laboratory-generated datasets. To achieve this, different generic test scenarios were conducted to collect data for various cases of the water depth in the channel (w), the flow velocity (u_f), the water depth in the channel where it undergoes deepening (h), the slope applied to the channel's bed (s), and the particle shape (including spherical and cylindrical). Eleven models including different dimensionless combinations (obtained using Buckingham theorem) of input variables (i.e., $\pi_1 = \frac{w}{d_p}$, $\pi_2 = \frac{h}{d_p}$, $\pi_3 = \frac{u_f d_p}{v}$, $\pi_4 = s$) were taken into account. Statistical evaluation metrics were used to determine the best model for predicting either spherical or cylindrical MPs. The model including all four dimensionless inputs was found to be the best model based on either spherical ($R = 0.94, MAE = 0.06, RMSE = 0.09,$ and $BIAS = 0.01$) or cylindrical data ($R = 0.90, MAE = 0.09, RMSE = 0.11,$ and $BIAS = 0.02$). The sensitivity analysis and confidence intervals revealed that the ratio of the water depth in the channel's bed deepening to the particle diameter had the most significant influence on the deposition patterns of both spherical and cylindrical MPs. These findings underscore the potential of machine learning approaches in advancing our understanding and prediction of microplastic behavior in aquatic environments, contributing to improved environmental monitoring and management strategies.

Keywords: Spherical, Cylindrical, Microplastics, Transport, Deposition, Machine Learning

4.2 Introduction

Large MPs (≤ 5 mm) can easily enter rivers, lakes, and coastal areas through direct deposition, wastewater effluent, surface runoff, infiltration, wind, etc., due to their small size and density as well as the huge uncontrolled release (Bigdeli et al., 2024; Bigdeli et al., 2022; Fazil et al., 2024;

Fiore et al., 2022; Gan et al., 2023; Xi et al., 2023). Subsequently, they are deposited or transported between various water bodies. MPs deposition and transport cause different serious challenges such as environmental pollution and outbreak diseases. For instance, urban water management systems, such as water distribution systems and wastewater treatment plants, serve as transition points for MPs, connecting natural and human water cycles (Ou et al., 2024). On the other hand, MPs can be absorbed by aquatic fauna, entering the food chain and persisting without degradation (Alvarez-Zeferino et al., 2020). Consequently, they can infiltrate the body tissues of human organs such as lymph, liver, kidney, and circulatory systems (Vethaak & Legler, 2021). Furthermore, MPs can serve as platforms for the growth of harmful biofilms (Vethaak & Legler, 2021).

Several methods have been employed to study MPs behavior in different water bodies, including laboratory modeling, machine learning (ML) modeling, numerical simulations, and field surveys (Atugoda et al., 2022; Bigdeli et al., 2024; Bigdeli et al., 2022; Boos et al., 2021; Cao et al., 2024; Eriksen et al., 2013; Fazil et al., 2024; Issac & Kandasubramanian, 2021; Jalón-Rojas et al., 2019; Mai et al., 2018; Neder et al., 2022; Shamskhany & Karimpour, 2022). Physical and predictive modeling (including ML methods), are particularly valuable for predicting the transport and fate of plastic debris, offering potential solutions to mitigate plastic pollution. Laboratory experiments are recognized as a primary method to obtain reliable results. In physical modeling, conducting simplified and generic experiments is useful for (1) observe the behavior of MPs under real-world conditions and (2) provide data for predictive models using ML approaches (Bigdeli et al., 2024). However, the main question here is whether ML is capable enough in predicting the behavior of MPs under the influence of different hydraulic flow conditions and various physical properties of MPs?

Artificial intelligence (AI) and its subset (i.e., ML) have emerged as promising tools in various scientific contexts in recent years, particularly in addressing the transport and deposition of MPs. Previous studies (Fazil et al., 2024; Qian et al., 2024) reported that ML has significant potential in addressing sediment and MPs deposition and transport, and providing proactive risk assessment. This leads to significant improvements in real-time monitoring of MPs, as well as in understanding their deposition patterns and transport trajectories, which are crucial in adopting timely actions to preserve human well-being and aquatic ecosystems.

Size, density, and shape are important physical properties that influence the fate and transport of MPs (Bigdeli et al., 2024; Bigdeli et al., 2022). In addition, the flow velocity, the water depth, and bathymetry changes exerted on the bottom of a water body including deepening and slope, are the other parameters that influence MPs deposition and transport. The complexity of their independent and combined effects makes it difficult to develop predictive models using traditional theoretical analysis and data fitting methods. However, machine learning can address these challenges by effectively handling regression tasks, inferring patterns from large datasets, and transforming them into promising models (Fazil et al., 2024; Qian et al., 2024; Xu et al., 2022). Moreover, machine learning models exploit the feature of interpretability, which can shed light on the significance and impact of parameters that play key roles in the deposition and transport of MPs.

One of the fast and promising ML methods is Extreme Learning Machine (ELM) which was proposed by Huang et al. (2006). ELM is a rapid technique that typically offers very high training speeds, significantly faster than other popular AI-based methods including adaptive neuro-fuzzy inference systems (ANFIS), support vector machines (SVM), and artificial neural networks (ANN) (Ebtehaj et al., 2023; Ebtehaj et al., 2018; Milukow et al., 2019). ELM works within the framework of a single hidden layer multi-layer perceptron, and this is why ELM is efficient and robust (Aredah et al., 2022). Furthermore, when modeling a nonlinear and complex system with ELM, the user only needs to adjust one parameter as well as the number of hidden neurons compared to other AI techniques that have multiple adjustable parameters the affect model performance (Aredah et al., 2022; Ebtehaj et al., 2023; Ebtehaj et al., 2018; Milukow et al., 2019).

The ELM consists of three layers of an input, a hidden, and an output (Ebtehaj et al., 2018). The input layer stores the input variables and makes the data available to the ELM network. The main computations of the ELM occur in the hidden layer that connects the input and output layers (Aredah et al., 2022). The information processed in the hidden layer is then passed to the output layer, which contains target parameters and where the results of ELM are compiled. In other words, the ELM algorithm starts by randomly initializing its weights between the input and hidden layers and then analytically approximates the output weights (Huang et al., 2006). It then transforms the optimization of the weight vector that is needed to be assigned between the hidden and output layers into a straightforward mathematical problem. Unlike traditional ANNs that use gradient-based optimization, the ELM method employs a least-squares training approach to develop a

single-layer feedforward network. ELM eliminates numerous complexities associated with gradient-based algorithms, such as local minima and overfitting, as well as the need for iterative adjustment of learning parameters including learning rate and epochs (Ebtehaj et al., 2018). Therefore, ELM is remarkably efficient and tends to achieve a global optimum using commonly employed activation functions. Generalization efficiency and performance are the advantages of ELM compared to traditional feedforward neural networks (FFNN) algorithms which have been proven effective on a variety of topics in different fields (Huang et al., 2006).

This study aimed to evaluate the capability of the ELM model in predicting MPs deposition patterns based on a comprehensive and reliable experimental dataset derived from controlled test scenarios. The dataset was generated through the development and construction of a scaled physical model designed to simulate realistic aquatic environments. A series of experimental test scenarios were conducted, varying key parameters such as flow conditions, particle characteristics, and channel geometries, to capture a wide range of deposition behaviors. These tests provided a robust dataset to rigorously assess the accuracy and efficiency of the ELM model in predicting MPs deposition patterns, highlighting its potential for applications in environmental monitoring and water resource management.

4.3 Materials and methods

4.3.1 Experimental setup

In this study, 57 unique test scenarios (including changes in the water depth, the flow velocity, the elevation and slope of the channel's bed) took place in a tilting flume at the National Research Council Canada Ocean, Coastal, and River Engineering Research Centre (NRC-OCRE) facility (Figure 15). The flume is 10 meters long, 40 centimeters high, and 38 centimeters wide including 1-centimeter-thick plexiglass and PVC sheets.

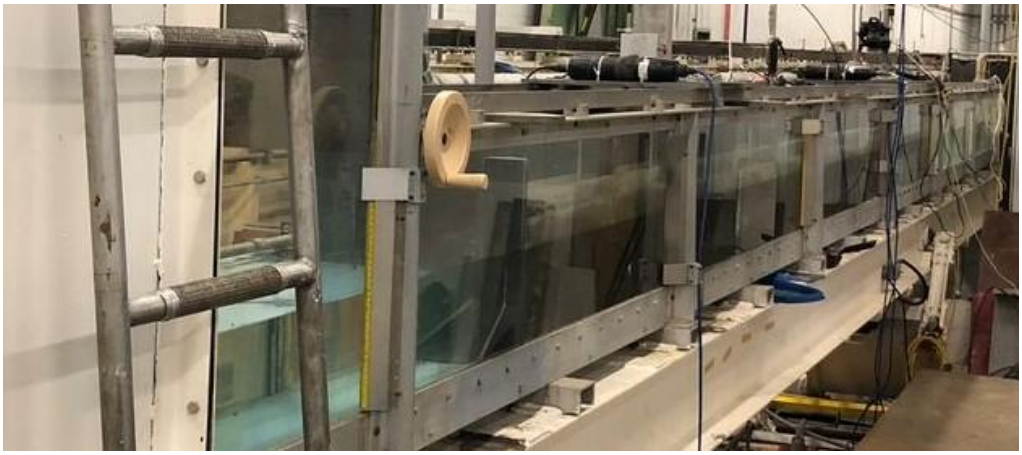

Figure 15. NRC-OCRE Tilting flume adapted from Bigdeli et al. (2024)

Figure 16 shows schematically the physical model, detailing its geometric properties and various components as well as the dimensions in each zone. Three Nortek wave probes were employed to measure the water surface elevations in the model. Wave probes were installed at various locations in the flume: the first at the very beginning of the flume (point 1 in Figure 16); the second in zone A at point 2, near the area (i.e., zone B) where the channel deepens sharply (7 cm) and moderately (3.5 cm); and the third (point 6) at the end of the flume, just before the tailing gate. A tailing gate consisting of a panel hinged at the bottom allows water to pass over it when lowered. Additionally, two mesh screens were positioned within the flume: one before the first wave probe to maintain a uniform and steady flow, and another after the tailing gate to capture particles before they enter the basin. It should be noted that each test scenario was started only after ensuring that the flow was fully developed.

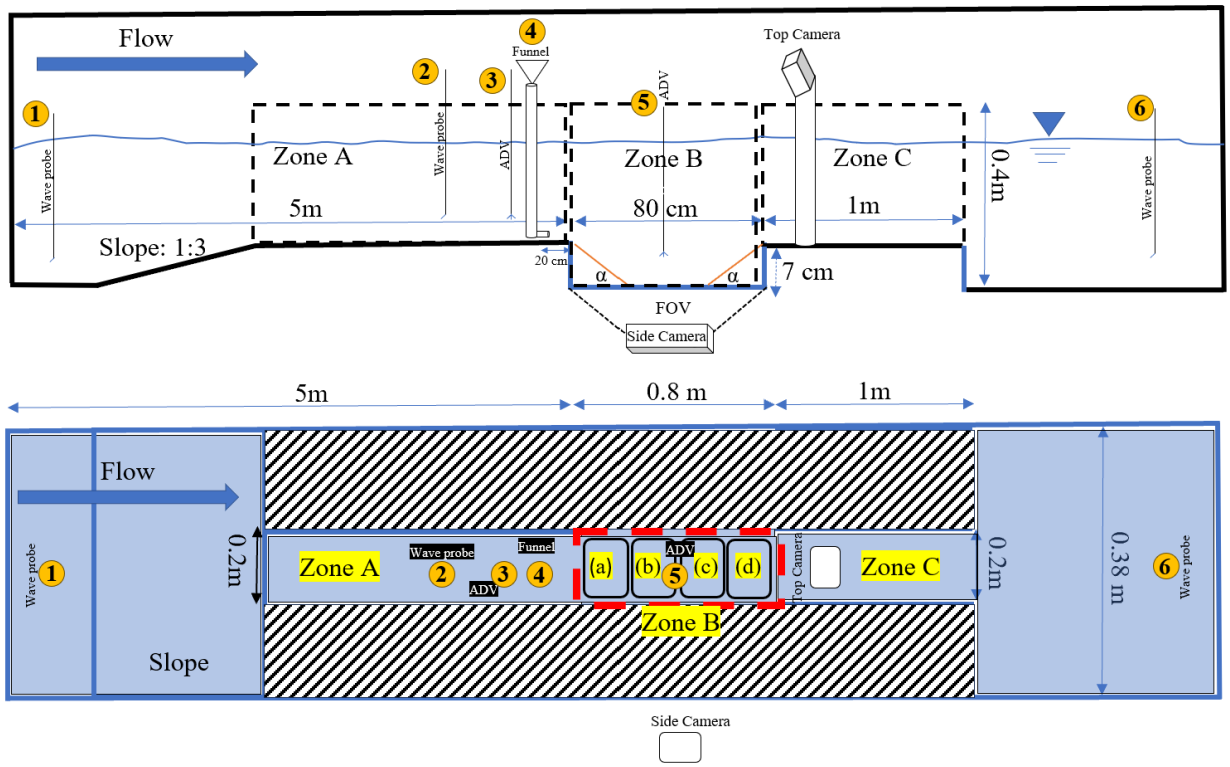

Figure 16. Schematic of the physical model setup: Top figure: Side view, Bottom figure: Top view.

As shown in Figure 16, a ramp with a slope of 1:3 was added to the initial section of the flume, just before the start of zone A. This ramp raises the channel bed, allowing a deeper area in zone B. The motion of particles within the field of view (FOV) was monitored using two high-resolution digital cameras placed on the top (in zone C) and side (in zone B) of the flume at the positions indicated in Figure 16. FOV was divided into four zones (a), (b), (c), and (d), each 20 cm in length as shown in Figure 17. Three slopes (α = 10°, 16.25°, and 22.5°) were applied to the bed of the channel within FOV. MPs were injected into the flow through funnels and injection tubes positioned just five centimeters above the flume bed in zone A (Figure 16, point 4) and 20 cm away from zone B. Therefore, they were injected into the flow from a position very near the bed, enabling the particles to be transported and deposited freely on the bed.

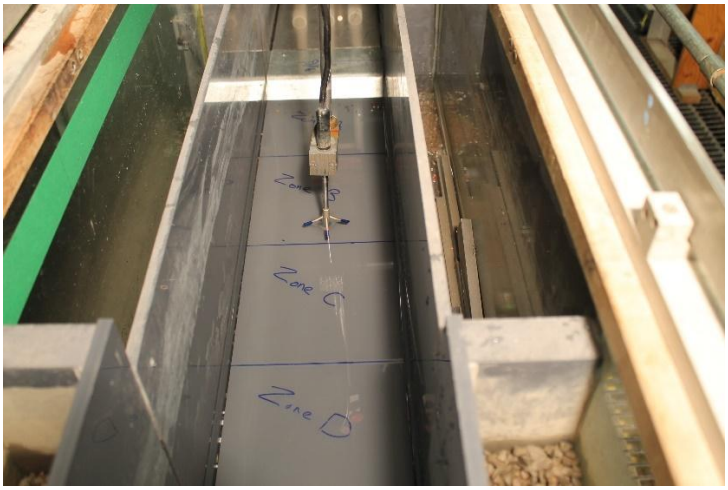

Figure 17. FOV in the physical model setup from top view

An 8-psi pressure pump was used to circulate the water flow within the flume. Water velocity profiles were evaluated both before and after the funnels and injection tubes to confirm that the flow conditions in zone A and just before zone B were unaffected by the presence of the injection tubes. In each test scenario, flow velocities were measured using two Nortek Acoustic Doppler Velocimeters (ADV). The first ADV was positioned near the funnels and injection tubes in zone A (point 3), while the other was placed at the center of FOV at point 5 (see Figure 16). The probes were installed at a depth of 0.6 times the total water depth from the surface. Velocity measurements for each test were recorded following the same procedure described by Bigdeli et al. (2024).

Each test began 100 seconds before particles release and lasted for five minutes. The test scenarios were repeated three times, and all observations were recorded to investigate MPs deposition and ensure that errors and uncertainties are minimized. It is important to note that the result for each test scenario was confirmed after the investigation of measurements obtained from three repeats and the repeat(s) which included outliers was excluded from the dataset. To measure MPs deposition within FOV, trap efficiency (TE), i.e., the ratio of deposited number MPs to total number of MPs entered FOV, was measured in each zone. The fresh water with a density of 1000 kg/m3 was used for conducting test scenarios. Two widely observed types of MPs in water bodies, polyethylene terephthalate (PET) and polyvinyl chloride (PVC), were used each having a density of 1380 kg/m^3, approximately. The shape of PET and PVC particles were considered as spherical and cylindrical, respectively (Figure 18). A total of 1000 MPs particles were injected into the flow

in each test. Both the spherical and cylindrical MPs were 3 mm in diameter. Furthermore, the average length of the cylindrical particles was 4 mm.

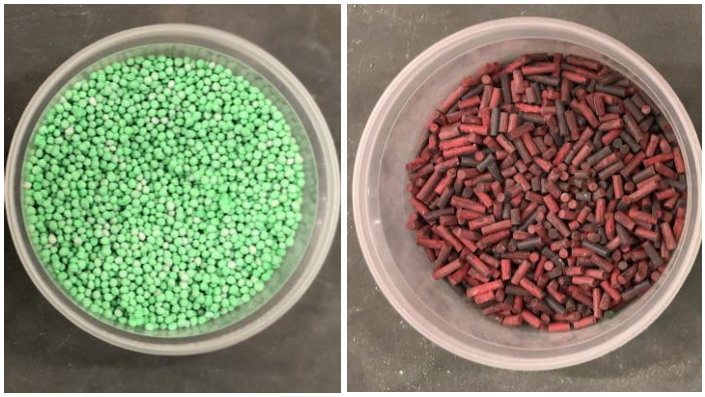

(**a**) (**b**)

Figure 18. MPs used in test scenarios. (a) Spherical (b) Cylindrical adapted from Bigdeli et al. (2024)

4.3.2 Data Acquisition

Two separate datasets were generated, one for spherical and the other for cylindrical MPs based on observations in each test scenario. Accordingly, the values of the statistical indices of the parameters used in this study are shown in Table 8. The effective hydraulic parameters on deposition of MPs have been given in this table including w (water depth in the channel), u_f (the velocity of the water flow), h (water depth in the channel where it deepens in FOV), s (the slope applied to the channel's bed in FOV), d_p (the particle diameter corresponding to 3 mm), v (dynamic viscosity of water), TE_a (trap efficiency of MPs in zone a), TE_b (trap efficiency of MPs in zone b), TE_c (trap efficiency of MPs in zone c), TE_d (trap efficiency of MPs in zone d), and TE_t (total trap efficiency of MPs in FOV).

Table 8. Statistical indices of all measured parameters in experimental test scenarios and dimensionless inputs

Parameter	Min		Max		Mean		Standard Deviation (SD)		Variance	
	Sphr.*	Cyln.**	Sphr.	Cyln.	Sphr.	Cyln.	Sphr.	Cyln.	Sphr.	Cyln.
w	0.09	0.10	0.24	0.25	0.16	0.17	0.04	0.04	0.001	0.001
u_f	0.07	0.07	0.36	0.38	0.20	0.20	0.09	0.08	0.01	0.01
h	0.09	0.10	0.31	0.31	0.21	0.21	0.04	0.04	0.002	0.002
s	0	0	22.5	22.5	13.39	12.80	7.77	7.66	60.39	58.69
w/d_p	0	0	1	1	0.49	0.46	0.25	0.24	0.06	0.06
h/d_p	0	0	1	1	0.54	0.53	0.21	0.21	0.04	0.04
$u_f.d_p/v$	0	0	1	1	0.49	0.44	0.32	0.27	0.10	0.07
TE_a	0	0	1	1	0.45	0.47	0.46	0.39	0.21	0.15
TE_b	0	0	1	1	0.14	0.15	0.30	0.21	0.09	0.05
TE_c	0	0	0.25	0.42	0.02	0.08	0.04	0.11	0.002	0.011
TE_d	0	0	0.25	0.61	0.03	0.09	0.05	0.15	0.002	0.023
TE_t	0.01	0.02	1	1	0.67	0.77	0.43	0.32	0.18	0.10

*Spherical

**Cylindrical

4.3.3 ELM Architecture

ELM, known as a novel alternative algorithm for a single-layer feedforward neural network (SLFFNN), utilizes the activation function of $f(x)$ as below using N arbitrary training samples,

included as a pair of $(x_i, y_i) \in R^n \times R^m (i = 1, 2, \dots, n)$, with L hidden nodes to predict N different samples with an error equal to zero approximately (Milukow et al., 2019):

$$\sum_{i=1}^{L} \beta_i f_i(x_j) = \sum_{i=1}^{L} \beta_i f_i(a_i \cdot b_i \cdot x) \qquad j = 1, 2, \dots, N \tag{1}$$

where $\beta_i = [\beta_{i1}, \beta_{i2}, \dots, \beta_{im}]^T$ and $a_i = [a_{i1}, a_{i2}, \dots, a_{in}]^T$ denote the matrices of output and input weights that are connected both to the hidden layer nodes. b_i represents the bias of the hidden layer nodes.

The equation 1 can be rewritten as follows (Milukow et al., 2019):

$$\sum_{i=1}^{L} \beta_i f_i(x_j) = H\beta \tag{2}$$

where H and β indicate the output matrix of the hidden layer and the output weight matrix, respectively, as shown in below (Ebtehaj et al., 2018; Milukow et al., 2019):

$$H = \begin{bmatrix} f(a_1 \cdot b_1 \cdot x_1) & \cdots & f(a_L \cdot b_L \cdot x_1) \\ \vdots & \ddots & \vdots \\ f(a_1 \cdot b_1 \cdot x_N) & \cdots & f(a_L \cdot b_L \cdot x_N) \end{bmatrix}_{N \times L} \tag{3}$$

$$\beta = \begin{bmatrix} \beta_1^T \\ \vdots \\ \beta_L^T \end{bmatrix}_{L \times m} \tag{4}$$

It should be noted that ELM can calculate the output weight with a very small error ($\varepsilon > 0$) using the pseudo-inverse of the H output.

In this model, the first step during the training phase is to determine a_i and b_i as the matrices of the input weights and the bias of the hidden layer nodes, respectively. Then hidden layer matrix is obtained by employing input variables. With the input weights and hidden layer biases established, the SLFFNN training process is converted to a least squares solution. The target function is defined subsequently as below by utilizing regularization theory in ELM models (Milukow et al., 2019):

$$min \ L_{ELM} = \frac{1}{2}\|\beta\|^2 + \frac{c}{2}\|T - H\beta\|^2 \tag{5}$$

where c is a regularization parameter which is used for increasing the generalization capability of the ELM (Salimi et al., 2024). T denotes the label matrix as below (Ebtehaj et al., 2018; Milukow et al., 2019):

$$T = \begin{bmatrix} y_1^T \\ \vdots \\ y_L^T \end{bmatrix}_{N \times m} \tag{6}$$

ELM can assign random parameters to hidden nodes if the number of discrete samples is more than the number of hidden neurons (Ebtehaj et al., 2018).

4.3.4 Methodology

4.3.4.1 Dimensional Analysis

One of the basic theorems in dimensional analysis is called the pi-theorem (Buckingham's π theorem), because it applies to groups of products of quantities. This technique allows for the development of an equation containing only products of variables, and occasionally, a single non-dimensional product, by utilizing a functional transformation. According to dimensional analysis, a natural phenomenon can be described by the following very general equation (Gibbings, 2011):

$$f(Q_1, Q_2, \dots, Q_i, \dots, Q_N) = 0 \tag{7}$$

where each of the variables, Q_j, $j = 1, 2, \dots, N$ represents either concepts, properties or units-conversion factors.

In dimensional analysis, the π -theorem provides the following transformation of equation 7 (Gibbings, 2011):

$$f(\Pi_1, \Pi_2, \dots, \Pi_i, \dots, \Pi_N) = 0 \tag{8}$$

Each of $\Pi_i$variables form a non-dimensional product of one or more variables in equation 7 where $p < N$ and this means that any of Π_1, Π_2, ... can be related to the others (e.g., $\Pi_1 = \phi(\Pi_2, \Pi_3, \dots)$). This transformation theorem is known as the π -theorem. In other words, we can show a phenomenon as a function of some dimensionless parameters, taking into account the fundamental dimensions. Accordingly, there are n independent variable with m fundamental dimensions (for instance time and length). Thus, we can conclude that the phenomenon can be a function of $n - m$ dimensionless parameters which help us to investigate its trends, variations, and sensitivity in appropriate manner. In this study, the dimensional analysis (using Buckingham theorem) was

conducted to reduce scale effects of experimental datasets on the performance of the ELM model. In this regard, seven independent variables were considered, as shown below, in order to find dimensionless parameters as well as the relationship between the hydraulic characteristics of the flow and other effective parameters on MPs transport and deposition:

$$f(v, w, u_f, h, d_p, s) = 0 \tag{9}$$

where v is the kinematic viscosity, w is water depth in the channel, u_f represents the velocity of the water flow, h is the water depth in the channel's bed deepening in FOV, d_p is the particles diameter, and s is the slope applied to the channel's bed in FOV. By using Buckingham π theorem, the dimensionless groups were defined as:

$$\begin{gathered} TE = f(\pi_1, \pi_2, \pi_3, \pi_4) \\ \pi_1 = \frac{w}{d_p},\ \pi_2 = \frac{h}{d_p},\ \pi_3 = \frac{u_f d_p}{v},\ \pi_4 = s \end{gathered} \tag{10}$$

Therefore, after generating the dataset for both spherical and cylindrical MPs, the effective variables on TE were made dimensionless and connected to it through the Eq. 10. The spherical and cylindrical datasets were split separately into two groups of training and testing data in which 70% of the data were used for training. Then the model optimization parameters were configured, and orthogonality was enabled. The number of hidden layer neurons was determined by trial and error. It should be noted that for practical applications, the model should be compact, with the number of hidden neurons (L) much lower than the number of input samples (N). If N matches L, zero error is achieved in the training dataset and often results in high error in the testing dataset which is known as overfitting (Salimi et al., 2024). The methodology of this study includes nine steps as depicted in Figure 19.

The training data were used to build the model based on 11 combinations, and the performance was evaluated using the testing dataset. In order to investigate the effect of each input variable included in Eq.10 on the performance and accuracy of the ELM in predicting TE_t, different sets of combinations were proposed. First, the ELM was modeled using the combination included in Model 1 (i.e., all four dimensionless input variables included in Eq.10). By removing one to three input variables, ten more models (Model 2 to 11) were proposed in addition to Model 1, as described in Table 9.

Table 9. The input variables included in Models 1 to 11

Model	Included input variables	Excluded input variable(s)
Model 1	$\pi_1, \pi_2, \pi_3, \pi_4$	-
Model 2	π_2, π_3, π_4	π_1
Model 3	π_1, π_3, π_4	π_2
Model 4	π_1, π_2, π_4	π_3
Model 5	π_1, π_2, π_3	π_4
Model 6	π_3, π_4	π_1 and π_2
Model 7	π_2, π_4	$\pi_1$and π_3
Model 8	π_2, π_3	π_1 and π_4
Model 9	π_1, π_4	$\pi_2$and π_3
Model 10	π_1, π_2	π_3 and π_4
Model 11	π_1, π_3	π_2 and π_4

If any of Models 2 through 11, which have one to three fewer parameters than Model 1, outperformed Model 1, the better-performing model in predicting TE_t was selected. By applying the reduction of input parameters, the increase in modeling accuracy was investigated and the best model was selected. This investigation was continued to determine which combination of input variables yielded the highest accuracy for ELM, as these had the greatest impact on modeling performance. It is important to note that the performance of ELM in prediction of TE_a, TE_b, TE_c, and TE_d was investigated in addition to TE_t as shown in Table 10 and Table 11.

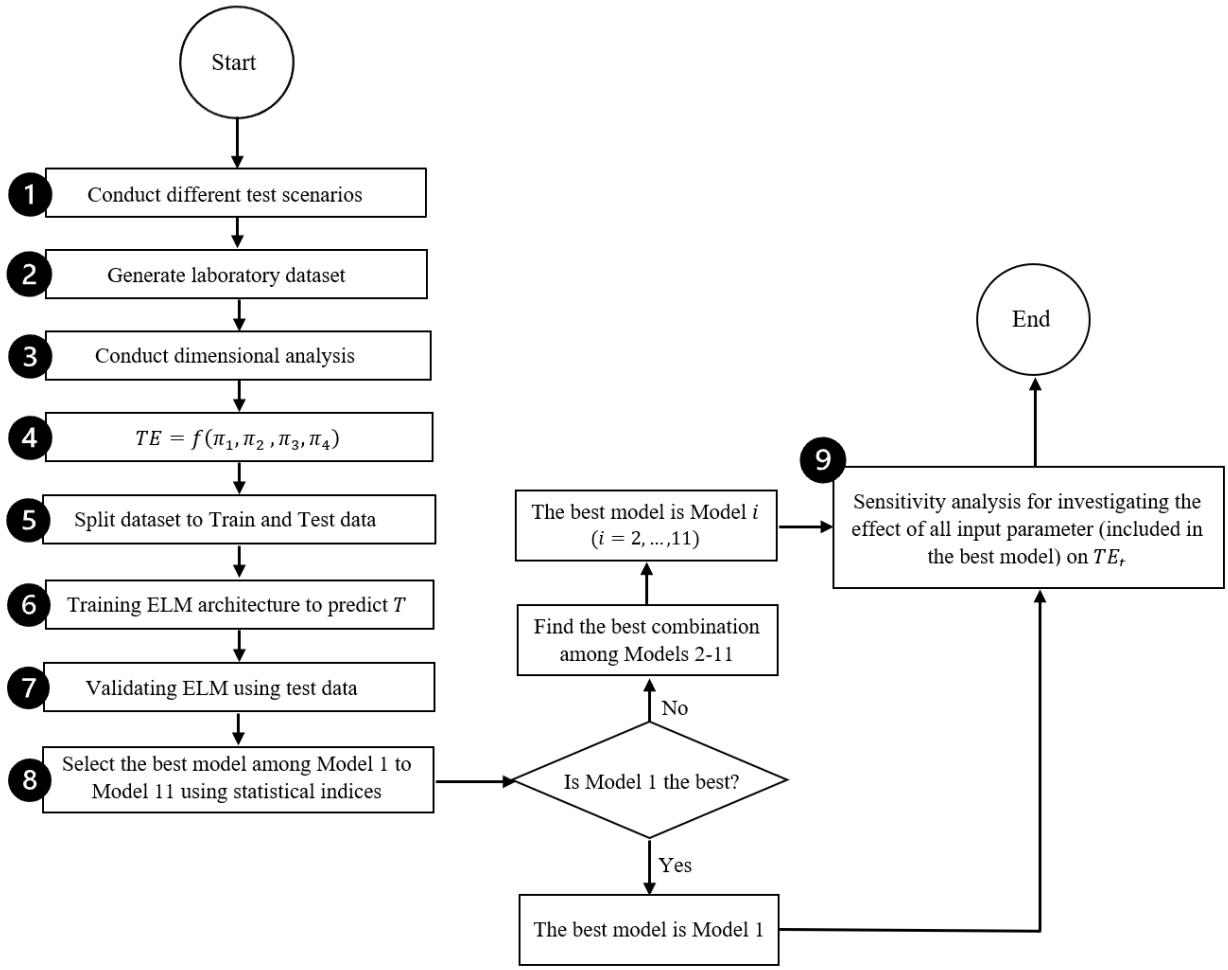

Figure 19. The methodological structure of the study.

Table 10. Statistical characteristics for different models using various combinations of spherical input variables.

Model No.	R					MAE					$RMSE$					$BIAS$				
	TE_a	TE_b	TE_c	TE_d	TE_t	TE_a	TE_b	TE_c	TE_d	TE_t	TE_a	TE_b	TE_c	TE_d	TE_t	TE_a	TE_b	TE_c	TE_d	TE_t
Model 1	0.96	0.91	0.94	0.93	0.95	0.12	0.09	0.01	0.01	0.09	0.14	0.13	0.02	0.02	0.12	0.03	0.00	0.01	0.00	0.01
Model 2	0.91	0.86	0.75	0.68	0.82	0.15	0.10	0.02	0.03	0.18	0.19	0.15	0.03	0.03	0.24	0.03	0.01	0.01	0.01	0.02
Model 3	0.79	0.90	0.83	0.69	0.81	0.20	0.10	0.02	0.03	0.21	0.28	0.14	0.03	0.03	0.27	0.00	0.01	0.00	0.00	0.04
Model 4	0.76	0.69	0.82	0.85	0.70	0.23	0.15	0.01	0.02	0.24	0.33	0.21	0.02	0.03	0.29	0.14	0.00	0.00	0.00	0.00
Model 5	0.56	0.46	0.89	0.69	0.77	0.31	0.17	0.02	0.02	0.20	0.38	0.25	0.02	0.03	0.27	0.02	0.00	0.00	0.01	0.06
Model 6	0.69	0.76	0.72	0.57	0.65	0.24	0.13	0.02	0.02	0.22	0.34	0.22	0.03	0.03	0.31	0.09	0.00	0.00	0.01	0.08
Model 7	0.77	0.80	0.73	0.55	0.41	0.23	0.17	0.01	0.03	0.33	0.31	0.27	0.02	0.04	0.40	0.07	0.10	0.00	0.01	0.10
Model 8	0.43	0.43	0.44	0.48	0.67	0.38	0.15	0.03	0.03	0.23	0.42	0.20	0.04	0.05	0.31	0.03	0.05	0.01	0.02	0.03
Model 9	0.73	0.77	0.60	0.55	0.49	0.25	0.17	0.02	0.03	0.32	0.32	0.27	0.03	0.04	0.35	0.05	0.11	0.01	0.02	0.09
Model 10	0.33	0.32	0.49	0.62	0.36	0.39	0.19	0.02	0.02	0.33	0.43	0.25	0.02	0.03	0.41	0.07	0.08	0.00	0.01	0.03
Model 11	0.40	0.46	0.46	0.47	0.77	0.35	0.18	0.03	0.03	0.21	0.41	0.25	0.04	0.03	0.30	0.04	0.04	0.01	0.01	0.08

Table 11. Statistical characteristics for different models using various combinations of cylindrical input variables.

Model No.	R					MAE					$RMSE$					$BIAS$				
	TE_a	TE_b	TE_c	TE_d	TE_t	TE_a	TE_b	TE_c	TE_d	TE_t	TE_a	TE_b	TE_c	TE_d	TE_t	TE_a	TE_b	TE_c	TE_d	TE_t
Model 1	0.94	0.92	0.91	0.83	0.91	0.11	0.10	0.04	0.07	0.11	0.12	0.13	0.05	0.10	0.14	0.01	0.04	0.01	0.02	0.03
Model 2	0.75	0.90	0.84	0.65	0.82	0.23	0.07	0.05	0.08	0.12	0.28	0.11	0.06	0.12	0.17	0.10	0.00	0.00	0.00	0.03
Model 3	0.79	0.91	0.84	0.71	0.86	0.18	0.08	0.05	0.10	0.14	0.23	0.10	0.07	0.14	0.18	0.05	0.02	0.02	0.03	0.00
Model 4	0.79	0.77	0.82	0.71	0.75	0.18	0.12	0.05	0.06	0.16	0.23	0.16	0.07	0.10	0.21	0.02	0.01	0.01	0.00	0.00
Model 5	0.47	0.49	0.47	0.62	0.82	0.31	0.10	0.08	0.09	0.12	0.37	0.16	0.10	0.13	0.19	0.01	0.01	0.02	0.00	0.00
Model 6	0.63	0.86	0.72	0.69	0.85	0.21	0.10	0.05	0.10	0.14	0.29	0.15	0.07	0.17	0.20	0.04	0.06	0.02	0.05	0.04
Model 7	0.64	0.66	0.77	0.51	0.54	0.24	0.11	0.05	0.09	0.20	0.32	0.15	0.07	0.11	0.24	0.00	0.01	0.01	0.03	0.06
Model 8	0.40	0.53	0.48	0.52	0.67	0.30	0.12	0.08	0.11	0.19	0.35	0.17	0.10	0.16	0.26	0.15	0.04	0.00	0.01	0.03
Model 9	0.73	0.68	0.83	0.58	0.56	0.23	0.11	0.04	0.08	0.24	0.28	0.16	0.06	0.10	0.29	0.04	0.04	0.02	0.04	0.06
Model 10	0.39	0.37	0.52	0.45	0.53	0.31	0.14	0.07	0.09	0.20	0.35	0.21	0.09	0.10	0.27	0.07	0.07	0.02	0.07	0.03
Model 11	0.42	0.57	0.38	0.57	0.73	0.32	0.14	0.07	0.11	0.15	0.36	0.18	0.09	0.15	0.21	0.03	0.01	0.01	0.01	0.02

4.3.5 Sensitivity analysis

As shown in step 9 in Figure 19, sensitivity analysis was employed to investigate how changes in the parameters affect the models' performance. In this study, the partial derivative sensitivity analysis (PDSA) method was used which is known as one of the commonly used techniques for analyzing the sensitivity (Azimi et al., 2017; Ebtehaj et al., 2018). In this technique, the partial derivative of the target parameter (i.e., TE_t) with respect to each input parameter (i.e., $\pi_1, \pi_2, \pi_3, \pi_4$) was calculated to assess the sensitivity of ELM to each input variable. The PDSA value determines the impact of input variables on the model's predictions. In this regard, smaller or larger PDSA values obtained with respect to each input variables imply lower or higher effect of that variable on the model's predictions for TE_t, respectively. In addition, positive or negative PDSA values for each input variable indicate that an increase or decrease in the input variable causes a corresponding increase or decrease in the target variable (TE_t), respectively.

In this study, the derivative of the obtained equation (Eq. 11) with ELM based the activation function of Sigmoid, which was in the form of a matrix function, with respect to each effective parameter was calculated using PDSA technique. This allowed for the investigation of how the considered function varies with each parameter. The matrix of partial derivatives was employed in applying PDSA.

$$f(x) = \exp\left(\left[1/\left(1+\exp\left(-\left((InW \times InV) + BHN\right)\right)\right)\right]^T \times OutW\right) \quad (11)$$

where InW denotes the $p \times q$ matrix of the input weights, InV represents the $q \times 1$ matrix of input variables (x), BHN indicates the $p \times 1$ matrix of the bias of the hidden neurons, and $OutW$ shows the $p \times 1$ matrix of the output weights. It is important to note that InV consists of $x_1, x_2, \ldots, x_q$ input variables so that each of which included k sample values so that they are formed as $k \times 1$ matrices. Moreover, p includes the number of q input variables in addition to the number of the target variable.

4.3.6 Statistical evaluation metrics

Different statistical indices were employed to assess the performance of the ELM using the predefined optimization parameters in the prediction of TE_a, TE_b, TE_c, TE_d, and TE_t by including various combinations of input variables. The statistical indices including the correlation coefficient

(R), Mean Absolute Error (MAE), Root Mean Square Error ($RMSE$), and $BIAS$, were calculated as below:

$$R = \frac{\sum_{i=1}^{n}(x_i - \bar{x})(y_i - \bar{y})}{\sqrt{\sum_{i=1}^{n}(x_i - \bar{x})^2 \sum_{i=1}^{n}(y_i - \bar{y})^2}} \quad (12)$$

$$MAE = \frac{\sum_{i=1}^{n}|y_i - x_i|}{n} = \frac{\sum_{i=1}^{n}|e_i|}{n} \quad (13)$$

$$RMSE = \sqrt{\left(\frac{1}{n}\right)\sum_{i=1}^{n}(x_i - y_i)^2} \quad (14)$$

$$BIAS = \frac{\sum_{i=1}^{n}(y_i - x_i)}{n} \quad (15)$$

where x_i and y_i are observed and predicted TE values, respectively, and $\bar{x}$ and $\bar{y}$ are the mean values of observed and predicted values of TE, respectively. $e_i = y_i - x_i$ denotes the error. n is the number of samples.

4.3.7 Uncertainty analysis

Previous research in the field of machine learning has indicated that recognizing the inherent uncertainty within machine learning algorithms is essential for improving their reliability (Habibian, 1994; Huang et al., 2022). Accordingly, in this study, the uncertainty analysis (Shaghaghi et al., 2017) was implemented using parameters such as individual prediction error (e_i), mean prediction error ($\bar{e}$), and standard deviation of prediction error (S_e) as shown below (Ebtehaj et al., 2018; LaMorte, 2021):

$$e_i = P_i - T_i \quad (16)$$

$$\bar{e} = \sum_{i=1}^{n} e_i/n \quad (17)$$

$$S_e = \sqrt{\sum_{i=1}^{n}(e_i - \bar{e})^2/n} \quad (18)$$

where P_i and T_i indicate predicted and observed values, respectively.

4.4 Results and discussion

In this section, the laboratory observations as well as the ELM performance in prediction of TE values for both spherical and cylindrical particles using different combinations of input variables were investigated. Then, the best model (i.e., combination) based on each of spherical and cylindrical datasets was introduced. Furthermore, sensitivity analysis was performed for both spherical and cylindrical data to examine the variation trend of the target variable (TE_t), based on the derivative of Eq. 11, with respect to each input variable. Finally, uncertainty analysis was performed to evaluate the performance of the proposed ELM-based model for both spherical and cylindrical particles.

4.4.1 Laboratory observations

In this study, three water depths ($w = 0.1, 0.15, \text{and } 0.2\ m$), three velocities of flow ($u_f = 0.1, 0.2, \text{and } 0.3\ m/s$), six channel's bed deepening in FOV ($h = 0.135, 0.17, 0.185, 0.220, 0.235, \text{and } 0.270\ m$), and four slopes applied to the channel's bed in FOV ($s = 0°, 10°, 16.25°, \text{and } 22.5°$) were included in conducting the experiments. As stated above, 57 out of 72 possible test scenarios excluding outlier repeats were considered in this study. As stated in Table 8, the mean values of TE values for cylindrical particles were more than spherical MPs in all zones which was consistent with the results obtained in previous studies (e.g. Bigdeli et al. (2024)). This was confirmed by the observed average ± standard deviation values of TE_t for spherical (0.67 ± 0.43) and cylindrical (0.77 ± 0.32) particles. The calculated standard deviation of the spherical data was slightly larger than that of cylindrical data indicating the wider range of TE_t values because of the shape on the results of test scenarios. The other important point that should be noted was the similarity of the measured mean values for two hydraulic parameters, i.e., w and u_f. The average values for w and u_f in spherical tests were observed to be very close to those in cylindrical experiments, indicating consistency in the test scenario implementations. In other words, the predefined values for w and u_f in spherical and cylindrical tests were set to be the same while the measured values of these two parameters were observed with a very small difference. The other two effective parameters, h and s, were predefined in each test scenario due to the geometric conditions of the channel.

Among the observed experimental test scenarios, there are several key findings regarding the behavior of both spherical and cylindrical MPs: (1) In cases with low flow velocity ($u_f = 0.1\ m/s$): Most MPs were deposited in the FOV due to the slower flow velocity near the bed, which has greater influence on the TE_t values than other hydraulic factors. (2) In high flow velocity cases ($u_f = 0.3\ m/s$): The deepening of the channel along the FOV has significant impact on increasing the deposition of MPs, especially at slopes of 16.25° and 22.5°. (3) In steeper slope cases (s = 16.25° and 22.5°): TE_t values were increased, as the particles velocity was reduced due to the continuity equation, independent of factors such as u_f and h.

4.4.2 Hyperparameters Tuning

Hyperparameter tuning is crucial for optimizing the performance of machine learning models. The optimized parameters for ELM training are presented in Table 12. It is important to highlight that identical parameter values were employed for both spherical and cylindrical datasets to ensure consistency in the modeling process.

For the ELM, separate training sessions were conducted with the spherical and cylindrical datasets. For both datasets, a total of 64 samples for training and 27 samples for testing were allocated. This distribution was achieved using a random selection method, designating 70% of the data for training and the remaining 30% for testing.

During the hyperparameter tuning, it was observed that setting the number of hidden neurons to 25 and the number of iterations to 25,000 provided the optimal performance for the ELM. These settings were determined after extensive experimentation and evaluation of the model's performance metrics. Table 12 lists the key hyperparameters that were fine-tuned to achieve the best results. The sigmoid function with 4 input neurons and 5 output neurons was used as the activation function, which followed the ELM learning rule.

Table 12. User-specified parameters for the ELM model

Parameter	Value
Hidden Neuron	25
Activation Function(s)	Sigmoid Function

Parameter	Value
Neurons - Input	4
Neurons - Output	5
Learning rule	ELM
Number of iterations	25,000

4.4.3 Selecting the best Model

As mentioned earlier, 30% of the data (27 samples) was used to test the performance of the model. The prediction results obtained based on those samples of spherical and cylindrical MPs deposition in different zones of FOV using Model 1 are depicted in Figure 20 and Figure 21, respectively. Model 1 contained all four effective and dimensionless parameters included in Eq. 10 and estimated TEs for both spherical and cylindrical MPs. As shown in Figure 20, TE_a, TE_b, TE_c, TE_d, and TE_t were estimated almost close to the observed values, $R = 0.96, 0.91, 0.94, 0.93$ and 0.95, respectively, in spherical tests. The Model 1 also performed well in prediction of TE_a, TE_b, TE_c, TE_d, and TE_t by $R = 0.94, 0.92, 0.91, 0.83$ and 0.91, respectively, in cylindrical tests (Figure 21). This similarity provided the first evidence of the accuracy and validity of predictive model. Additionally, MPs deposition patterns were very similar between the physical model and the corresponding ELM model. These observations demonstrated that the ELM model was promising for predicting MPs deposition. The relatively small errors were obtained for predicting TE_a, TE_b, TE_c, TE_d, and TE_t in spherical tests with $MAE = 0.12, 0.09, 0.01, 0.01$, and 0.09, and $RMSE$ of $0.14, 0.13, 0.02, 0.02$, and 0.12, respectively. This was followed by the obtained results for TE_a, TE_b, TE_c, TE_d, and TE_t in cylindrical tests with $MAE = 0.11, 0.10, 0.04, 0.07$, and 0.11, and $RMSE$ of $0.12, 0.23, 0.05, 0.010$, and 0.14, respectively. $BIAS$ was obtained to be very small and positive in the results for both spherical and cylindrical tests. This indicated that ELM had a slight overestimation in predicting all TEs, resulting in insignificant impact to the prediction results. In spherical tests, the $BIAS$ values were found to be $0.03, 0.004, 0.01, 0.001$, and 0.01 for TE_a, TE_b, TE_c, TE_d, and TE_t, respectively. $BIAS$ values of predictions for cylindrical particles for the

quantities TE_a, TE_b, TE_c, TE_d, and TE_t were found to be $0.01, 0.04, 0.01, 0.02$, and 0.03, respectively.

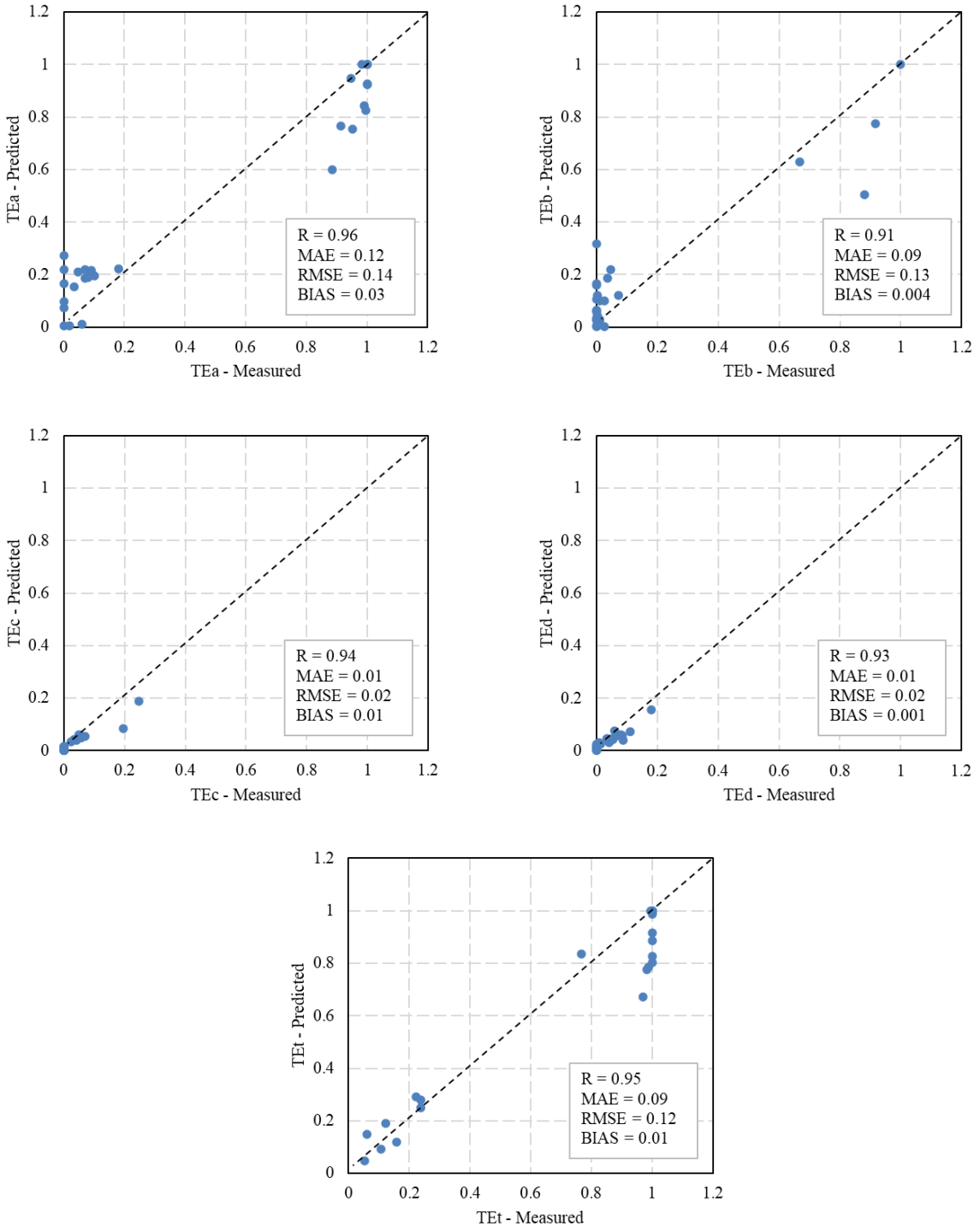

Figure 20. The prediction of spherical MPs deposition in different zones of FOV using ELM, Model 1.

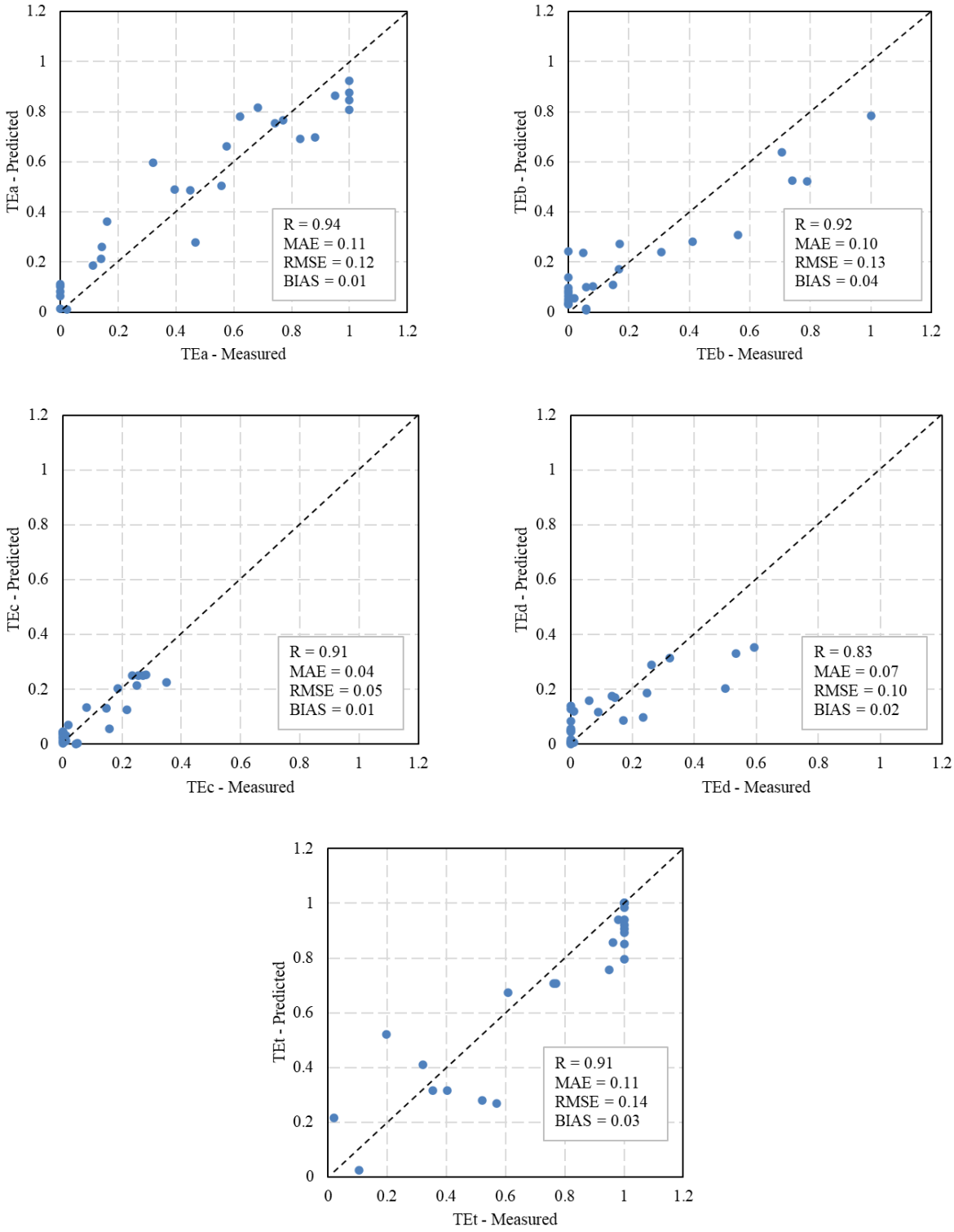

Figure 21. The prediction of cylindrical MPs deposition in different zones of FOV using ELM, Model 1.

2128

The analysis of the ELM performance was further continued by investigating the outcomes obtained from the other Models including different input combinations to determine the best Model. In other words, ELM training was continued with different combinations to find the best performance in terms of $R, MAE, MSE,$ and $BIAS$. For this purpose, the average value of the statistical indices including all TEs values was calculated for all models, as shown in Table 13, to facilitate the comparison. In this regard, as mentioned before, 10 additional models (Model 2 to 11) were analyzed alongside Model 1 by excluding one to two input variables. Among Models 2 to 11, Model 10 had the poorest performance based on spherical ($R = 0.42, MAE = 0.19, RMSE = 0.23,$ and $BIAS = 0.04$) and cylindrical ($R = 0.45, MAE = 0.16, RMSE = 0.20,$ and $BIAS = 0.06$) data. In Model 10, $\pi_3 = \frac{u_f d_p}{v}$ and $\pi_4 = s$ were excluded from the input variables. This indicated that π_3 and π_4 were more important compared to the other parameters included in Eq. 10, when predicting TEs values. On the other hand, Model 8 and 11 showed weak performance. This indicated that excluding π_4 had the most significant impact on the ELM's performance, as confirmed by both spherical and cylindrical results.

According to Table 13, Model 1 performed the best based on both spherical ($R = 0.94, MAE = 0.06, RMSE = 0.09,$ and $BIAS = 0.01$) and cylindrical ($R = 0.90, MAE = 0.09, RMSE = 0.11,$ and $BIAS = 0.02$) datasets, as stated before. This indicated an inevitable influence of each dimensionless parameter on TE values.

In general, the best ELM model using spherical data exhibited slightly higher accuracy in predicting TEs values than the best model using cylindrical data, although Model 1 showed the performance in both datasets. It is important to note that ELM model's results are consistent with the fundamental behaviors and properties of MPs observed under real conditions (simulated by conducting experimental tests).

Table 13. The average values of statistical indices of all TEs obtained for Models 1 to 11

Model	R		MAE		RMSE		BIAS		Best Model	
	Sphr.*	Cyln.**	Sphr.	Cyln.	Sphr.	Cyln.	Sphr.	Cyln.	Sphr.	Cyln.
Model 1	0.94	0.90	0.06	0.09	0.09	0.11	0.01	0.02	☑	☑
Model 2	0.81	0.79	0.10	0.11	0.13	0.15	0.01	0.03	☒	☒
Model 3	0.80	0.82	0.11	0.11	0.15	0.14	0.01	0.02	☒	☒
Model 4	0.76	0.77	0.13	0.11	0.18	0.16	0.03	0.01	☒	☒
Model 5	0.67	0.57	0.15	0.14	0.19	0.19	0.02	0.01	☒	☒
Model 6	0.68	0.75	0.13	0.12	0.19	0.17	0.04	0.04	☒	☒
Model 7	0.65	0.62	0.15	0.14	0.21	0.18	0.06	0.02	☒	☒
Model 8	0.49	0.52	0.16	0.16	0.21	0.21	0.03	0.05	☒	☒
Model 9	0.63	0.68	0.16	0.14	0.20	0.18	0.05	0.04	☒	☒
Model 10	0.42	0.45	0.19	0.16	0.23	0.20	0.04	0.06	☒	☒
Model 11	0.51	0.53	0.16	0.16	0.21	0.20	0.03	0.02	☒	☒

*Spherical

**Cylindrical

4.4.4 Sensitivity analysis

In this study, sensitivity analysis was performed for each input variable included in the best model derived from the optimal ELM model. The best model based on either spherical or cylindrical data was Model 1. According to the PDSA technique, the matrices derived from the optimal ELM model were substituted into Eq.11, and subsequently, the partial derivative of TE_t with respect to each input variable included in the best model was calculated. The PDSA results of the ELM-based equation for all input variables which were included in the best model were depicted in Figure 22 and Figure 23, based on spherical and cylindrical data. It was observed that the partial derivative (PD) obtained based on both spherical and cylindrical data in negative and positive values resulted in a decrease and an increase in the target variable (TE_t), respectively.

Among the input variables included in Model 1 (i.e., $\pi_1, \pi_2, \pi_3, \pi_4$), the values indicate the sensitivity of TE_t, measured for spherical MPs, to π_2 were calculated as the highest (see Figure

22). It is important to note that π_4 also had significant effect on the estimation of TE_t. The PD values for π_2 varied from −15 to +12. It was observed that π_1 and π_3 had almost the same effect on the prediction of TE_t .

The PD values for four dimensionless input variables included in Model 1 and obtained based on cylindrical data were shown in Figure 23. Similar to the results of sensitivity analysis based on spherical data, π_2 had the highest PD values (when $\pi_2 = 0.7$) and the largest effect on the predicted TE_t, although the variation is limited to a larger range (-12 to 20). Contrary to what was obtained based on spherical data, π_1 also had an undeniable influence on predicting TE_t. In addition, π_3 and π_4 had almost the same impact on the prediction of TE_t. The methodology employed here demonstrates how a sensitivity analysis can be used to understand the relative influence of different parameters affecting MPs deposition in various applications.

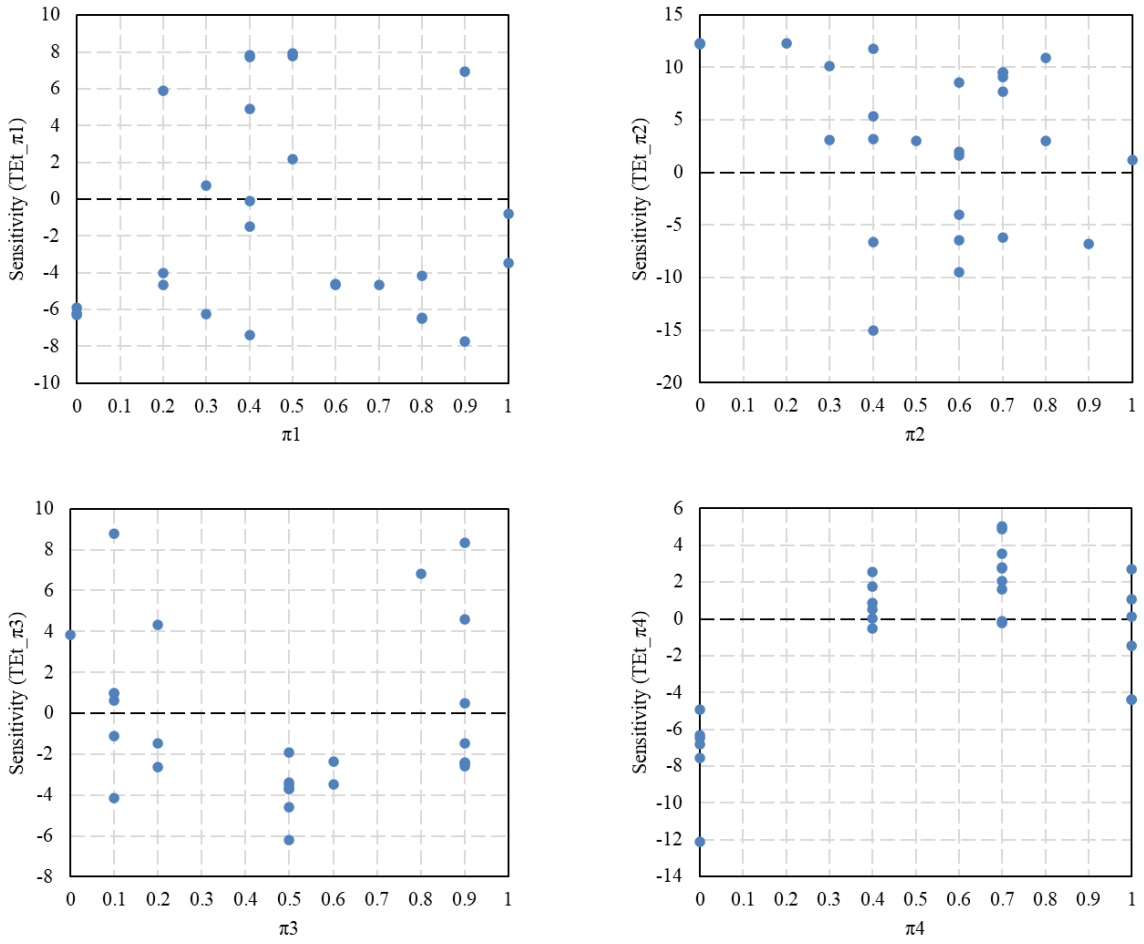

Figure 22. Sensitivity analysis results obtained from Model 1 based on spherical data.

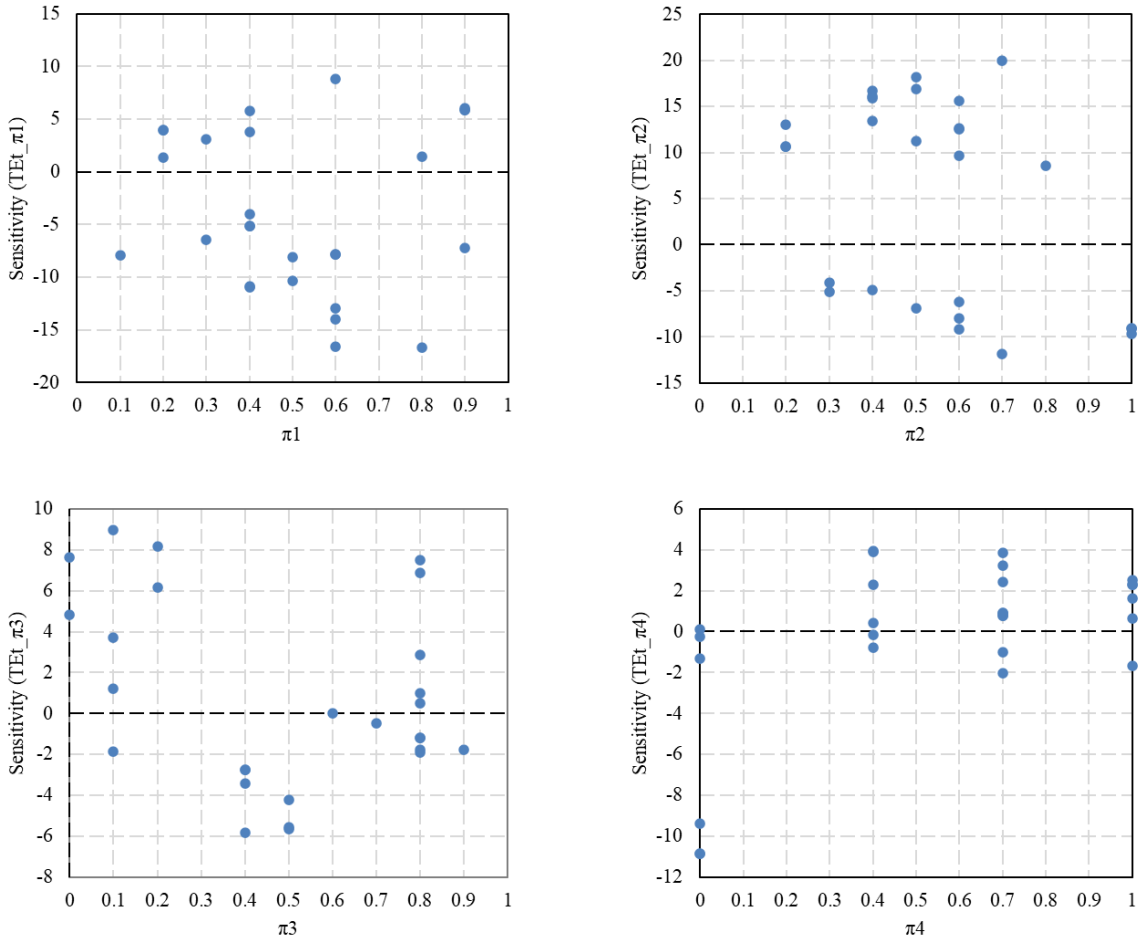

Figure 23. Sensitivity analysis results obtained from Model 1 based on cylindrical data.

4.4.5 Uncertainty analysis

In the present study, the uncertainties in predicting TE_t values, as the target variable, were provided by evaluating the ELM model quantitatively. In this regard, the positive or negative $\bar{e}$ value shows whether the prediction model is overestimating or underestimating the target variable (TE_t).

The confidence band was defined by $\bar{e}$ and S_e values and using the Wilson score method without continuity correction and a confidence level of 95%. It should be noted that since the sample size was under 30, we had to switch to using a t-value instead of a Z-score to accommodate the smaller sample size and dependence on sample standard deviation (LaMorte, 2021). Thus, a confidence band of almost 95% was obtained for both spherical and cylindrical data using $\pm 1.706 S_e$ values. Accordingly, the width of uncertainty band (WUB) was calculated, which indicates the gap

between the upper and lower uncertainty bands. The results of the uncertainty analysis, including $\bar{e}$, S_e, WUB, and 95% prediction interval error (PEI) were summarized in Table 14. The observed narrow uncertainty bands (±0.139 and ±0.155) and small 95% prediction error intervals, (0, 0.20) and (0, 0.25), for spherical and cylindrical data, respectively, indicate the reliability of the ELM model for the present application.

Table 14. Results of the uncertainty analysis for ELM in testing phase

Method	**Number of Test Samples**	**Dataset Source**	**Mean Error ($\bar{e}$)**	**Standard Deviation of Absolute Error (S_e)**	**Width of uncertainty band (WUB)**	**95% prediction error interval (PEI)**
ELM	27	Spherical	0.063	0.081	±0.139	(0, 0.20)
		Cylindrical	0.096	0.091	±0.155	(0, 0.25)

4.5 Conclusion

This study aimed to evaluate the capability of machine learning methods in predicting of MPs deposition, at the same particle diameter (d_p) and dynamic viscosity of water (v) in a generic experimental setup and included a comparative analysis of different potential input combinations.

ELM was used as a subset of AI to evaluate the feasibility of predicting the deposition of spherical and cylindrical MPs under different test scenarios (i.e., various water depths (w), velocities of the water flow (u_f), water depths in the channel where it undergoes a deepening in the FOV (h), and slopes applied to the channel's bed in FOV (s)) conducted experimentally in the laboratory. Four dimensionless input variables including $\pi_1 = \frac{w}{d_p}$, $\pi_2 = \frac{h}{d_p}$, $\pi_3 = \frac{u_f d_p}{v}$, and $\pi_4 = s$ were found to be the most effective parameters as a result of dimensional analysis on the deposition of MPs. The trap efficiencies (TEs) of MPs, parameters for showing their deposition, were measured in the lab for four zones including TE_a (trap efficiency of MPs in zone a), TE_b (trap efficiency of MPs in zone b), TE_c (trap efficiency of MPs in zone c), TE_d (trap efficiency of MPs in zone d), and TE_t (total trap efficiency of MPs in FOV). The ELM model was trained based on spherical and

cylindrical datasets including TEs values and different combinations of input variables. Accordingly, 11 different models were introduced including various combinations of dimensionless inputs. The best model for spherical and cylindrical data showed high accuracy in predicting MPs deposition in different zones of FOV.

Model 1 performed best based on both spherical ($R = 0.94$ and $RMSE = 0.09$) and cylindrical ($R = 0.90$ and $RMSE = 0.11$) datasets. This is the first study to conduct an in-depth sensitivity analysis, using a proposed equation, on the trained ELM model for each input variable. In this regard, the partial derivative sensitivity analysis (PDSA) technique was employed for the first time for analyzing the sensitivity of the target variable (TE_t) to each input variable included in the best model using the ELM-based equation. Conclusively, the best model selected based on spherical and cylindrical data (i.e., Model 1) confirmed that π_2 had the largest effect on the predicted TE_t. In addition, π_1 and π_4 also had a noticeable impact on the prediction of TE_t, which were estimated based on cylindrical and spherical data, respectively. Moreover, π_3 had the most limited range of PD values, which had the least impact on the prediction of TE_t compared to the other dimensionless parameters in both spherical and cylindrical datasets. It is worth noting that the differences in the obtained ranges of PD values for the dimensionless inputs were not very significant, highlighting the influence of each input on the prediction of TE_t.

Uncertainty analysis was also used to quantitatively assess the ELM model. Narrow uncertainty bands (±0.139 and ±0.155 for spherical and cylindrical data, respectively) and small 95% prediction error interval, (0, 0.20) and (0, 0.25) based on spherical and cylindrical data, respectively, were obtained for the ELM model.

This study demonstrates the promising capability of ELM in predicting MPs deposition observed under different experimental scenarios in the presence of sufficient data and lays the foundation for further applications of the ELM method in MPs deposition predictions.

4.6 References

Alvarez-Zeferino, J. C., Ojeda-Benítez, S., Cruz-Salas, A. A., Martínez-Salvador, C., & Vázquez-Morillas, A. (2020). Microplastics in Mexican beaches. *Resources, Conservation and Recycling*, *155*, 104633.

Aredah, A. S., Ertugrul, O. F., Sattar, A. A., Bonakdari, H., & Gharabaghi, B. (2022). Extreme Learning Machine model for assessment of stream health using the Qualitative Habitat Evaluation Index. *Water Supply*, *22*(5), 5355-5375.

Atugoda, T., Piyumali, H., Liyanage, S., Mahatantila, K., & Vithanage, M. (2022). Fate and behavior of microplastics in freshwater systems. In *Handbook of Microplastics in the Environment* (pp. 781-811). Springer.

Azimi, H., Bonakdari, H., & Ebtehaj, I. (2017). A highly efficient gene expression programming model for predicting the discharge coefficient in a side weir along a trapezoidal canal. *Irrigation and drainage*, *66*(4), 655-666.

Bigdeli, M., Mohammadian, A., & Pilechi, A. (2024). A Laboratory Dataset on Transport and Deposition of Spherical and Cylindrical Large Microplastics for Validation of Numerical Models. *Journal of Marine Science and Engineering*, *12*(6), 953.

Bigdeli, M., Mohammadian, A., Pilechi, A., & Taheri, M. (2022). Lagrangian modeling of marine microplastics fate and transport: The state of the science. *Journal of Marine Science and Engineering*, *10*(4), 481.

Boos, J. P., Gilfedder, B. S., & Frei, S. (2021). Tracking microplastics across the streambed interface: Using laser-induced-fluorescence to quantitatively analyze microplastic transport in an experimental flume. *Water Resources Research*, *57*(12), e2021WR031064.

Cao, T., Tian, D., Zhou, F., & Bao, M. (2024). Numerical investigation of the transport and accumulation of conservative pollutants off Changjiang Estuary. *Journal of Marine Systems*, *241*, 103895.

Ebtehaj, I., Bonakdari, H., Gharabaghi, B., & Khelifi, M. (2023). Short-Term Precipitation Forecasting Based on the Improved Extreme Learning Machine Technique. *Environmental Sciences Proceedings*, *25*(1), 50.

Ebtehaj, I., Bonakdari, H., Moradi, F., Gharabaghi, B., & Khozani, Z. S. (2018). An integrated framework of extreme learning machines for predicting scour at pile groups in clear water condition. *Coastal engineering*, *135*, 1-15.

Eriksen, M., Mason, S., Wilson, S., Box, C., Zellers, A., Edwards, W., Farley, H., & Amato, S. (2013). Microplastic pollution in the surface waters of the Laurentian Great Lakes. *Marine pollution bulletin*, *77*(1-2), 177-182.

Fazil, A. Z., Gomes, P. A., & Sandamal, R. K. (2024). Applicability of Machine Learning Techniques to Analyze Microplastic Transportation in Open Channels with Different Hydro-environmental Factors. *Environmental pollution*, 124389.

Fiore, M., Fraterrigo Garofalo, S., Migliavacca, A., Mansutti, A., Fino, D., & Tommasi, T. (2022). Tackling marine microplastics pollution: an overview of existing solutions. *Water, Air, & Soil Pollution*, *233*(7), 276.

Gan, Q., Cui, J., & Jin, B. (2023). Environmental microplastics: Classification, sources, fates, and effects on plants. *Chemosphere*, *313*, 137559.

Gibbings, J. C. (2011). *Dimensional analysis*. Springer Science & Business Media.

Habibian, A. (1994). Effect of temperature changes on water-main breaks. *Journal of transportation engineering*, *120*(2), 312-321.

Huang, G.-B., Zhu, Q.-Y., & Siew, C.-K. (2006). Extreme learning machine: theory and applications. *Neurocomputing*, *70*(1-3), 489-501.

Huang, X., Rudolph, D. L., & Glass, B. (2022). A coupled thermal-hydraulic-mechanical approach to modeling the impact of roadbed frost loading on water main failure. *Water Resources Research*, *58*(3), e2021WR030933.

Issac, M. N., & Kandasubramanian, B. (2021). Effect of microplastics in water and aquatic systems. *Environmental Science and Pollution Research*, *28*, 19544-19562.

Jalón-Rojas, I., Wang, X. H., & Fredj, E. (2019). A 3D numerical model to track marine plastic debris (TrackMPD): sensitivity of microplastic trajectories and fates to particle dynamical properties and physical processes. *Marine pollution bulletin*, *141*, 256-272.

LaMorte, W. (2021). Confidence intervals for sample size less than 30, PH717 Module 6–Random error, probability, estimation, and confidence intervals. In: Boston University School of Public Health.

Mai, L., Bao, L.-J., Shi, L., Wong, C. S., & Zeng, E. Y. (2018). A review of methods for measuring microplastics in aquatic environments. *Environmental Science and Pollution Research*, *25*, 11319-11332.

Milukow, H. A., Binns, A. D., Adamowski, J., Bonakdari, H., & Gharabaghi, B. (2019). Estimation of the Darcy–Weisbach friction factor for ungauged streams using Gene Expression Programming and Extreme Learning Machines. *Journal of Hydrology*, *568*, 311-321.

Neder, C., Fofonova, V., Androsov, A., Kuznetsov, I., Abele, D., Falk, U., Schloss, I. R., Sahade, R., & Jerosch, K. (2022). Modelling suspended particulate matter dynamics at an Antarctic fjord impacted by glacier melt. *Journal of Marine Systems*, *231*, 103734.

Ou, H., Liu, R., Liao, Z., & Zeng, E. Y. (2024). Occurrence and fate of microplastics in urban water management systems. In *Microplastic Contamination in Aquatic Environments* (pp. 181-228). Elsevier.

Qian, S., Qiao, X., Zhang, W., Yu, Z., Dong, S., & Feng, J. (2024). Machine learning-based prediction for settling velocity of microplastics with various shapes. *Water Research*, *249*, 121001.

Salimi, A., Noori, A., Ebtehaj, I., Ghobrial, T., & Bonakdari, H. (2024). Advancing Spatial Drought Forecasts by Integrating an Improved Outlier Robust Extreme Learning Machine with Gridded Data: A Case Study of the Lower Mainland Basin, British Columbia, Canada. *Sustainability*, *16*(8), 3461.

Shaghaghi, S., Bonakdari, H., Gholami, A., Ebtehaj, I., & Zeinolabedini, M. (2017). Comparative analysis of GMDH neural network based on genetic algorithm and particle swarm optimization in stable channel design. *Applied Mathematics and Computation*, *313*, 271-286.

Shamskhany, A., & Karimpour, S. (2022). Entrainment and vertical mixing of aquatic microplastics in turbulent flow: the coupled role of particle size and density. *Marine pollution bulletin*, *184*, 114160.

Vethaak, A. D., & Legler, J. (2021). Microplastics and human health. *Science*, *371*(6530), 672-674.

Xi, Y., Li, P., Pang, X., Han, Y., Lin, J., Wang, Q., Li, Y., & Yao, W. (2023). Numerical modelling for ecologically successful spawning-site restoration in Chin-sha River, China. *Marine and Freshwater Research*, *74*(15), 1324-1339.

Xu, R.-Z., Cao, J.-S., Ye, T., Wang, S.-N., Luo, J.-Y., Ni, B.-J., & Fang, F. (2022). Automated machine learning-based prediction of microplastics induced impacts on methane production in anaerobic digestion. *Water Research*, *223*, 118975.

5 Numerical Modeling of Large Spherical Microplastics Transport and Deposition using CFD-DEM

5.1 Abstract

The transport and deposition patterns of microplastics (MPs) in water are significantly influenced by the hydraulic characteristics of the surrounding fluid flow, including the water level, flow velocity, and the bathymetric and geometric conditions of the water bodies. Accordingly, this study aims to employ an Eulerian-Lagrangian numerical modeling approach to illuminate spherical MPs transport and deposition patterns by comparing different scenarios applied to flow and channel geometry. Various test scenarios were simulated to assess the impact of various variables, including the flow velocity (u_f), depth of turbulent flows (w), deepening of the channel bed (d), and slopes applied to the bottom of the channel bed (s). The utilized numerical model is based on the unresolved computational fluid dynamics (CFD) model coupled with discrete element method (DEM) solver, which was validated against laboratory experimental measurements. The results demonstrated that the CFD-DEM could simulate MPs transport and deposition with an accuracy of over 61%. Additionally, the model effectively captured the effects of hydraulic parameters (w, u_f, d, and s) on MPs deposition. It was concluded that CFD-DEM model is highly sensitive to the values of the sliding and rolling friction coefficients, and the number of particles considered for running simulations.

Keywords: Numerical Modeling, Microplastics, Transport, Deposition, CFD-DEM

5.2 Introduction

The widespread distribution of microplastics (MPs), driven by their high production rates and rapid industrial growth, poses a significant threat to the sustainability of aquatic ecosystems and biodiversity, thereby contributing to environmental pollution. For example, large micro-sized (≤ 5 mm) plastic particles (Rocha-Santos & Duarte, 2015) can be digested by aquatic fauna, enter the food chain, and persist without degradation (Alvarez-Zeferino et al., 2020). The dynamics of MPs in aquatic environments is influenced by various factors, including particle-specific characteristics (such as size, density, shape, and chemical composition), hydrodynamic conditions, and sediment characteristics of the ambient environment (Bigdeli et al., 2024; Bigdeli et al., 2022; Klaine et al., 2008; Masliyah, 1998; Wiesner & Bottero, 2017).

Previous studies have provided significant insight into the abundance, shape, color, and size of MPs in the aquatic environments (Ballent et al., 2016; Bujaczek et al., 2021; Castañeda et al., 2014; Corcoran et al., 2019). However, their transport and deposition patterns remain largely unknown, primarily due to the complexity and limited understanding of the processes governing MPs movement in such dynamic environments. This knowledge gap hinders our understanding of their environmental impacts on aquatic ecosystems.

Recent studies have demonstrated the effectiveness of numerical modeling tools, particularly Eulerian-Lagrangian models, in predicting the behavior of MPs in aquatic environments (Declerck et al., 2019; Díez-Minguito et al., 2020; Ghazizadeh et al., 2024; Isobe et al., 2019; Lebreton et al., 2012; Liubartseva et al., 2016; Maximenko et al., 2012; Pilechi et al., 2022; Van Sebille et al., 2015). Numerical modeling is a valuable tool for predicting the fate and transport of MPs, offering a cost-effective approach alternative to physical modelling and field surveys. It enables the prediction of pathways, identification of accumulation zones, and potential sources in aquatic environments, particularly in remote areas, where water quality monitoring is often impractical. However, it remains crucial to calibrate these with field or laboratory data to ensure their accuracy and reliability.

Deposition is a critical process influencing the transport of MPs in aquatic environments. Previous mass balance analyses of plastic pollution have revealed that a substantial portion of plastic entering these systems remains unaccounted for (Bigdeli et al., 2024; Bondelind et al., 2020b; Domercq et al., 2022). This gap suggests that our understanding of MPs deposition is incomplete and that much of the 'missing' plastic may have accumulated in sediment substrates.

Numerical simulations of deposition and transport of MPs in water bodies can be performed using Eulerian and Lagrangian models. Eulerian grid models operate within a fixed reference frame, unlike Lagrangian trajectory models, which employ a movable coordinate system in space (Van Utenhove, 2019). Lagrangian models, often referred to as particle-tracking methods (PTMs), focus on tracking individual particles, whereas Eulerian models address advection and diffusion processes at specific locations (computational nodes) (Van Sebille et al., 2018). PTMs are recognized as cost-effective and promising tools for interpreting MPs' behavior, offering valuable insights into their fate and transport in dynamic flow systems (Hardesty et al., 2017). Lagrangian models have the advantage of solving fewer equations per node since they do not compute

equations for every location in the mesh. However, the strengths and limitations of both methods make them complementary. Thus, these two approaches can be integrated, with Eulerian hydrodynamic models providing essential hydrological parameters as input for PTMs. By coupling particle-tracking models with hydrodynamic models, researchers can analyze potential trajectories of plastic debris on scales ranging from local (Lammerts, 2016; Rodríguez-Díaz et al., 2020; Stuparu et al., 2015) to global (Lebreton et al., 2012). This combination enables the assessment of MPs transport, deposition, distribution, residence time, and fate under various environmental conditions (Carlson et al., 2017; Critchell & Lambrechts, 2016; Ebbesmeyer et al., 2012; Isobe et al., 2009; Lebreton et al., 2012; Liubartseva et al., 2018; Van Utenhove, 2019).

There are two primary approaches for numerically modeling MPs particles. The first approach, known as the kinematic approach, treats particles as an passive entities that move with the surrounding flow field (Goniva et al., 2010; Pilechi et al., 2022). However, this method does not account for the local behavior of the individual particles. In contrast, the second modeling strategy (i.e., dynamic approach) simulates the motion of each particle individually. In other words, this approach treats particles as active entities whose motion is governed by a balance of forces such as gravity, friction, drag, and inertia, along with interactions with the surrounding medium. In the dynamic approach, the movement of particles is determined by the resultant external and internal forces acting on them, as described by the equation of motion (Pilechi et al., 2022). The most prominent models in this category are those based on the Discrete Element Method (DEM) and its variations. The DEM has the potential to capture all granular physical phenomena.

The Eulerian-Lagrangian CFD-DEM method (Anderson & Jackson, 1967) suggests calculating fluid motion by employing the Navier–Stokes equations within a fluid domain that is partitioned into cells, as is typical in the finite volume method. The trajectory of particles is modelled in the DEM model using the hydrodynamic forces calculated by the CFD model at each time step (Jérémy et al., 2020). DEM can also incorporate the interactions between fluid and different phases of particulate matter within (e.g., sediment and MPs) based on their shapes and forces they undergo (Y. Wang et al., 2019; Zhong et al., 2016). Further details about the coupling process of CFD and DEM has been provided in the subsequent section. Thus, in simulating particle trajectories, the DEM approach has been employed as a powerful tool in previous studies (Valyrakis et al., 2008; Zhong et al., 2016).

There are two well-known methods for modeling particle collisions that DEM is capable to employ: (1) soft particle and (2) hard particle, (also known as soft/hard sphere) approaches. In the soft particle approach, a pair of particles is allowed to deform or overlap during a collision that spans multiple time steps (Cundall & Strack, 1979). This makes it possible to calculate the elastic, plastic, and frictional forces between particles. Additionally, this approach allows for prolonged collisions between multiple particles, enabling the formation of chains or clusters, with all inter particle forces being accounted for during the collision. The soft particle approach has been considered the best balance between accuracy and computational effort in most cases (Aspherix®, 2024) such as dense granular flows (Gantt et al., 2006). In contrast, the hard particle method assumes that collisions are instantaneous and occur between only two particles at a time, meaning only one collision is considered per time step. Because of the instantaneous nature of these collisions, the forces between particles are often not explicitly calculated (Zhu et al., 2007).

The size difference between the particles and the mesh resolution influences the selection of the coupling methods, including unresolved, resolved, and hybrid methods. In the unresolved approach (Figure 24), most particles are smaller than the CFD cell size. Rigid and noncohesive particles are mostly simulated using an unresolved method. If the particles and mesh cells are of similar sizes, neither the resolved nor unresolved method alone is ideal, but a hybrid approach can be applied. For deformable and cohesive particles, it is recommended to use the resolved approach, in which the particle size is larger than the CFD cell size (Aspherix®, 2024). While the resolved method enhances accuracy, it also increases the computational effort required.

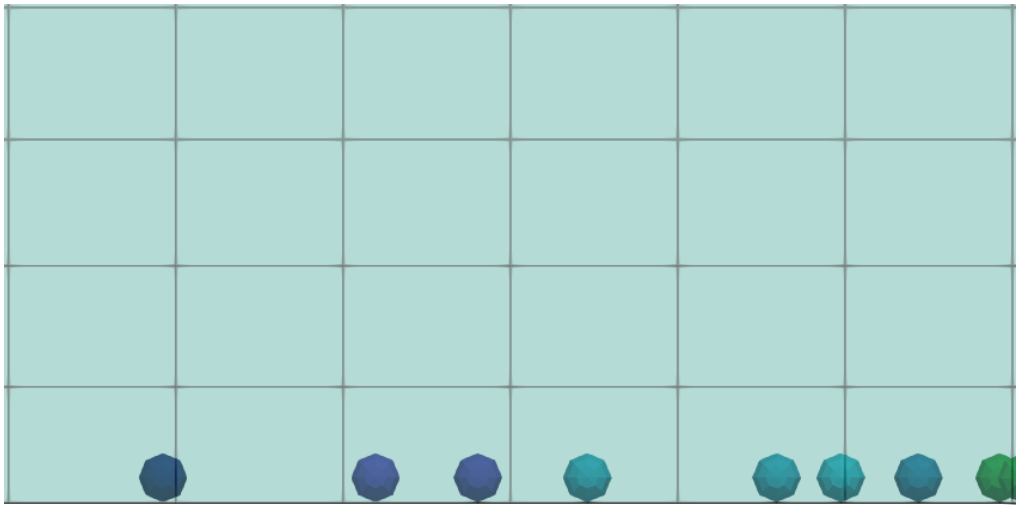

Figure 24. CFD-DEM coupling using the unresolved approach for simulating spherical MPs

The objective of this study is to investigate the capability of the coupled CFD-DEM (also known as CFDEM) by employing unresolved coupling method and soft particle collision approach to simulate spherical MPs that are denser than the flow (i.e., water). The MPs deposition patterns in some generic cases observed through laboratory test scenarios in a flume setup that mimics a natural channel. The scenarios that were simulated numerically included various hydraulic variables, such as the flow velocity, depth of turbulent flows, deepening in the depth of the channel, and slopes applied to the bed of the channel. Thus, CFD-DEM numerical simulations were implemented accordingly to assess the performance of the model. The validation process included the assessment of the performance of the model against laboratory measurements. The numerical results agreed well with the experimental observations. The analysis of key parameters such as the static and rolling friction coefficients, the coupling interval, DEM time-step, and the number of particles considered for running simulations revealed that they have significant influence of on the model's accuracy and predictive capability.

This paper is structured as follows: Section 5.3 outlines the methodology including experimental and numerical modeling, covering details such as the physical model setup, governing equations in the numerical model, and numerical model setup and configurations. Section 5.4 presents the results obtained from experimental observations and numerical simulations along with a discussion of the findings. Section 5.5 presents conclusions drawn from the implementation of the test scenarios numerically.

5.3 Methodology

5.3.1 Physical model

In this study, different test scenarios were conducted in a tilting flume at the National Research Council Canada Ocean, Coastal, and River Engineering Research Centre (NRC-OCRE) facility. Test scenarios consisted of different water levels (w), velocities of the flow (u_f), slopes (s) and deepening levels (d) applied to the channel bed within the field of view (FOV). The physical model setup as well as the implementation of the experimental procedure and test scenarios were considered the same as in the study conducted by Bigdeli et al. (2025). Out of 57 unique experimental tests, six physical model setups, including 18 test scenarios, were selected for the numerical modeling in this study, as shown in Table 15. Two water levels ($w = 0.1$ and $0.2\ m$), two velocities of flow ($u_f = 0.1$ and $0.3\ m/s$), two channel's bed deepening in the FOV ($d =$

$0, 0.035$ and 0.07 m), and three slopes applied to the channel's bed in the FOV ($s = 10°, 16.25°,$ and $22.5°$). The total MPs deposition within the FOV, as discussed previously (Bigdeli et al., 2025), was measured using trap efficiency (TE), which is the ratio of the number of deposited MPs to the total number of MPs entering the FOV. The flow water had a density of 1000 kg/m3. A total of 1000 polyethylene terephthalate (PET) particles were used as spherical MPs with a density of 1380 kg/m³. The spherical MPs had a diameter of 3 mm.

Table 15. Different model setups selected for numerical modeling

Model Setup	w (m)	u_f (m/s)	d (cm)	s $(^\circ)$
1	0.1 and 0.2	0.1 and 0.3	3.5	10
2	0.1 and 0.2	0.1 and 0.3	3.5	16.25
3	0.1 and 0.2	0.1 and 0.3	3.5	22.5
4	0.1 and 0.2	0.1 and 0.3	7	10
5	0.1 and 0.2	0.1 and 0.3	7	16.25
6	0.1 and 0.2	0.1 and 0.3	7	22.5

5.3.2 Numerical Modelling

As stated above, 18 test scenarios were simulated using the numerical method described below, maintaining the same initial and boundary conditions of the generic channel employed in the laboratory, as well as the same physical properties of the particles. Furthermore, the numerical approach includes a four-way coupling method, which accounts for the interaction between the fluid and particles (i.e., indicating a two-way simulation), as well as particle-particle collisions that demonstrate two-way modeling. This enhances the accuracy of the numerical simulation, making it a faithful representation of the real-world conditions.

5.3.2.1 CFD-DEM approach

The model used in this study comprises two primary phases: fluid (i.e., water) flow and spherical MPs particles. The motion of the particles were simulated using Discrete Element Method (DEM) by solving Newton's second law of motion for each individual particles, while the fluid flow was simulated using an OpenFOAM® (Jasak, 2009) which is an open-source CFD toolbox. The CFD

simulations were conducted using OpenFOAM's PISO solver, which applies the Finite Volume Method to solve the Navier–Stokes equations, calculating fluid pressure and velocity on an Eulerian mesh grid. This information is then passed to the DEM model at each CFD-DEM coupling interval to determine the forces (e.g., buoyancy, drag) acting on particles, and calculate their trajectories. The DEM modeling of this study was performed using Aspherix® (Aspherix®, 2024) which is coupled with OpenFOAM through the CFDEM® library (Goniva et al., 2010). Given the above descriptions and to gain better insight into the CFD-DEM coupling algorithm, a flowchart of the CFD-DEM coupling method is shown in Figure 25. Accordingly, the particulate system is solved using the DEM package, which results in obtaining dynamic information about the particles, such as their location and velocity in each fluid cell as well as forces affect their motion trajectory. Subsequently, the hydrodynamic forces, including drag, pressure gradient, and viscous forces, which are applied to the particles, are averaged over each fluid cell.

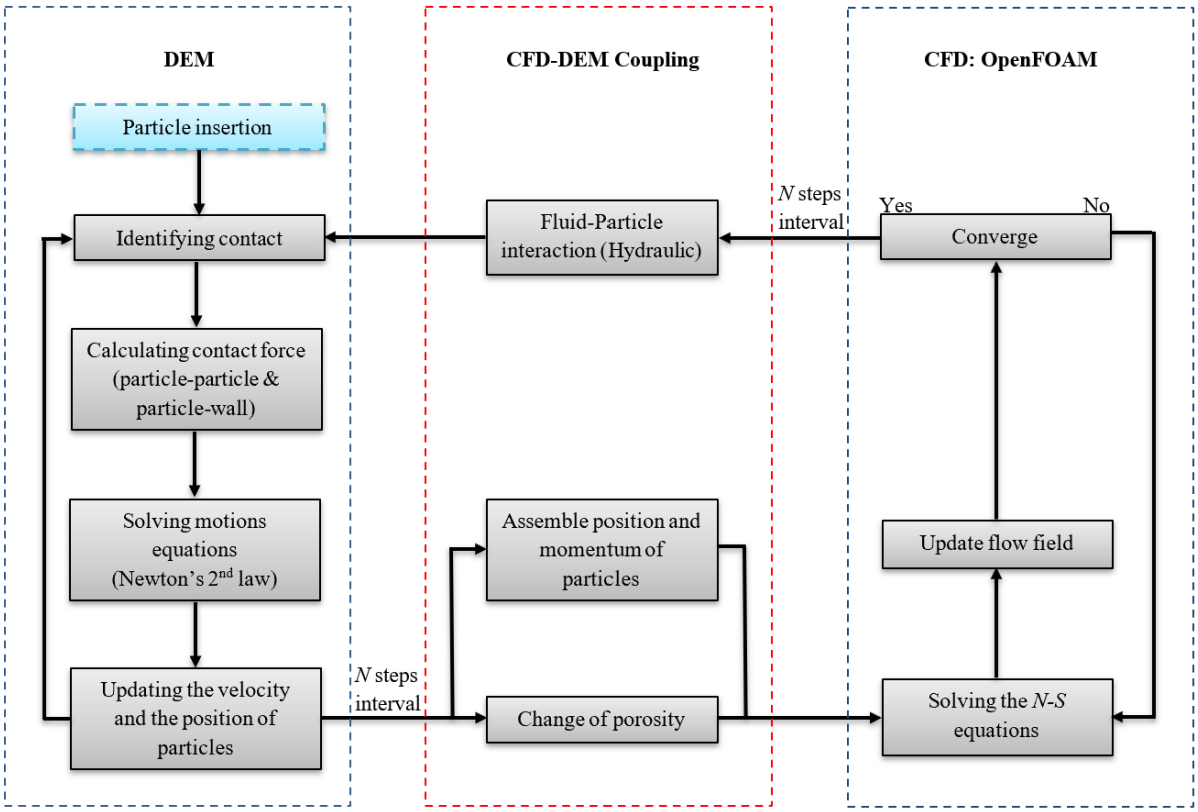

Figure 25. Flowchart of the CFD-DEM coupling method adapted from (Hu et al., 2019)

5.3.2.1.1 CFD

As stated above, the CFD modeling in this study was performed using the incompressible fluid solver in OpenFOAM, which calculates hydrodynamic properties, such as velocity and pressure, at each computational mesh cell by solving the Navier-Stokes equations (Bigdeli et al., 2022; Yin Wang et al., 2019). The solver does not account for free surface changes, which were considered negligible for the case investigated in this study. Since the CFD simulation was performed in conjunction with DEM, the CFD solver used a modified version of the governing equations to reflect the impact of particles occupying the Eulerian mesh cells, as follows:

$$\frac{\partial(\varepsilon_f \rho_f)}{\partial t} + \nabla.\left(\varepsilon_f \rho_f U^f\right) = 0 \tag{1}$$

$$\frac{\partial(\varepsilon_f \rho_f U^f)}{\partial t} + \nabla.\left(\varepsilon_f \rho_f U^f U^f\right) - \varepsilon_f \nabla.\left(\mu_f \nabla U^f\right) = -\nabla p + \varepsilon_f \rho_f g - f^{f,p} \tag{2}$$

where $\varepsilon_f = V_{void}/V_c = 1 - V_p/V_c$ indicates the porosity, also known as the void fraction (V_{void}, V_c, and V_p are the total void volume in a fluid cell, the total volume of the fluid cell, and the occupied volume due to particles, respectively), ρ_f represents the fluid density, t is time, U^f denotes the velocity vector of the flow, μ_f indicates the viscosity of the fluid, p indicates the pressure, g is the gravitational acceleration vector, and $f^{f,p}$ represents the drag force exerted by the particles on the fluid in the cell.

In this study, the standard $k - \varepsilon$ model was employed in the CFD modeling of the flow, which is one of the most widely used turbulence models in CFD simulations (Mohsenabadi et al., 2019). This method is based on the concept of eddy viscosity. Two partial differential equations known as transport equations can be solved using this turbulence model. The first is the turbulent kinetic energy (k) and the second is the turbulent eddy dissipation (ε), which is the dissipation rate of the turbulent kinetic energy. Further details can be found in Bigdeli et al. (2023) and Mohsenabadi et al. (2019).

5.3.2.1.2 DEM

The calculation of a particle's trajectory in DEM model is performed based on standard discrete element theory accounting for force and torque balances (Fonceca et al., 2021; Yin Wang et al., 2019):

$$m_i \frac{dU_i^p}{dt} = \sum_{j-1}^{n_i^c} F_{ij}^c + F_i^{f,p} + F_i^g \quad (3)$$

$$I_i \frac{d\omega_i}{dt} = \sum_{j-1}^{n_i^c} M_{ij} \quad (4)$$

where m_i denotes the mass of particle i, U_i^p is the translational velocity of particle i, F_{ij}^c is the contact force applied by particle j or the wall(s) on particle i. $F_i^{f,p}$ and F_i^g are the particle-fluid interaction (including drag force in this case) and gravitational forces, respectively, which act on particle i in the fluid-phase cell, as shown in Figure 26. I_i represents the moment of inertia and ω_i is the angular velocity of particle i, and M_{ij} is the torque exerted by particle j or the wall(s) on particle i. It should be noted that there are other forces, such as viscosity, which should be considered in the formulation of different fluid-particle interactions, as explained in depth by Smuts (2015). Viscous force arises from the shear stress within the fluid caused by its velocity gradient. Accordingly, this force drives particles towards areas of reduced shear (Smuts, 2015). This force was considered to be small in this study since it becomes significant when particles are large, the surrounding fluid is highly viscous, the relative velocities between particles are high (such as during a potential collision), and the distance between particles is much smaller than their radius.

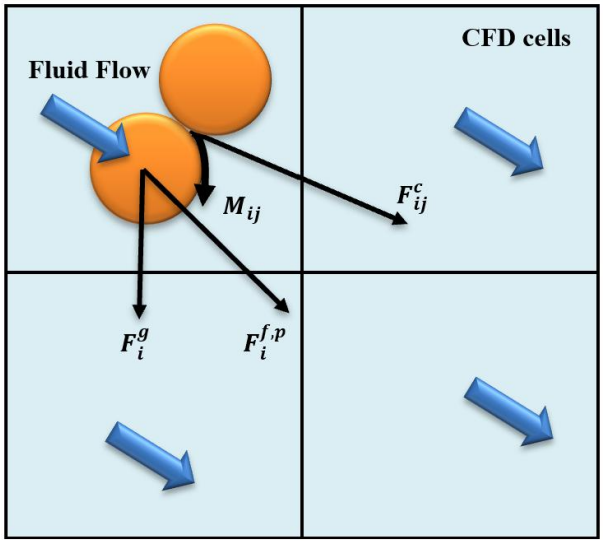

Figure 26. Schematic diagram of CFD cells including fluid flow, and drag forces and torques exerted on particles adapted from (Yin Wang et al., 2019)

There are various equations in the literature (Smuts, 2015; Yin Wang et al., 2019; Zhu, 2019) which have been proposed as equations for calculating the drag force ($F_i^{f,p}$) (e.g., Di Felice (Di Felice, 1994) and Koch and Hill (Koch & Hill, 2001). It has been reported that the Di Felice model is a promising model for developing relations of the drag force around a single particle in multiphase systems that include non-spherical particles (Yin Wang et al., 2019).

However, the more recent drag force model, i.e., the Koch and Hill correlation (Koch & Hill, 2001), considers particle-particle interactions based on lattice-Boltzmann simulations (Smuts, 2015; Van Buijtenen et al., 2011; Vangö, 2019; Yin Wang et al., 2019; Zhu, 2019). Therefore, in this study, the Koch and Hill model (Koch & Hill, 2001) was employed because it provides a better estimation of drag forces around particles based on the literature (Smuts, 2015) compared with other models such as Di Felice (Di Felice, 1994).

The combination of the Hertz contact model with Coulomb's friction law was utilized to characterize the interaction between particles in both the normal and tangential directions (Ma et al., 2019; Smuts, 2015). The Hertz contact model, including the non-linear contact relationship, was employed to calculate the normal elastic force (Ma et al., 2019). Tangential shear forces can be generated during collisions, leading to the development of a torque. Many models apply a Coulomb-type friction law, occasionally incorporating damping, to calculate tangential contact force. It is important to note that the Coulomb's friction criterion limits the tangential force using the sliding friction coefficient (Ma et al., 2019).

The model parameters were set to the values listed in Table 16. Key parameters selected during implementation of coupled CFD-DEM simulations. To reduce computational time, the stiffness of the particles is specifically reduced by lowering the Young's modulus value. This commonly used technique allows for the use of larger time steps in simulations. (Smuts, 2015; Xiong et al., 2021). Selecting the Young's modulus in DEM serves as a preliminary stage in simulation, given its critical role in determining the DEM's time step and assessing particle overlap (Xiong et al., 2021). A broad spectrum of Young's modulus values (ranging from 10^6 to 10^{10} Pa) has been employed in numerical simulations to analyze particulate systems (Akbarzadeh, 2014; Hu et al., 2019; Kong et al., 2021; Ma et al., 2019; Smuts, 2015; Xiong et al., 2021). Relaxing the stiffness of particles prolongs their contact duration, enabling the utilization of larger time steps while ensuring an adequate resolution of collision events. Furthermore, the literature indicates that reducing

magnitude of the Young's modulus does not substantially impact the physical behavior of the particulate system. In other words, studies have demonstrated that reducing the particle stiffness by two to three orders of magnitude typically does not significantly alter the overall behavior of simulations (Hoomans et al., 1996; Tsuji et al., 1993; Wassgren & Sarkar, 2008). In this study, the Young's modulus was set to 5 MPa in the particulate phase for both particle-particle and particle-wall contacts according to the literature (Ma et al., 2019). In addition, the restitution coefficient, which represents the ratio of the rebound velocity of a particle to its velocity before the collision with other particles, was set to 0.5 (Ma et al., 2019; Xiong et al., 2021) to consider energy dissipation within the fluid-particulate system.

Unlike sliding friction, which limits the tangential force, rolling resistance is frequently employed as a practical method to estimate the influence of the particle shape, as observed in various studies (Ai et al., 2011; Cheng et al., 2017; Estrada et al., 2011; Iwashita & Oda, 1998). It is quantified through a torque that accounts for particle rotation which has been described in depth by Ma et al. (2019). In this study, the sliding and rolling friction coefficients were set to 0.01 and 0, respectively, in both particle-particle and particle-wall interactions to represent the closest results to the real condition.

Table 16. Key parameters selected during implementation of coupled CFD-DEM simulations

Fluid (CFD)/Particulate (DEM) phase items	**Parameter**	**Selected value**
Fluid phase (water flow at 20℃ and 1 atm)	Density (kg/m^3)	998.2
	Viscosity (Pa.s)	1×10^{-3}
	CFD cell size (m)	1×10^{-2}
Particulate phase (spherical particles)	Particle Number	500
	Particle Density (kg/m^3)	1300
	Radius (mm)	3
	Young's modulus (particle-particle contact) (MPa)	5
	Young's modulus (particle-wall contact) (MPa)	5
	Poisson's ratio	0.3

Fluid (CFD)/Particulate (DEM) phase items	Parameter	Selected value
	Restitution coefficient	0.5
	Interparticle sliding friction coefficient	0.01
	Particle-wall sliding friction coefficient	0.01
	Interparticle rolling friction coefficient	0
	Particle-wall rolling friction coefficient	0
Simulation timesteps	DEM Time step (s)	1×10^{-5} and 2×10^{-5}
	CFD Time step (s)	1×10^{-3} and 2×10^{-3}
	Coupling Interval	10 and 100
Global coupled CFD-DEM settings	Gravitational acceleration (m^2/s)	9.81

In Aspherix®, the critical time step size is determined using two main criteria: the Rayleigh and Hertz criteria (Aspherix®, 2024). Li et al. (2005) suggested that it is reasonable to assume that all energies are transferred via Rayleigh waves on the particle surface in the simulations. Kremmer and Favier (2001) observed that calculating the critical time step size based on the Rayleigh wave frequency is a common practice. Typically, the Rayleigh criterion is more significant, particularly for dense systems, while the Hertz criterion is more applicable to dilute systems (Smuts, 2015). Rayleigh time (T_R) refers to the duration required for a wave to travel through a solid particle (Aspherix®, 2024; Li et al., 2005). This can be estimated as follows (Aspherix®, 2024; Li et al., 2005):

$$T_R = \pi R \left(\frac{\rho}{G}\right)^{\frac{1}{2}} / (0.1631v + 0.8766) \quad (5)$$

$$G = \frac{Y}{2(v+1)} \quad (6)$$

where R and ρ denote particle radius and density, respectively. G is the shear modulus. v is Poisson's ratio, and Y represents Young's modulus of the particle.

It is advised to use a simulation DEM time-step between 0.1 T_R and 0.3 T_R (Aspherix®, 2024). However, a simulation time-step can be also selected according to the duration of particle contact proposed in the Hertzian contact theory, which depends on the relative velocity between particles, their mass, radius, Poisson's ratio, and Young's modulus (Y^*) as follows (Aspherix®, 2024; Li et al., 2005):

$$t_{contact,H} = 2.87\left(\frac{m^{*2}}{r^* Y^{*2} v_{rel}}\right)^{1/5} \tag{7}$$

$$m^* = \left(\frac{1}{m_1} + \frac{1}{m_2}\right)^{-1} \quad , \quad r^* = \left(\frac{1}{r_1} + \frac{1}{r_2}\right)^{-1} \tag{8}$$

$$Y^* = \left(\frac{1-v_1^2}{Y_1} + \frac{1-v_2^2}{Y_2}\right)^{-1} \tag{9}$$

It is recommended that a small fraction of the Hertz contact time ($t_{constact,H}$), typically 5%-15%, be used as the DEM time-step (Aspherix®, 2024). This approach ensures that the contact is accurately resolved, thereby preventing an excessive overlap of energy. In this study, T_R and $t_{constact,H}$ were calculated to be 0.00014 s and 0.00039 s, respectively. Accordingly, the DEM time step size considering both the Rayleigh and Hertz contact time criteria was calculated to be 2×10^{-5} s.

5.3.2.1.3 CFD-DEM coupling configuration

The contribution of particles to the fluid flow can be incorporated with two common formulations, called the "Model A" and "Model B", which are employed in different fluid flow-particle applications (Smuts, 2015). In both Model A and Model B, the total fluid-particle interaction force which is applied on an every individual particle, is the sum of the drag, pressure gradient, and viscous forces (typically considered as the dominant forces in interactions between the particle and the fluid), and the combined effect of other less significant particle-fluid interaction forces, including buoyancy, virtual mass, Saffman lift, Magnus force, and others (Smuts, 2015). These two models differ primarily based on how they treat the pressure-source term in the formulations (i.e., governing equations). Model B assumes that the pressure originates only from the fluid phase while it is attributed to both the fluid and particle (solid) phases in Model A by including the void fraction (Smuts, 2015; Zhou et al., 2010). In addition, the pressure gradient force, excluding the buoyancy force, was combined with the drag force in Model B. While this approach works when

the forces are aligned in the same direction. It may not be appropriate for all flow systems where this condition doesn't hold (Smuts, 2015). In this study, Model A was employed in the implementation of coupling to obtain a better estimation of pressure than Model B (Smuts, 2015; Zhou et al., 2010). On the other hand, cfdemSolverPiso was employed, in this study, to couple CFD (i.e., $k-\varepsilon$ model) and DEM models, for handling the exchange of particle momentum (Smuts, 2015). The cfdemSolverPiso solver (Smuts, 2015) is a developed version of OpenFOAM pisoFoam solver. It is recommended that the size of the fluid cell be several times larger than the particle diameter (Hu et al., 2019), which was confirmed in this study. In addition, to obtain more accurate results, as reported in the literature (Hu et al., 2019; Smuts, 2015), and given that CFD and DEM are run separately, it is recommended to consider a CFD time step 50–100 times larger than that of the DEM. In this study, the time interval was set to 100, after implementing a sensitivity analysis.

The voidFractionModel determines the volume of the DEM particles within the CFD domain. It is advised to use the "divided" sub-model, as employed in this study, when particle sizes are comparable to that of a CFD cell (Smuts, 2015). This approach employed satellite points to distribute a particle's volume across the cells it intersects, making it more accurate than the "center" model, which assumed that the entire mass is concentrated in the cell containing the particle's center (Smuts, 2015), as shown in Figure 27. In other words, it is assumed that all particle volume is placed into the cell encompassing the particle center in the center sub-model (Figure 27a) while in the divided sub-model, the particle volume is distributed over several cells using splitting the particle into satellite points when the particle volume spans cell boundaries (Figure 27b). To use the voidFractionModels, the void fraction should be positive (i.e., $\varepsilon_f > 0$) and it is recommended $\varepsilon_f > 0.2$ (Aspherix®, 2024).

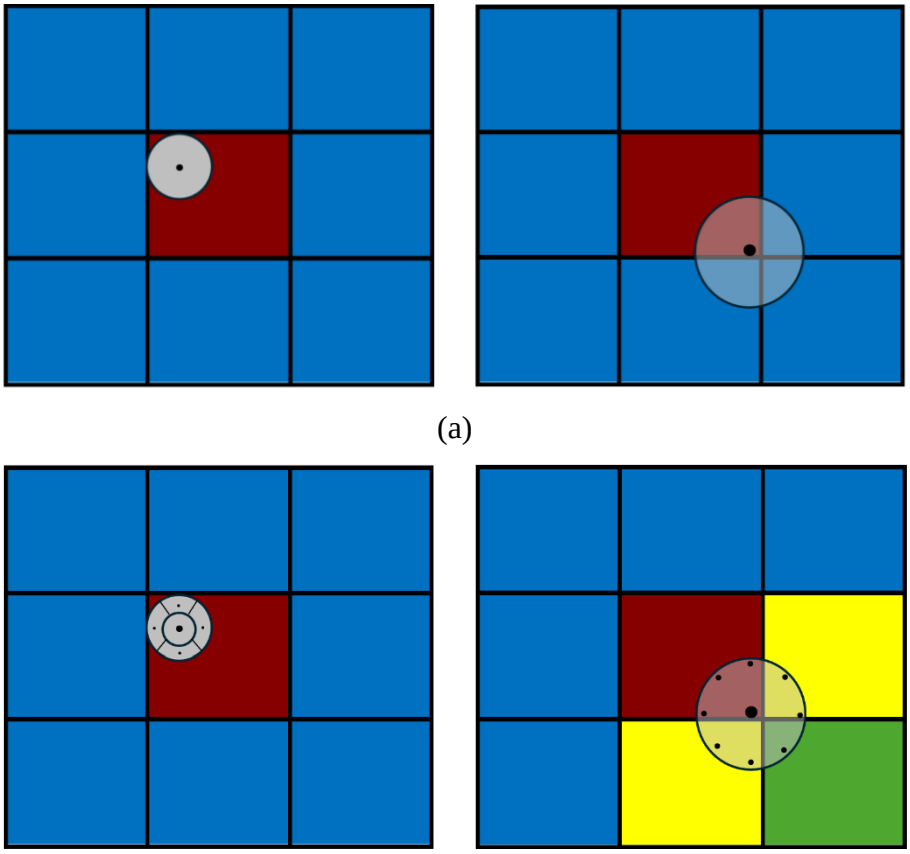

Figure 27. Different approaches employed in the voidfractionModel, as the sub-model, for calculating the void fraction: (a) center and (b) divided

5.3.2.2 Numerical model setup

The computational domains used of the CFD-DEM simulations was created with the same dimensions and initial and boundary conditions as the physical model setups discussed above to be able to compare the results with the experimental observations. The mesh was built with a domain size of 4.2 and 0.2 meters in x and z-direction. The size of the domain in the y-direction varied according to each test scenario. MPs particles were injected into the flow on the channel bed, 0.2 m ahead of the FOV. Figure 28 depicts a section of the computational domain corresponding to the field of view in the laboratory experiment. It is important to note that to use the unresolved approach, the size of CFD cells should be larger than particles size. This is necessary to ensure that there is a balance between the accuracy of the flow and accuracy of particles while maintaining the feasible computational effort.

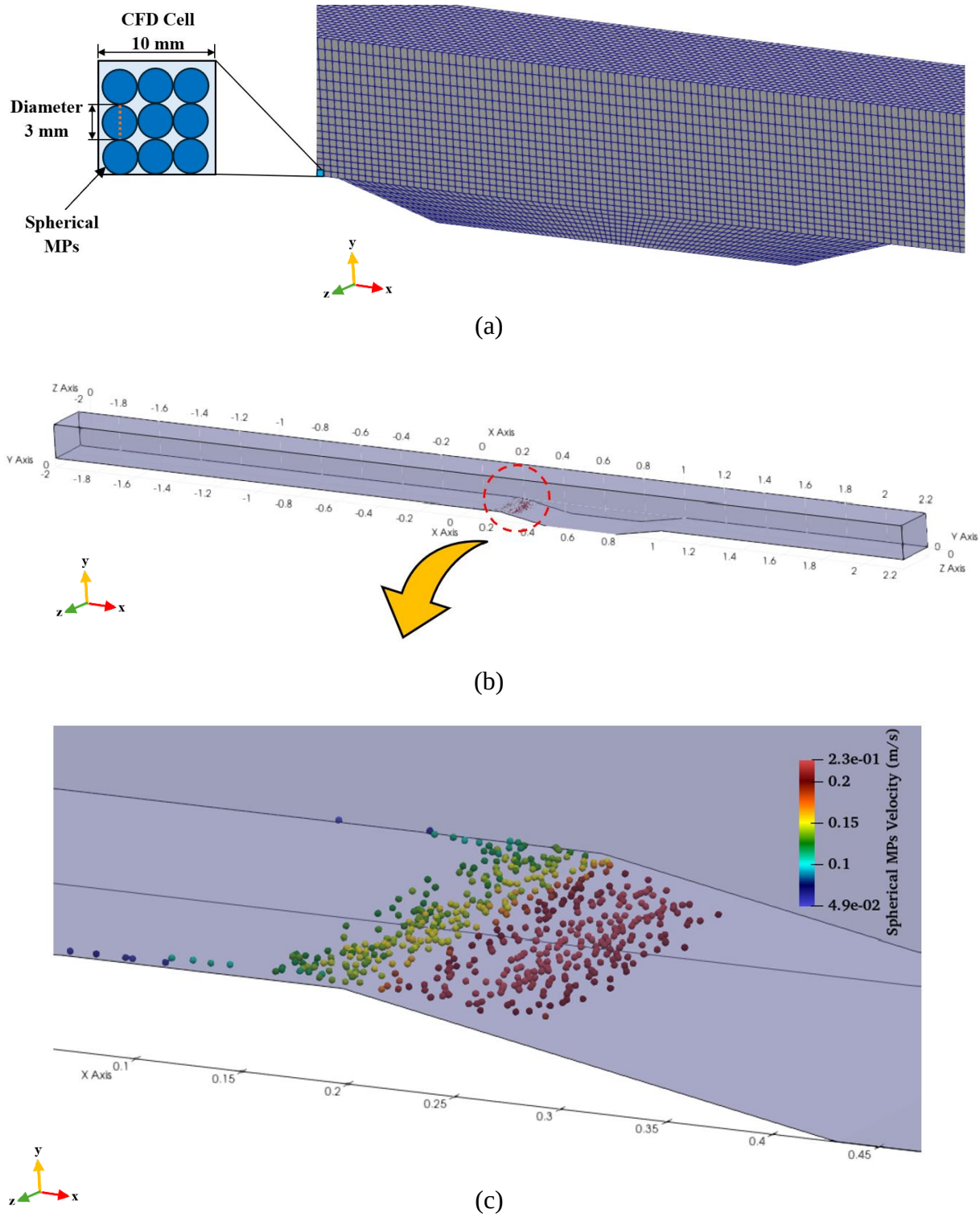

2671

2672 **Figure 28.** Snapshot of the computational domain: (a) mesh configuration, (b) full size, and (c) an
2673 example of the simulated MPs distribution within the FOV.

The mesh size was refined close to the bottom of the channel and corners several times to improve the model stability (see Figure 28a). Mesh considerations play a crucial role in CFD-DEM method, where it is commonly assumed that DEM particles should be considerably smaller than CFD cells. However, there is a lack of established criteria regarding the extent of this size difference (Smuts, 2015). The sizing is often specific to each case, with the cell dimensions adjusted according to the problem requirements. Nonetheless, empirical observations suggest that cell dimensions should be approximately 3-4 times the particle diameter (Smuts, 2015). This range typically represents the lower threshold because choosing cell size less than it leads to cells being excessively filled with particles, leaving inadequate space for fluid.

All surfaces of the channel were assumed to be smooth during numerical simulations. The lower boundary and sidewalls were set as "wall", and the inlet and outlet were set as a "patch" representing open boundaries in the OpenFOAM model. Constant atmospheric pressure, zero shear stress, and zero gradient for turbulence quantities were considered as boundary conditions to account for the air-water interactions (Bigdeli et al., 2023). The detailed boundary conditions employed for running the simulations are shown in Table 17. Boundary conditions selected in OpenFOAM® for $k-\varepsilon$ model.

Table 17. Boundary conditions selected in OpenFOAM® for $k-\varepsilon$ model

Boundary	***U***	***P***	***k***	***ε***	***nut***
Inlet	U.F.V[1]	Z.G[5]	T.K.E.I [7]	Z.G	C[10]
Outlet	I.O[2]	f.V[6]	I.O	I.O	C
Top	S[3]	Z.G	Z.G	Z.G	Z.G
Channel Bed	N.S[4]	Z.G	K.R.W.F[8]	E.W.F[9]	N.K.W.F[11]
Side Walls	N.S	Z.G	K.R.W.F	E.W.F	N.K.W.F

[1] uniformFixedValue [5] zeroGradient [9] epsilonWallFunction

[2] inletOutlet [6] fixedValue [10] calculated

[3] slip [7] turbulentIntensityKineticEnergyInlet [11] nutkWallFunction

[4] noSlip [8] kqRWallFunction

To calibrate and validate the numerical simulations, test 2 was selected for calibration and the other tests were considered for validation using four hydraulic parameters including w, u_f, d, and s. In addition, three mesh sizes (i.e., fine, medium, and coarse) were considered for the sensitivity analysis of simulations, as depicted in Table 18. Different configurations used for implementing the sensitivity analysis of the mesh for Test 2.

Table 18. Different configurations used for implementing the sensitivity analysis of the mesh for Test 2

Mesh size	Total number of cells	Cell type	Minimum cell size (m)	Maximum cell size (m)
Fine	138,800	hexahedra	0.005	0.01
Medium	38,400	hexahedra	0.01	0.02
Coarse	4,720	hexahedra	0.01	0.03

Accordingly, the size of the domain and the total number of cells in the computational domain for each test scenario based on the fine mesh were listed in Table 19. Different test scenarios selected for numerical modeling. Detailed characteristics of the 18 tests are provided in Section 5.4.1 (Table 20).

Table 19. Different test scenarios selected for numerical modeling

Test Scenario	Model Setup	Size of the domain in each direction (x, y, z)	Total number of cells in the domain
1	1	4.2 m, 0.1668 m, 0.2 m	122,000
2	1	4.2 m, 0.189 m, 0.2 m	138,800
3	1	4.2 m, 0.2758 m, 0.2 m	220,800
4	2	4.2 m, 0.1671 m, 0.2 m	122,000
5	2	4.2 m, 0.2098 m, 0.2 m	155,600
6	2	4.2 m, 0.2768 m, 0.2 m	214,400
7	3	4.2 m, 0.1624 m, 0.2 m	113,600
8	3	4.2 m, 0.1934 m, 0.2 m	138,800
9	3	4.2 m, 0.2642 m, 0.2 m	197,600
10	4	4.2 m, 0.1679 m, 0.2 m	108,400

Test Scenario	Model Setup	Size of the domain in each direction (x, y, z)	Total number of cells in the domain
11	4	4.2 m, 0.211 m, 0.2 m	150,400
12	4	4.2 m, 0.2833 m, 0.2 m	209,200
13	5	4.2 m, 0.169 m, 0.2 m	116,800
14	5	4.2 m, 0.2027 m, 0.2 m	142,000
15	5	4.2 m, 0.2855 m, 0.2 m	217,600
16	6	4.2 m, 0.1726 m, 0.2 m	116,800
17	6	4.2 m, 0.1956 m, 0.2 m	142,000
18	6	4.2 m, 0.2871 m, 0.2 m	217,600

5.3.2.3 Sensitivity analysis

Several sensitivity analyses were performed to investigate the effects of different factors, such as the CFD mesh size, number of plastic particles, coupling interval, values of sliding and rolling friction coefficients, and the DEM time step size. Accordingly, 250, 500, and 1000 plastic particles were simulated separately to determine if there is a possibility, based on the obtained numerical results for TE, to execute the numerical model with fewer particles to decrease computational time (i.e., reducing computational costs). The simulation results described in section 5.4 showed that the optimal number for simulating MPs particles is 500 particles.

Several mesh configurations were investigated, featuring a finer mesh near the channel's bed and corners and a coarser mesh towards the water surface. To determine the optimum mesh size, a sensitivity analysis was conducted using three different combination numbers in the x (110, 220, and 420), and z (8, 16, and 20) directions (Figure 28). The y-direction values varied with an expansion ratio of 1:2 depending on the characteristics of each test scenario. As stated in section 5.4, it was concluded that grid number of 420 in the x-direction and 20 in the z-direction is optimal.

Various combinations of sliding and rolling friction coefficients were also examined to identify the values that best align the numerical simulations to the experimental observations. The result indicated that the sliding (f_s) and rolling (f_r) friction coefficients of less than 0.1 provided the closest match to the experimental data. Accordingly, four combinations were used $f_s = 0.1$ and $f_r = 0.05$, $f_s = 0.05$ and $f_r = 0.1$, $f_s = 0.05$ and $f_r = 0.05$, and $f_s = 0.01$ and $f_r = 0$. The optimal combination was found to be $f_s = 0.01$ and $f_r = 0$, as described in section 5.4.

Three coupling intervals, defined as the number of steps between the CFD and DEM models: 10, 50, and 100. Additionally, two DEM time-step sizes of 1×10^{-5} s and 2×10^{-5} s, were evaluated for the stability and computational efficiency. The coupling intervals of 10 and 100, and combined with DEM time-steps of 1×10^{-5} s and 2×10^{-5} s was found to run stably, as further explained in section 3.3.

5.4 Results and discussion

In this section, we analyze the result from the laboratory experiments along with the CFD-DEM simulations for the various tested scenarios. The total deposition of MPs within the FOV is compared between the experimental and simulated data. Additionally, a sensitivity analysis is conducted on the numerical model performance, focusing on several key parameters: mesh configuration, DEM time step size, sliding and rolling friction coefficients, coupling interval values, and the total number of particles simulated by the numerical model. This comprehensive analysis aims to identify the optimal conditions for accurate and efficient simulations.

5.4.1 Laboratory observations

18 experimental cases, selected from Bigdeli et al. (2025), were investigated as shown in Table 20. The cases were selected to ensure comparability in terms of how each hydraulic parameter influences the TE value. For example, cases with similar hydraulic parameters but varying flow velocities were included among the 18 selected cases in this study.

Several findings can be derived from the comparison of TE values in the tests conducted. First, when water velocity is low (approximately 0.1 m/s), most MPs are deposited within the FOV. This is because the flow velocity near the bed is slower than in cases with higher flow velocities (e.g., 0.3 m/s), irrespective of hydraulic factors such as w, d, and s. This highlights the significant influence of water velocity on the TE value compared to other factors. Second, in higher flow velocities ($u_f = 0.3\ m/s$), the deposition of MPs is notably affected by doubling the channel bed depth in tests with slopes of $s = 16.25^\circ$ and 22.5°. This contrasts with observations from tests with a slope of 10°, where steeper slopes resulted in greater water depth, reducing flow velocity due to the continuity equation. Third, TE values generally increase as the channel bed slope becomes steeper, which is expected. Steeper slopes reduce particle velocity, regardless of the values of w, u_f, and d.

Table 20. Characteristics of 18 experimental tests selected for numerical modeling

Test No.	$w\ (m)$	$u_f\ (m/s)$	$d\ (cm)$	$s\ (^\circ)$	TE
1	0.1	0.1	3.5	10	0.95
2	0.1	0.3	3.5	10	0.07
3	0.2	0.3	3.5	10	0.118
4	0.1	0.1	3.5	16.25	0.99
5	0.1	0.3	3.5	16.25	0.088
6	0.2	0.3	3.5	16.25	0.11
7	0.1	0.1	3.5	22.5	1
8	0.1	0.3	3.5	22.5	0.10
9	0.2	0.3	3.5	22.5	0.16
10	0.1	0.1	7	10	0.98
11	0.1	0.3	7	10	0. 13
12	0.2	0.3	7	10	0.17
13	0.1	0.1	7	16.25	1
14	0.1	0.3	7	16.25	0.99
15	0.2	0.3	7	16.25	1
16	0.1	0.1	7	22.5	1
17	0.1	0.3	7	22.5	1
18	0.2	0.3	7	22.5	1

5.4.2 Numerical simulation results

To evaluate the capability of CFD-DEM model, digital replications of the scenarios tested in the experimental work were developed. The predicted trap efficiency (TE) from the model was compared with the lab measurements. The model's performance in terms of the accuracy was reported using the relative accuracy (RA) parameter, which was defined by the formula below, with the results presented in Figure 29:

$$RA = 1 - \frac{(|x_i - y_i|)}{|x_i|} \quad (10)$$

where x_i and y_i are experimental and numerical TE values, respectively.

The numerical model showed an accuracy of over 61% in predicting the TE values for the selected test scenarios (showed in Table 20). The lowest accuracy was observed for Test 6, in which the hydraulic parameters were set to $w = 0.2\ m, u_f = 0.3\ m/s, d = 3.5\ cm$, and $s = 16.25^\circ$. For this test, the model overestimated the TE value (15.3%) during the numerical simulation compared to the observed TE value (11%) in the laboratory (indicating approximately 61% accuracy).

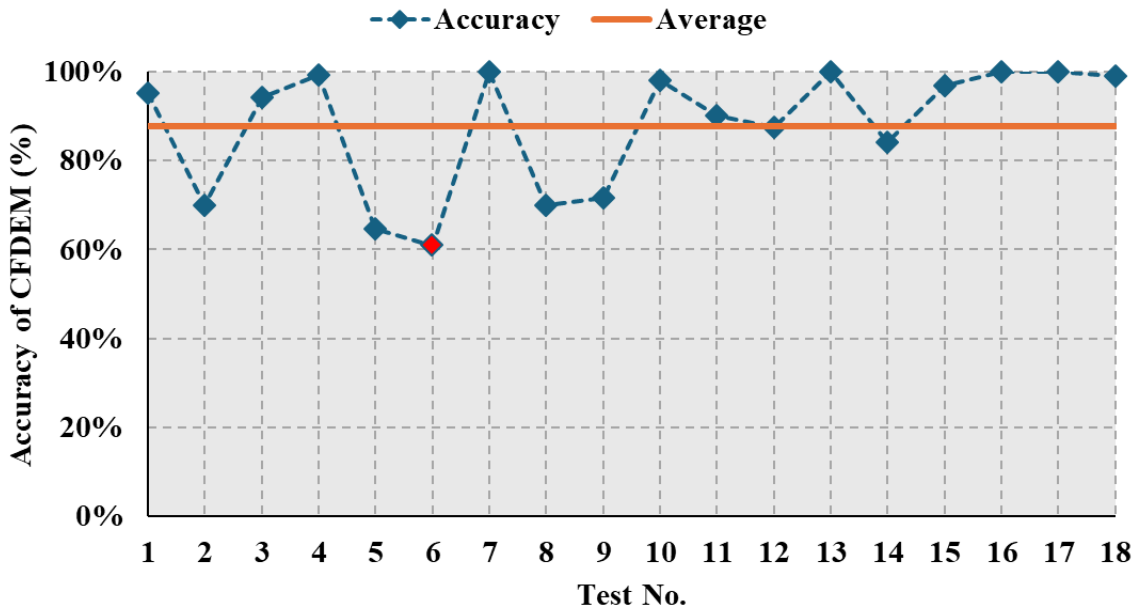

Figure 29. The accuracy of CFD-DEM in simulating TE values based on experimental observations

To evaluate the impact of various parameters on particle behaviour and CFD-DEM performance the simulated TE values were compared with experimental data, as shown in Figure 30, Figure 31, and Figure 32. Each figure depicts the variation of a single parameter – bed deepening depth (d), water velocity (u_f), and water level (w) – allowing for the isolated analysis of the individual effect of different parameters on TE values. In each figure, the individual TE graphs were also grouped for pairs of tests with the same bed slope within the FOV, allowing for a clearer comparison of results under similar conditions. The cases with steeper slopes were associated with greater water depth at the bed deepening, which resulted in slower velocities and increased deposition. These

trends were also captured by the CFD-DEM model as shown in Figure 30. In tests 2, 5, and 8, tripling the flow velocity resulted in a significant reduction in TE values (by more than 80%) compared to the corresponding tests 1, 4, and 7, as shown in Figure 30a. However, this effect was not observed when the bed deepening depth was doubled in steep-slope scenarios, such as in tests 14 and 17 (Figure 30b).

On the other hand, by providing results close to experimental observations, CFD-DEM was reasonably capable of simulating tests in which the water level changed. As depicted in Figure 31, the simulations captured the effect of the water level on TE values despite the existing error between the numerical and experimental results. In this regard, the higher water depth leads to lower particles velocity on the bed, resulting in larger deposition rate (i.e., TE). The TE values of tests with doubled water depth showed a slight increase of less than 6%, regardless of the doubling of d and the value of s (Figure 31a and Figure 31b).

The model also performed well in capturing the effect of changes in deepening of the channel bed within the FOV area, as shown in Figure 32, when comparing the numerical and experimental results in terms of increasing the depth of the channel bed. This leads to increase in the water depth and results in higher values of TE. Doubling d led to a significant increase (over 80%) in TE values, in steep-slope scenarios (Figure 32a and Figure 32c). However, this effect was not observed in cases where MPs experienced low water depth and flow velocity (i.e., $w = 0.1\,m$ and $u_f = 0.1\,m/s$), as illustrated in Figure 32b.

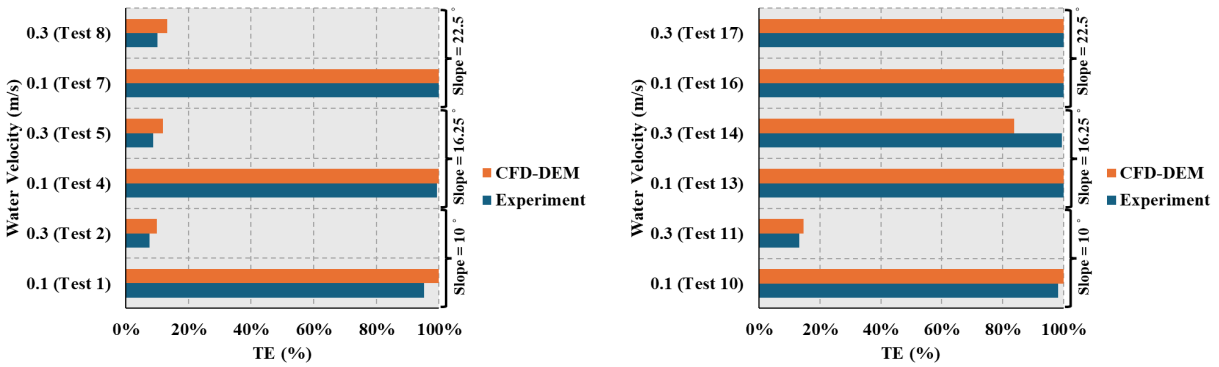

(a) (b)

Figure 30. CFD-DEM results for tests in which the water velocity is varying while the other parameters maintained constant: (a) tests in which $d = 3.5\,cm$, (b) tests in which $d = 7\,cm$

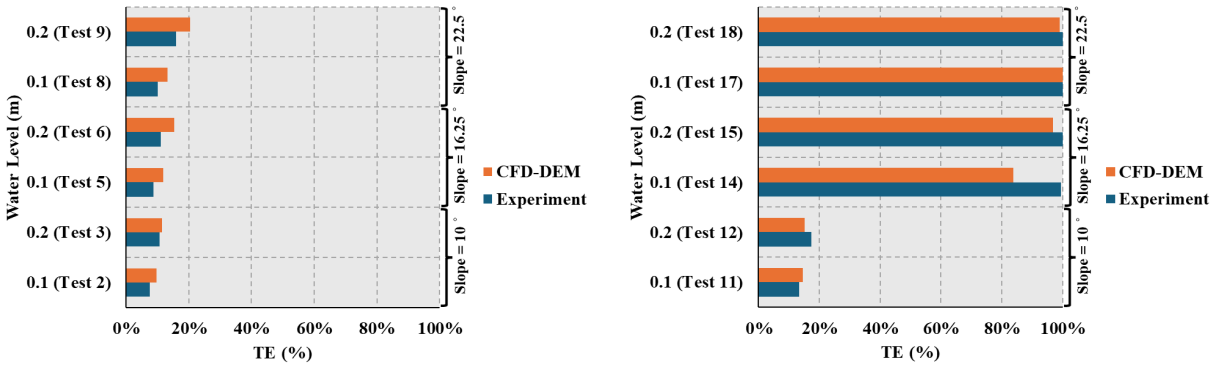

(a) (b)

2801 **Figure 31.** CFD-DEM results for tests in which the water level is varying while the other
2802 parameters maintained constant: (a) tests in which $d = 3.5\ cm$, (b) tests in which $d = 7\ cm$

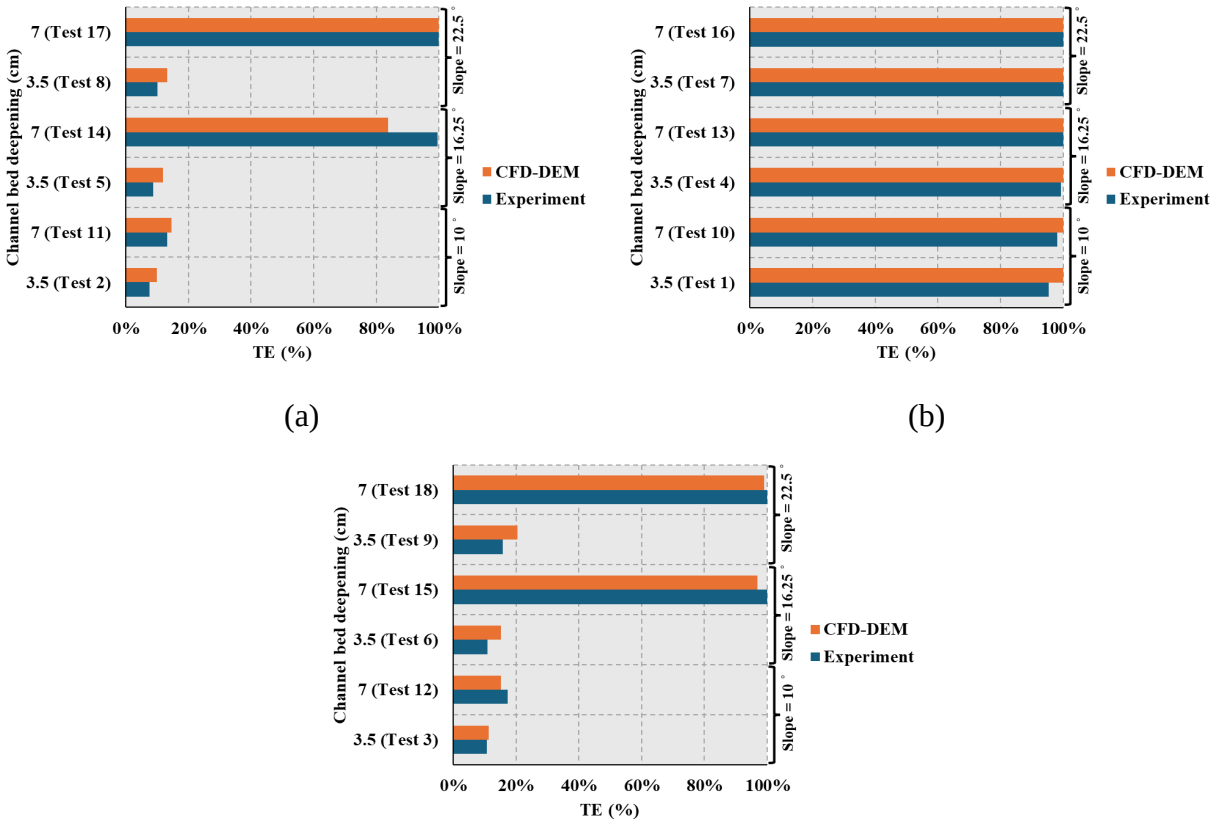

(a) (b)

(c)

2803 **Figure 32.** CFD-DEM results for tests in which the channel bed deepening is varying while the
2804 other parameters maintained constant: (a) tests in which $w = 0.1\ m$ and $u_f = 0.3\ m/s$, (b) tests
2805 in which $w = 0.1\ m$ and $u_f = 0.1\ m/s$, and (c) tests in which $w = 0.2\ m$ and $u_f = 0.3\ m/s$

To investigate the pattern of MPs deposition within the FOV in greater detail, tests 2, 5, and 8 were chosen for further analysis based on the results of the numerical model for 10 s of simulation, as depicted in Figure 33. The selected cases are completely similar to each other in terms of the hydraulic parameters except for the slope applied to the channel bed. In addition, they were among the cases in which CFD-DEM simulated MPs deposition and transport with the lowest accuracy (see Figure 29). The streamwise flow velocities in tests 2, 5, and 8, were simulated 0.37, 0.33, and 0.35 m/s that were very closed to the experimental observations.

In general, particles located near the center line within the FOV are transported faster compared to those on the sides due to the higher value of the flow velocity in the centerline compared to edges. Conversely, particles located close to the sides of the channel are more likely to deposit due to lower velocity in these regions, which is influenced by the wall effects. In addition, an increase in the slope results in a higher water depth and lower flow velocity (due to the continuity equation), leading to reduced particle velocity. Consequently, more MP particles become trapped, which aligns with the experimental results.

In tests 2 and 5, the transport and deposition pattern of MP particles initially formed a semi-circular shape. Over time, this shape stretched out as most particles exited the FOV, leaving a few particles deposit along the channel sides. However, in test 8, MP particles showed a different transport and deposition pattern. They became trapped in circulations zone that pushed most particles further downstream, with a few being directed towards the sides of the channel. It can be concluded that a few plastic particles become trapped within the FOV over the time, and this is because of the effect of the sliding friction applied to MPs from the walls on the sides.

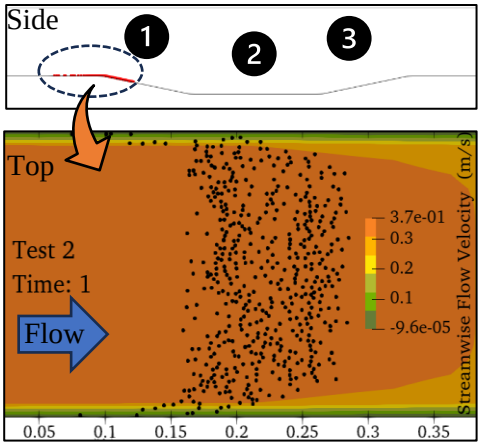

Longitudinal distance from the injection point (at x = 0) in x-direction (m)

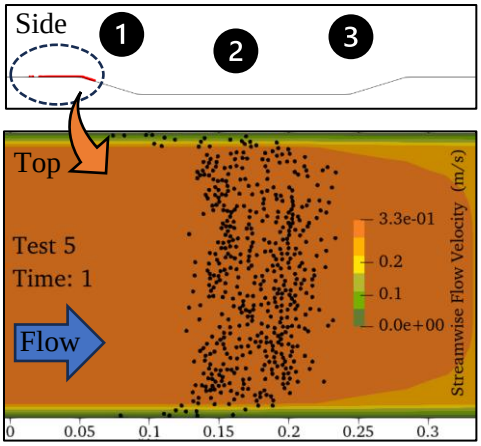

Longitudinal distance from the injection point (at x = 0) in x-direction (m)

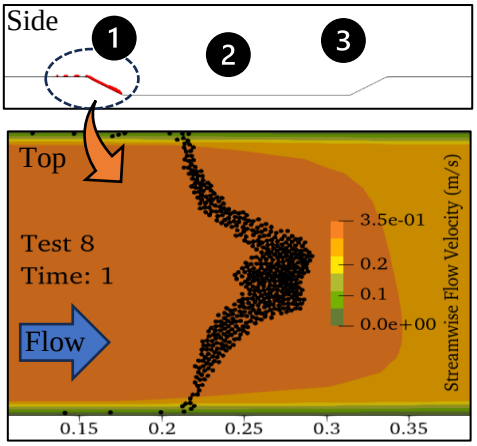

Longitudinal distance from the injection point (at x = 0) in x-direction (m)

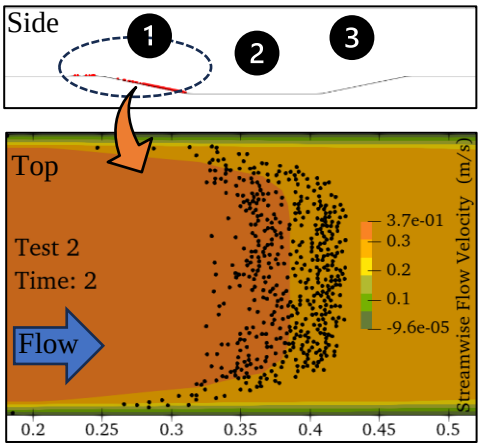

Longitudinal distance from the injection point (at x = 0) in x-direction (m)

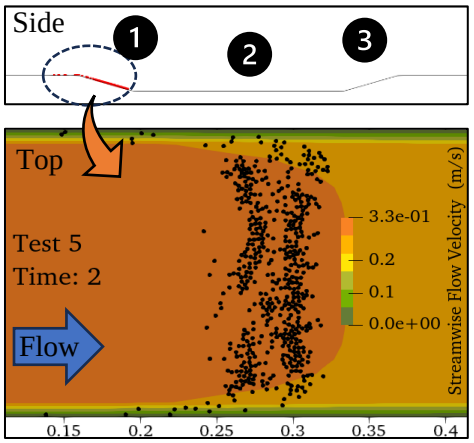

Longitudinal distance from the injection point (at x = 0) in x-direction (m)

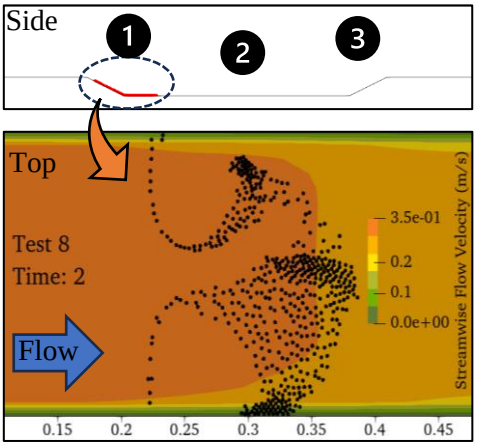

Longitudinal distance from the injection point (at x = 0) in x-direction (m)

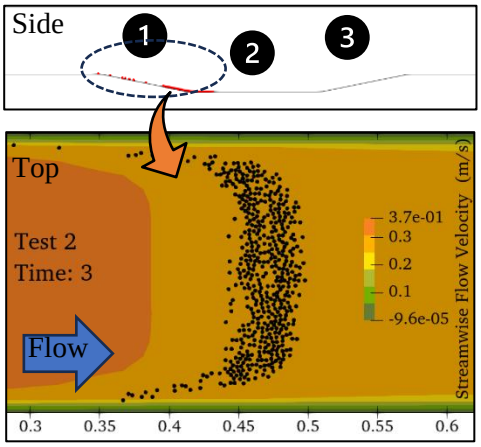

Longitudinal distance from the injection point (at x = 0) in x-direction (m)

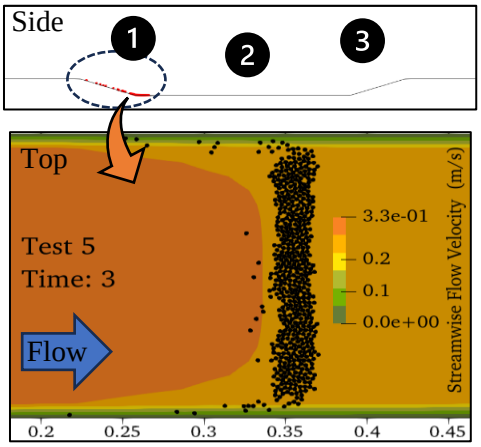

Longitudinal distance from the injection point (at x = 0) in x-direction (m)

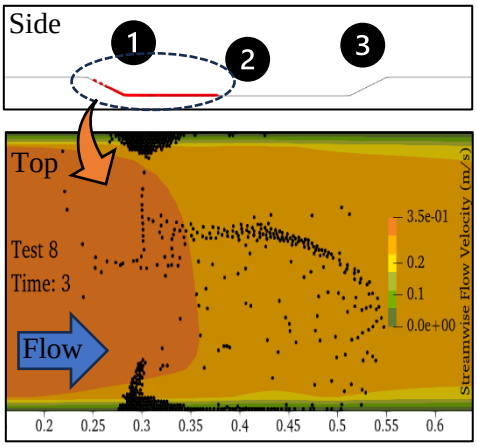

Longitudinal distance from the injection point (at x = 0) in x-direction (m)

Longitudinal distance from the injection point (at x = 0) in x-direction (m)

Longitudinal distance from the injection point (at x = 0) in x-direction (m)

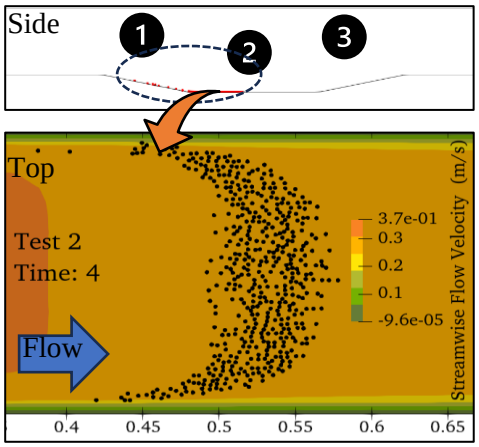

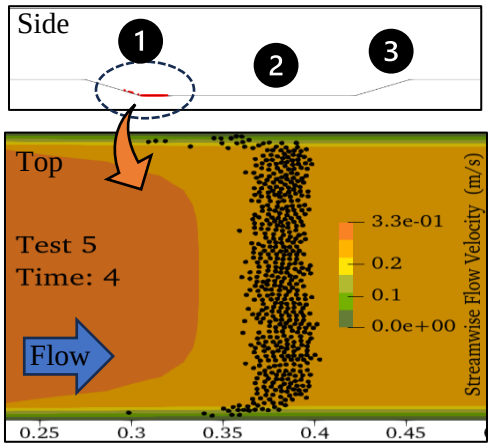

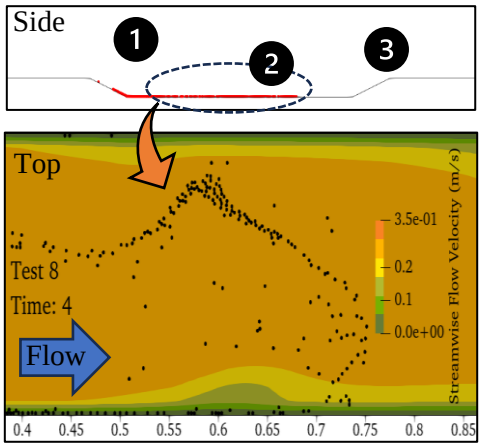

Longitudinal distance from the injection point (at x = 0) in x-direction (m)

Longitudinal distance from the injection point (at x = 0) in x-direction (m)

Longitudinal distance from the injection point (at x = 0) in x-direction (m)

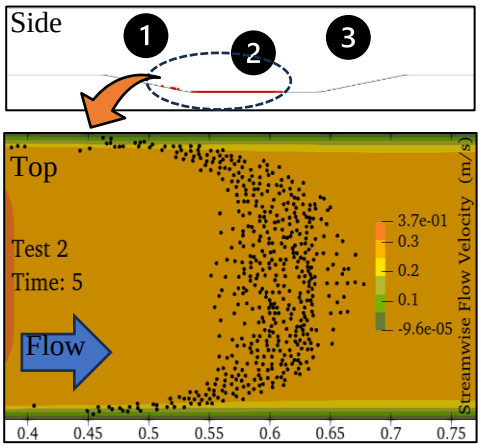

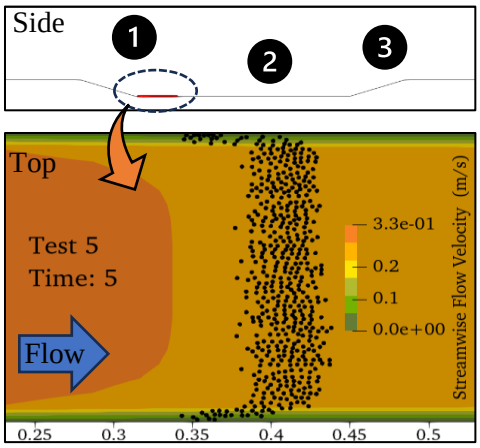

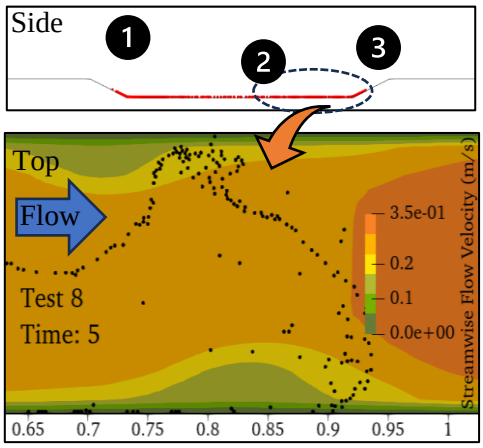

Longitudinal distance from the injection point (at x = 0) in x-direction (m)

Longitudinal distance from the injection point (at x = 0) in x-direction (m)

Longitudinal distance from the injection point (at x = 0) in x-direction (m)

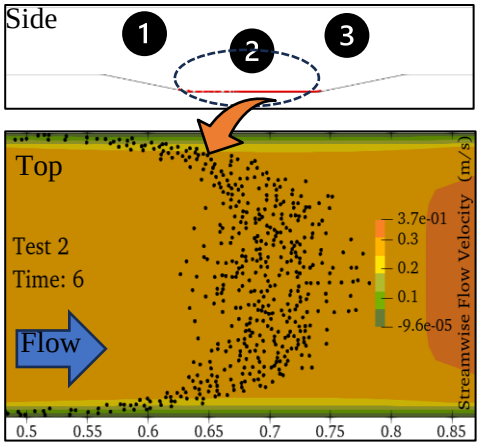

Longitudinal distance from the injection point (at x = 0) in x-direction (m)

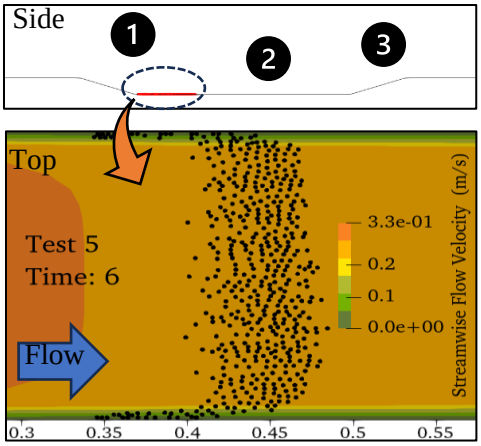

Longitudinal distance from the injection point (at x = 0) in x-direction (m)

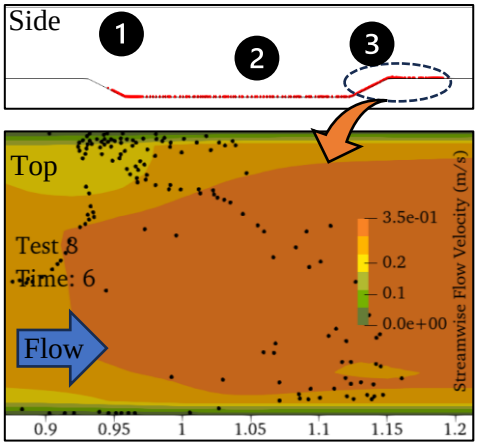

Longitudinal distance from the injection point (at x = 0) in x-direction (m)

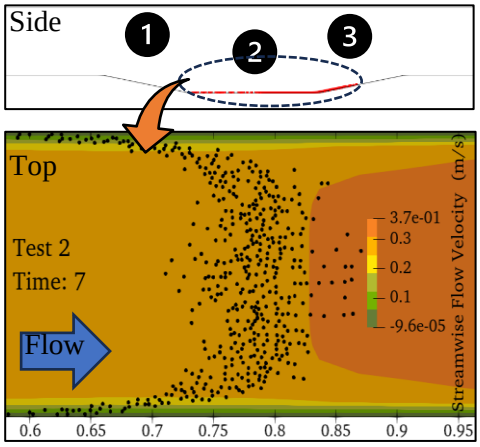

Longitudinal distance from the injection point (at x = 0) in x-direction (m)

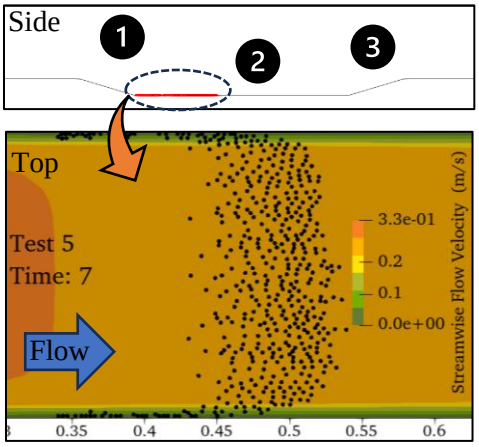

Longitudinal distance from the injection point (at x = 0) in x-direction (m)

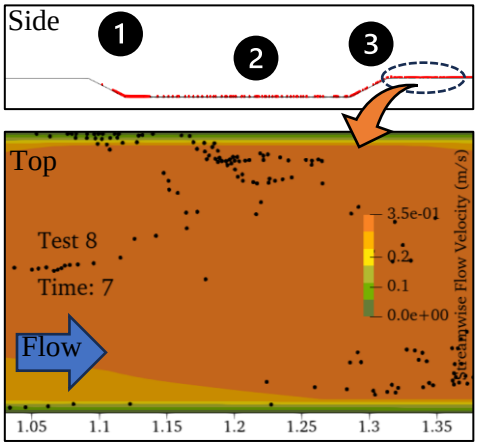

Longitudinal distance from the injection point (at x = 0) in x-direction (m)

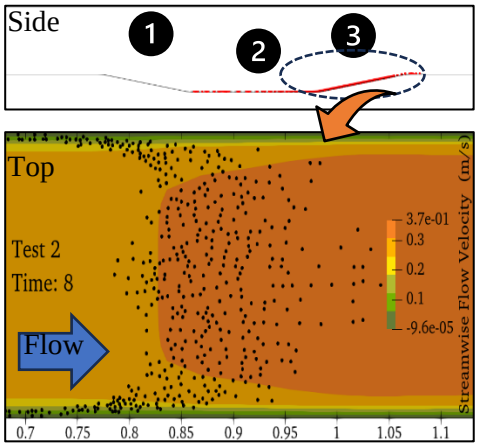

Longitudinal distance from the injection point (at x = 0) in x-direction (m)

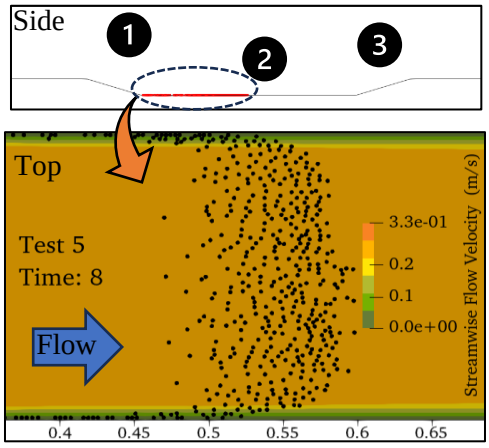

Longitudinal distance from the injection point (at x = 0) in x-direction (m)

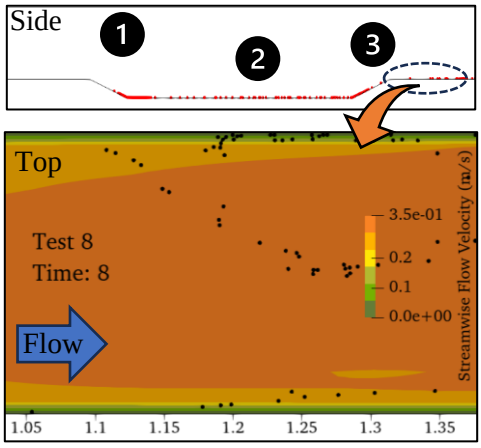

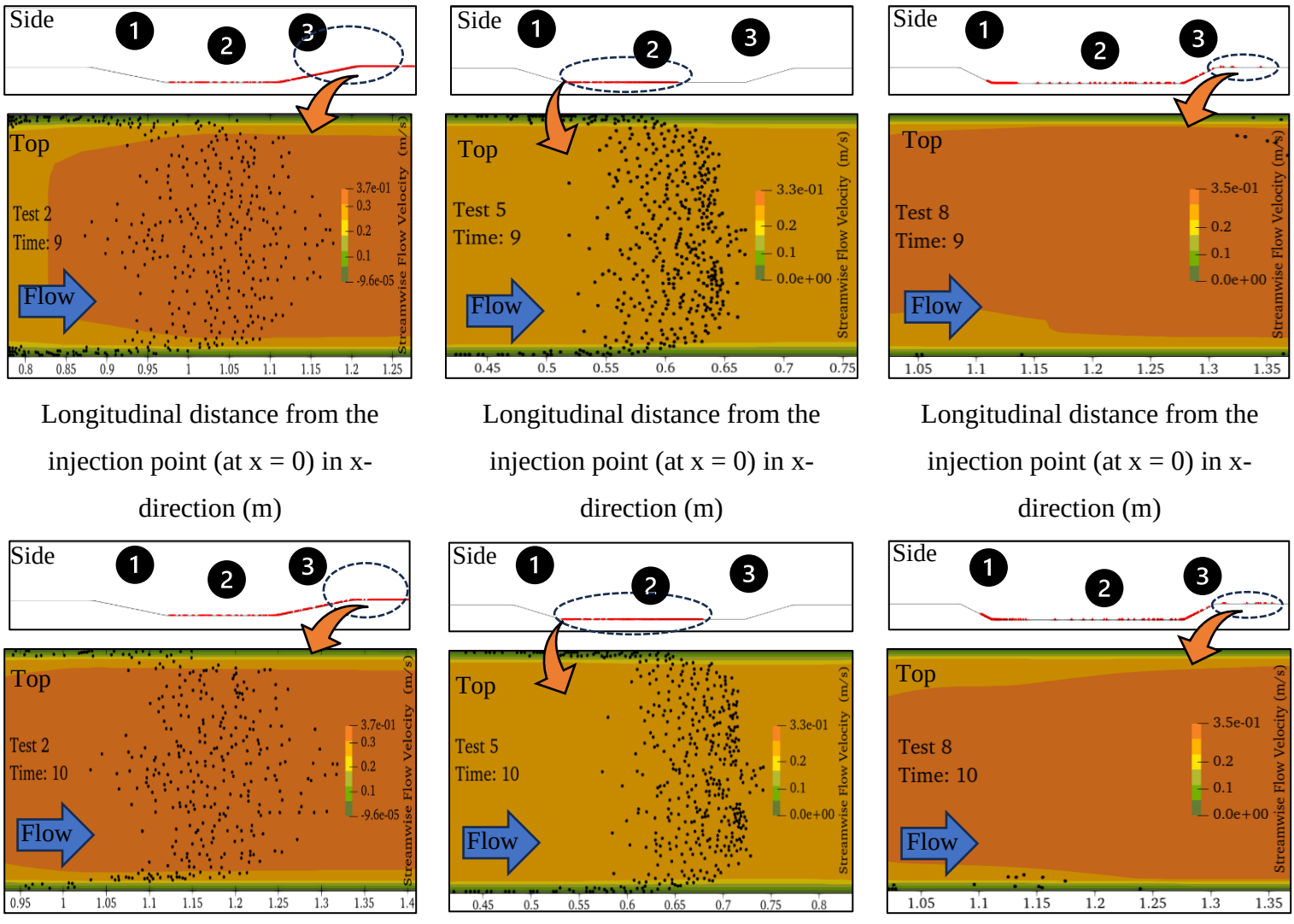

Figure 33. Typical pattern of spherical MPs deposition within the channel around FOV (x = 0.2 – 1 m) from both top and side views based on CFD-DEM simulation for (a) Test 2, (b) Test 5, and

(c) Test 8. The locations 1, 2, and 3 show the first slope, the flat bed, and the second slope applied to the channel bed, respectively.

MPs particles exhibited circulation, particularly in test 8 (see Figure 33c), due to the influence of the increased slope of the channel bed, which induced significant flow circulation. To investigate this further, the turbulent kinetic energy (k) contour lines for all three tests were depicted from the side view (Figure 34) at time-step equal to two when the first circulation was observed (in Test 8). It can be seen that the maximum value of k in Test 8 was almost doubled the k value in tests 2 and 5 at the same time across the channel bed including sloped and flat areas. Turbulent kinetic energy rises in areas with high local velocity gradients. This means that these areas are sources of turbulent kinetic energy where local velocity gradients are crucial (Pilechi et al., 2011). In this regard, it can be concluded that by increasing the slope of the channel bed, higher local velocities were generated resulting in larger k values and more intense circulations. As shown in Fig. 10, in all three tests, the maximum turbulent kinetic energy was reduced through diffusion and dissipation.

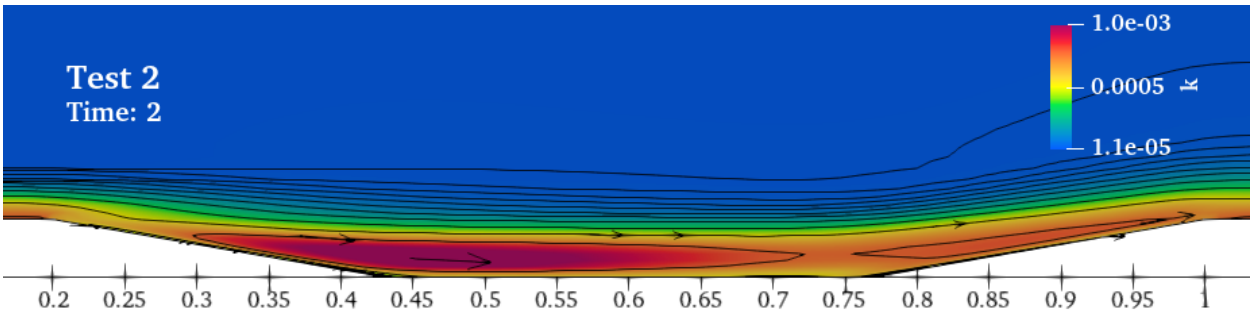

Longitudinal distance from the injection point (at x = 0) in x- direction (m)

(a)

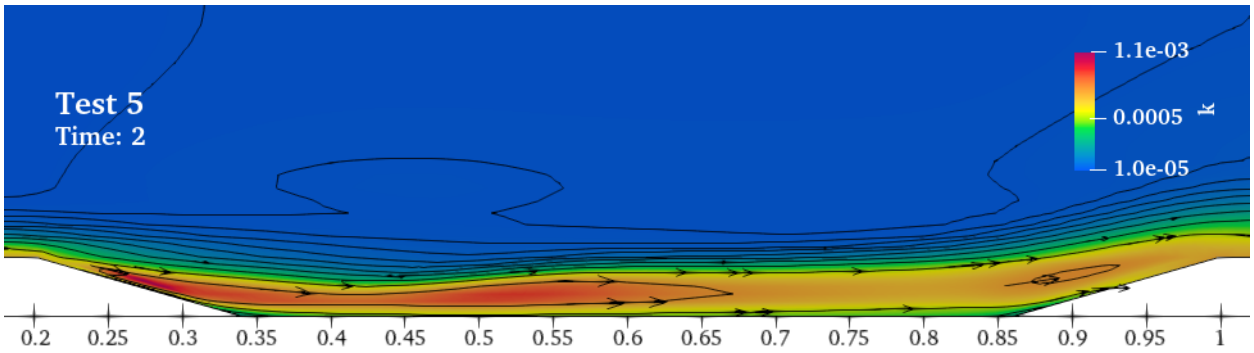

Longitudinal distance from the injection point (at x = 0) in x- direction (m)

(b)

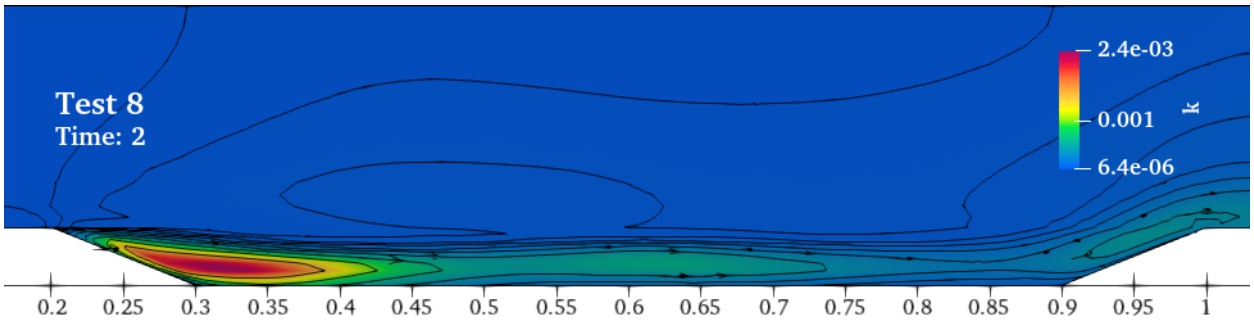

Longitudinal distance from the injection point (at x = 0) in x- direction (m)

(c)

Figure 34. Longitudinal cross-section contours of k within FOV (x = 0.2 – 1 m) at time = 2 s, from side view based on CFD-DEM simulation for (a) Test 2, (b) Test 5, and (c) Test 8.

5.4.3 Sensitivity analysis

To further evaluate the model's performance, a sensitivity analysis was conducted, as described in section 5.3.2.3, on the simulation results with respect to various parameters identified as potential impactful as shown in Table 21. The first parameter examined was the number of particles used is

the simulation. No significant difference in TE values were observed between simulations using 500 and 1000 particles. However, the TE values differed considerably when only 250 particles were used. This indicates that considering a very small number of particles compared to the number used in experiments or present in real conditions may lead to inaccurate results regarding the number of MPs accumulated (or deposited). On the other hand, considering the same number of MPs (used in experiments) in simulations highly increases the computational efforts without significantly improving result accuracy. Based on these findings, 500 particles were selected for the CFD-DEM coupling simulations across different test scenarios.

No significant difference was observed in the simulated TE for CFD mesh grid sizes smaller than 10 mm. Therefore, a grid resolution of 10 mm was chosen for the CFD mesh in all directions of simulations in this study, to balance accuracy and computational efficiency. It is important to note that the reported RA values are the best values obtained based on the measured and simulated TE values using the fine mesh.

Table 21. The performance (i.e., *RA* values) of the model in simulating MPs for Test 2 based on different sensitivity analysis parameters

Relative Accuracy	**Number of particles**			**Mesh size**			**Friction coefficient (f_s, f_r)**				**Coupling interval**		**DEM time-step (s)**	
	250	500	1000	Fine	Medium	Coarse	(0.1,0.05)	(0.05,0.1)	(0.05,0.05)	(0.01,0)	10	100	1e-5	2e-5
RA	0.56	0.70	0.72	0.70	0.65	0.64	0.23	0.19	0.51	0.70	0.70	0.70	0.70	0.70

Among the various numerical parameters for which sensitivity analysis was performed, the friction coefficient had the most significant impact on TE values across all 18 tested scenarios. Therefore, a detailed sensitivity analysis on the combination of sliding and rolling friction coefficients was conducted for all tests, as described in section 5.3.2.3. This analysis revealed that rolling friction (f_r) has a negligible effect compared to sliding friction (f_s). The combination of sliding friction f_s = 0.01 and rolling friction f_r = 0 showed the closest prediction to the experimental results.

Also, two coupling intervals of 10 and 100 with two DEM time-steps (1×10^{-5} s and 2×10^{-5} s) were analysed to assess their impact on computational efficiency and numerical stability. The coupling interval refers to the number of DEM time-steps between exchanges between the CFD and DEM models. Most simulations were successfully performed with a coupling interval of 100 and a DEM time-step of 2×10^{-5} s, which were more efficient in terms of computational cost. However, the model became unstable with this configuration in tests 4, 7, 13, and 16, which led to the use of smaller coupling intervals and DEM time-steps for these test cases. Despite these adjustments, no significant impact on the number of deposited MPs was observed with varying coupling intervals and DEM time-steps.

5.5 Conclusion

This study utilized a two-phase model combining fluid flow and spherical MPs dynamics, integrating CFD and DEM simulations. The study assessed the capability of a CFD-DEM model by creating digital replicas of experimental scenarios and comparing the model's predicted TE with laboratory measurements. Model accuracy was evaluated using the relative accuracy (RA) parameter. The numerical approach employed a four-way coupling method, incorporating fluid-particle interactions and particle-particle collisions, ensuring a two-way simulation for both dynamics. Fluid flow was modeled with OpenFOAM® using the PISO solver, while particle motion was simulated with Aspherix®. The CFD-DEM simulations were implemented using computational domains designed to match the dimensions, initial conditions, and boundary conditions of the physical model setups for comparison with experimental observations. Overall, the CFD-DEM model demonstrated an accuracy of over 61% in predicting TE values across the test scenarios.

The test with steepest slope (i.e., test 8) showed significant particle circulation due to increased bed slope. It was observed that the turbulent kinetic energy (k) value in this test was the largest compared to the k value obtained in the other tests. Therefore, it can be concluded that the larger

circulations occurred in steeper slope tests with higher k values. The steeper slope also resulted in greater water depth and lower flow velocity, causing reduced particle velocity and increased trapping of MPs, consistent with experimental observations. In milder slope tests (i.e., tests 2 and 5), MPs particles initially formed a semi-circular pattern, which gradually stretched out as most particles exited the FOV, leaving some deposited along the channel sides. However, in test 8, the particles behaved differently, becoming trapped in circulation zones that pushed them downstream, with some directed towards the channel sides. Over time, a few particles remained within the FOV due to the sliding friction from the channel walls.

A sensitivity analysis was conducted to evaluate the model's performance by examining the impact of various parameters on simulation results. Although the number of particles used in the simulation was found to significantly affect the results, the friction coefficients had the highest impact on TE values across all simulated test scenarios.

Given the findings provided in this study and to investigate more in-depth the capability of CFD-DEM in simulating MPs transport and deposition in water bodies, it is recommended to consider the following suggestions in future studies. First, it could be of great importance to include MPs particles with different physical properties (i.e., size, density, and shape) in numerical simulations performed using CFD-DEM. Second, it is crucial to include various types of water bodies with different hydraulic and geometric conditions in the numerical modeling of MPs transport and deposition using CFD-DEM, where a comprehensive physical modelling is required. Third, it is necessary to further investigate the effects of each parameter selected, through the sensitivity analysis, in this study on transport and deposition of MPs to obtain a better understanding of their impact on the accuracy of simulations.

5.6 References

Ai, J., Chen, J. F., Rotter, J. M., & Ooi, J. Y. (2011). Assessment of rolling resistance models in discrete element simulations. Powder technology, 206(3), 269-282.

Akbarzadeh, V. (2014). Modeling particle-particle and particle-wall interactions in liquid-particle flows in complex geometries

Alvarez-Zeferino, J. C., Ojeda-Benítez, S., Cruz-Salas, A. A., Martínez-Salvador, C., & Vázquez-Morillas, A. (2020). Microplastics in Mexican beaches. Resources, Conservation and Recycling, 155, 104633.

Anderson, T. B., & Jackson, R. (1967). Fluid mechanical description of fluidized beds. Equations of motion. Industrial & Engineering Chemistry Fundamentals, 6(4), pp.527-539.

Aspherix®. (2024). Tutorial. DCS Computing GmbH. https://www.aspherix-dem.com/services/training/

Ballent, A., Corcoran, P. L., Madden, O., Helm, P. A., & Longstaffe, F. J. (2016). Sources and sinks of microplastics in Canadian Lake Ontario nearshore, tributary and beach sediments. Marine pollution bulletin, 110(1), 383-395.

Bigdeli, M., Mohammadian, A., & Pilechi, A. (2024). A Laboratory Dataset on Transport and Deposition of Spherical and Cylindrical Large Microplastics for Validation of Numerical Models. Journal of Marine Science and Engineering, 12(6), 953.

Bigdeli, M., Mohammadian, A., Pilechi, A., & Bonakdari, H. (2025). Dynamic Prediction of Large Spherical and Cylindrical Microplastic Deposition: A Machine Learning Approach for Transport and Deposition. Under Review.

Bigdeli, M., Mohammadian, A., Pilechi, A., & Taheri, M. (2022). Lagrangian modeling of marine microplastics fate and transport: The state of the science. Journal of Marine Science and Engineering, 10(4), 481.

Bigdeli, M., Taheri, M., & Mohammadian, A. (2023). Numerical modeling of dam-break flood flows for dry and wet sloped beds. ISH Journal of Hydraulic Engineering, 29(3), 259-269.

Bondelind, M., Sokolova, E., Nguyen, A., Karlsson, D., Karlsson, A., & Björklund, K. (2020). Hydrodynamic modelling of traffic-related microplastics discharged with stormwater into the Göta River in Sweden. Environmental Science and Pollution Research, 27, 24218-24230.

Bujaczek, T., Kolter, S., Locky, D., & Ross, M. S. (2021). Characterization of microplastics and anthropogenic fibers in surface waters of the North Saskatchewan River, Alberta, Canada. Facets, 6(1), 26-43.

Carlson, D. F., Suaria, G., Aliani, S., Fredj, E., Fortibuoni, T., Griffa, A., Russo, A., & Melli, V. (2017). Combining litter observations with a regional ocean model to identify sources and sinks of floating debris in a semi-enclosed basin: the Adriatic Sea. Frontiers in marine science, 4, 78.

Castañeda, R. A., Avlijas, S., Simard, M. A., & Ricciardi, A. (2014). Microplastic pollution in St. Lawrence river sediments. Canadian Journal of Fisheries and Aquatic Sciences, 71(12), 1767-1771.

Cheng, K., Wang, Y., Yang, Q., Mo, Y., & Guo, Y. (2017). Determination of microscopic parameters of quartz sand through tri-axial test using the discrete element method. Computers and Geotechnics, 92, 22-40.

Corcoran, P. L., Belontz, S. L., Ryan, K., & Walzak, M. J. (2019). Factors controlling the distribution of microplastic particles in benthic sediment of the Thames River, Canada. Environmental science & technology, 54(2), 818-825.

Critchell, K., & Lambrechts, J. (2016). Modelling accumulation of marine plastics in the coastal zone; what are the dominant physical processes? Estuarine, Coastal and Shelf Science, 171, 111-122.

Cundall, P. A., & Strack, O. D. (1979). A discrete numerical model for granular assemblies. geotechnique, 29(1), 47-65.

Declerck, A., Delpey, M., Rubio, A., Ferrer, L., Basurko, O., Mader, J., & Louzao, M. (2019). Transport of floating marine litter in the coastal area of the south-eastern Bay of Biscay: A Lagrangian approach using modelling and observations. Journal of Operational Oceanography, 12(sup2), S111-S125.

Di Felice, R. (1994). The voidage function for fluid-particle interaction systems. International Journal of Multiphase Flow, 20(1), 153-159.

Díez-Minguito, M., Bermúdez, M., Gago, J., Carretero, O., & Viñas, L. (2020). Observations and idealized modelling of microplastic transport in estuaries: The exemplary case of an upwelling system (Ría de Vigo, NW Spain). Marine Chemistry, 222, 103780.

Domercq, P., Praetorius, A., & MacLeod, M. (2022). The Full Multi: An open-source framework for modelling the transport and fate of nano-and microplastics in aquatic systems. Environmental Modelling & Software, 148, 105291.

Ebbesmeyer, C. C., Ingraham, W., Jones, J. A., & Donohue, M. J. (2012). Marine debris from the Oregon Dungeness crab fishery recovered in the Northwestern Hawaiian Islands: identification and oceanic drift paths. Marine pollution bulletin, 65(1-3), 69-75.

Estrada, N., Azéma, E., Radjai, F., & Taboada, A. (2011). Identification of rolling resistance as a shape parameter in sheared granular media. Physical Review E—Statistical, Nonlinear, and Soft Matter Physics, 84(1), 011306.

Fonceca, I., Maza, D., & Hidalgo, R. C. (2021). Modeling particle-fluid interaction in a coupled CFD-DEM framework. EPJ Web of Conferences,

Gantt, J. A., Cameron, I. T., Litster, J. D., & Gatzke, E. P. (2006). Determination of coalescence kernels for high-shear granulation using DEM simulations. Powder technology, 170(2), 53-63.

Ghazizadeh, M., Rey, A., Pilechi, A., Burcher, R., Drouin, S. S.-O., & Lamontagne, P. (2024). A high-performance ray tracing particle tracking model for the simulation of microplastics in inland and coastal aquatic environments. Computer Physics Communications, 109423.

Goniva, C., Kloss, C., Hager, A., & Pirker, S. (2010). An open source CFD-DEM perspective. Proceedings of OpenFOAM Workshop, Göteborg,

Hardesty, B. D., Harari, J., Isobe, A., Lebreton, L., Maximenko, N., Potemra, J., Van Sebille, E., Vethaak, A. D., & Wilcox, C. (2017). Using numerical model simulations to improve the understanding of micro-plastic distribution and pathways in the marine environment. Frontiers in marine science, 4, 30.

Hoomans, B., Kuipers, J., Briels, W. J., & van Swaaij, W. P. M. (1996). Discrete particle simulation of bubble and slug formation in a two-dimensional gas-fluidised bed: a hard-sphere approach. Chemical Engineering Science, 51(1), 99-118.

Hu, Z., Zhang, Y., & Yang, Z. (2019). Suffusion-induced deformation and microstructural change of granular soils: a coupled CFD–DEM study. Acta Geotechnica, 14, 795-814.

Isobe, A., Iwasaki, S., Uchida, K., & Tokai, T. (2019). Abundance of non-conservative microplastics in the upper ocean from 1957 to 2066. Nature communications, 10(1), 1-13.

Isobe, A., Kako, S. i., Chang, P.-H., & Matsuno, T. (2009). Two-way particle-tracking model for specifying sources of drifting objects: application to the East China Sea Shelf. Journal of Atmospheric and oceanic technology, 26(8), 1672-1682.

Issa, R. I. (1986). Solution of the implicitly discretised fluid flow equations by operator-splitting. Journal of Computational Physics, 62(1), 40-65.

Iwashita, K., & Oda, M. (1998). Rolling resistance at contacts in simulation of shear band development by DEM. Journal of engineering mechanics, 124(3), 285-292.

Jasak, H. (2009). OpenFOAM: Open source CFD in research and industry. International journal of naval architecture and ocean engineering, 1(2), 89-94.

Jérémy, R., Gaston, L. P., & Valyrakis, M. (2020). Coupled CFD-DEM modelling to assess settlement velocity and drag coefficient of microplastics. EGU General Assembly.

Klaine, S. J., Alvarez, P. J., Batley, G. E., Fernandes, T. F., Handy, R. D., Lyon, D. Y., Mahendra, S., McLaughlin, M. J., & Lead, J. R. (2008). Nanomaterials in the environment: behavior, fate, bioavailability, and effects. Environmental Toxicology and Chemistry: An International Journal, 27(9), 1825-1851.

Koch, D. L., & Hill, R. J. (2001). Inertial effects in suspension and porous-media flows. Annual Review of Fluid Mechanics, 33(1), 619-647.

Kong, Y., Li, X., & Zhao, J. (2021). Quantifying the transition of impact mechanisms of geophysical flows against flexible barrier. Engineering Geology, 289, 106188.

Kremmer, M., & Favier, J. (2001). A method for representing boundaries in discrete element modelling—part II: Kinematics. International Journal for Numerical Methods in Engineering, 51(12), 1423-1436.

Lammerts, M. (2016). Marine litter in port areas-developing a propagation model.

Lebreton, L.-M., Greer, S., & Borrero, J. C. (2012). Numerical modelling of floating debris in the world's oceans. Marine pollution bulletin, 64(3), 653-661.

Li, Y., Xu, Y., & Thornton, C. (2005). A comparison of discrete element simulations and experiments for 'sandpiles' composed of spherical particles. Powder technology, 160(3), 219-228.

Liubartseva, S., Coppini, G., Lecci, R., & Clementi, E. (2018). Tracking plastics in the Mediterranean: 2D Lagrangian model. Marine pollution bulletin, 129(1), 151-162.

Liubartseva, S., Coppini, G., Lecci, R., & Creti, S. (2016). Regional approach to modeling the transport of floating plastic debris in the Adriatic Sea. Marine pollution bulletin, 103(1-2), 115-127.

Ma, Z., Wang, Y., Ren, N., & Shi, W. (2019). A coupled CFD-DEM simulation of upward seepage flow in coarse sands. Marine Georesources & Geotechnology, 37(5), 589-598.

Masliyah, J. (1998). Particle Deposition and Aggregation: Measurement, Modelling and Simulation. M. Elimelechet al. Journal of Colloid and Interface Science, 200(1), 195.

Maximenko, N., Hafner, J., & Niiler, P. (2012). Pathways of marine debris derived from trajectories of Lagrangian drifters. Marine pollution bulletin, 65(1-3), 51-62.

Mohsenabadi, S. E., Mohammadian, M., Nistor, I., & Gildeh, H. K. (2019). CFD modelling of near-field dam break flow. In Sustainable and Safe Dams Around the World, pp. 47-60.

Pilechi, A., Mohammadian, A., & Murphy, E. (2022). A numerical framework for modeling fate and transport of microplastics in inland and coastal waters. Marine pollution bulletin, 184, 114119.

Pilechi, A., Mohammadian, A., & Rennie, C. (2011). Experimental and Numerical study of turbulent wall jets

Rocha-Santos, T., & Duarte, A. C. (2015). A critical overview of the analytical approaches to the occurrence, the fate and the behavior of microplastics in the environment. TrAC Trends in analytical chemistry, 65, 47-53.

Rodríguez-Díaz, L., Gómez-Gesteira, J., Costoya, X., Gómez-Gesteira, M., & Gago, J. (2020). The Bay of Biscay as a trapping zone for exogenous plastics of different sizes. Journal of Sea Research, 163, 101929.

Smuts, E. M. (2015). A methodology for coupled CFD-DEM modeling of particulate suspension rheology.

Stuparu, D., van der Meulen, M., Kleissen, K., Vethaak, A., & El Serafy, G. (2015). Developing a transport model for plastic distribution in the North Sea. 36th IAHR World Congress,

Tsuji, Y., Kawaguchi, T., & Tanaka, T. (1993). Discrete particle simulation of two-dimensional fluidized bed. Powder technology, 77(1), 79-87.

Valyrakis, M., Diplas, P., Celik, A. O., & Dancey, C. L. (2008). Investigation of evolution of gravel river bed microforms using a simplified Discrete Particle Model. In Proceedings of River Flow.

Van Buijtenen, M. S., Van Dijk, W.-J., Deen, N. G., Kuipers, J., Leadbeater, T., & Parker, D. (2011). Numerical and experimental study on multiple-spout fluidized beds. Chemical Engineering Science, 66(11), 2368-2376.

Van Sebille, E., Griffies, S. M., Abernathey, R., Adams, T. P., Berloff, P., Biastoch, A., Blanke, B., Chassignet, E. P., Cheng, Y., & Cotter, C. J. (2018). Lagrangian ocean analysis: Fundamentals and practices. Ocean Modelling, 121, 49-75.

Van Sebille, E., Wilcox, C., Lebreton, L., Maximenko, N., Hardesty, B. D., Van Franeker, J. A., Eriksen, M., Siegel, D., Galgani, F., & Law, K. L. (2015). A global inventory of small floating plastic debris. Environmental Research Letters, 10(12), 124006.

Van Utenhove, E. (2019). Modelling the transport and fate of buoyant macroplastics in coastal waters.

Vangö, M. (2019). CFD-DEM modeling of multiphase fluid-granular systems and its application to blast furnace tapping/submitted by Mathias Vangö MSc.

Wang, Y., Zhou, L., & Yang, Q. (2019). Hydro-mechanical analysis of calcareous sand with a new shape-dependent fluid-particle drag model integrated into CFD-DEM coupling program. Powder technology, 344, 108-120.

Wang, Y., Zhou, L., & Yang, Q. (2019). Hydro-mechanical analysis of calcareous sand with a new shape-dependent fluid-particle drag model integrated into CFD-DEM coupling program. Powder Technology, 344, 108-120.

Wassgren, C., & Sarkar, A. (2008). Discrete element method (DEM) course module.

Wiesner, M. R., & Bottero, J.-Y. (2017). Surface Chemistry of Nanoparticles as It Affects Attachment. Environmental Nanotechnology: Applications and Impacts of Nanomaterials, Second Edition.

Xiong, H., Yin, Z.-Y., Zhao, J., & Yang, Y. (2021). Investigating the effect of flow direction on suffusion and its impacts on gap-graded granular soils. Acta Geotechnica, 16, 399-419.

Zhong, W., Yu, A., Liu, X., Tong, Z., & Zhang, H. (2016). DEM/CFD-DEM modelling of non-spherical particulate systems: theoretical developments and applications. Powder technology, 302 pp.108-152.

Zhou, Z., Kuang, S., Chu, K., & Yu, A. (2010). Discrete particle simulation of particle–fluid flow: model formulations and their applicability. Journal of Fluid Mechanics, 661, 482-510.

Zhu, H. P., Zhou, Z. Y., Yang, R., & Yu, A. (2007). Discrete particle simulation of particulate systems: theoretical developments. Chemical Engineering Science, 62(13), 3378-3396.

Zhu, L. (2019). Effects of Acoustic Fields on the Dynamics of Micro-particles in a Fluidized Bed.

6 Summary, Concluding Remarks, and Recommendations

6.1 Summary and Concluding Remarks

The water flow characteristics such as velocity and water depth, as well as physical properties of particles (including density, size, and shape), and bathymetric changes in water bodies affect the deposition patterns of marine MPs. As stated above, the main objective of this thesis is to utilize both physical and numerical modeling techniques to shed light on how spherical and cylindrical MPs are deposited or transported in water bodies, particularly considering changes in water bodies' bathymetry. Physical modeling provides not only valuable results regarding the sensitivity of MPs transport and deposition to different hydraulic and bathymetric conditions of water bodies but is also considered a reliable reference for numerical results. To achieve this goal, a series of experiments were carried out by employing a water body with a generic geometry to investigate the influence of various factors, such as the initial velocity of particles and depth of turbulent flows, changes in bathymetry, and shape of the MPs particles on their transport and deposition. This research was primarily focused on the use of two numerical approaches, the coupled CFD-DEM and ELM methods, to better understand and predict the transport and deposition of marine MPs in aquatic environments.

There are some concluding remarks obtained during this research that can be summarized as below:

1- This research was strongly founded on the review of four reliable lagrangian PTM models (i.e., D-WAQ PART, Ichthyop, TrackMPD, and CaMPSim-3D) to deliver a clear picture of the existing models in simulating the fate and transport of MPs. The comparison highlighted variations in how these models account for physical transport and transformation processes, as well as the effects of MPs properties such as size, shape, and density. Key findings indicated that TrackMPD and CaMPSim-3D incorporate more accurate equations for settling velocity, considering particle shape, whereas D-WAQ PART and Ichthyop use simplified formulations. Regarding transformation processes, only TrackMPD and CaMPSim-3D can simulate biofouling and degradation. While all models implement advection-diffusion equations, their approaches to parameterizing physical processes differ, with D-WAQ PART, TrackMPD, and CaMPSim-3D considering wind-

induced drift. In terms of mesh structure, CaMPSim-3D uniquely supports unstructured meshes, whereas the others rely on structured mesh systems. Despite these advancements, limitations remain. None of the reviewed models simulate homo- and hetero-aggregation, agglomeration, photodegradation, or chemical and biological degradation—key processes affecting MPs' long-term fate.

2- This study highlighted the importance of understanding how different shapes of MPs are transported and deposited in channels with generic geometry. The findings demonstrated that flow velocity and bathymetric changes significantly influence MPs behavior, with cylindrical particles exhibiting higher trapping tendencies than spherical ones. The dataset generated in this study served as a valuable resource for calibrating and validating numerical models, particularly CFD simulations, ensuring their reliability in cases where experimental data is unavailable.
3- This study highlighted the effectiveness of ML, specifically the ELM model, in predicting MPs deposition under various experimental conditions tested during physical modeling. The results confirmed that the best-performing model, including all dimensionless inputs that consisted of flow characteristics and the channel specifications, demonstrated high accuracy for both spherical and cylindrical datasets. The uncertainty analysis further validated the reliability of the model, with narrow uncertainty bands and small prediction error intervals.
4- This research successfully integrated CFD and DEM simulations to model fluid flow and spherical MPs dynamics, demonstrating the effectiveness of the CFD-DEM approach in replicating experimental conditions. The model achieved an accuracy of over 61% in predicting trapping tendencies of MPs, with results indicating that steeper slopes led to increased particle circulation, higher turbulent kinetic energy, and greater MPs trapping. Sensitivity analysis revealed that friction coefficients had the most significant influence on MPs trapping.

6.2 Recommendations for Future Studies

To enhance our understanding of MPs behavior and their environmental impact, further research should focus on either refining or employing the other numerical models to capture complex transport and transformation mechanisms with greater accuracy. Future studies should address critical gaps such as investigation of transformational processes, which impact MPs transport and

deposition, to develop a more comprehensive and reliable modeling framework for MPs pollution in aquatic systems. Limitations such as the consideration of only specific MP shapes, sizes, and densities, as well as the exclusion of varied sediment types, indicate the need for further research. Future studies should explore a broader range of MP characteristics and environmental conditions to enhance the understanding of MP transport and deposition dynamics. This research establishes a solid foundation for the future application of ML models in predicting MPs deposition, emphasizing their potential for broader environmental studies. It is important to note that to improve the understanding and accuracy of CFD-DEM simulations in MP transport and deposition, future studies should consider incorporating MPs with varying physical properties, modeling different hydraulic and geometric conditions, and further investigating the impact of key parameters identified during this research.